

UNCLASSIFIED

AD NUMBER

AD920772

LIMITATION CHANGES

TO:

Approved for public release; distribution is unlimited.

FROM:

Distribution authorized to U.S. Gov't. agencies only; Test and Evaluation; MAY 1974. Other requests shall be referred to Air Force Avionics Laboratory, ATTN: AFAL/TEM, Wright-Patterson AFB, OH 45433.

AUTHORITY

AFWAL ltr dtd 17 Apr 1984

THIS PAGE IS UNCLASSIFIED

THIS REPORT HAS BEEN DELIMITED
AND CLEARED FOR PUBLIC RELEASE
UNDER DOD DIRECTIVE 5200.20 AND
NO RESTRICTIONS ARE IMPOSED UPON
ITS USE AND DISCLOSURE.

DISTRIBUTION STATEMENT A

APPROVED FOR PUBLIC RELEASE;
DISTRIBUTION UNLIMITED.

AFAL-TR-74-128

L
BROADBAND RADOME TECHNIQUES

H. L. Bassett, D. G. Bodnar, G. K. Huddleston, et al.
Engineering Experiment Station
Georgia Institute of Technology
Atlanta, Georgia 30332

AD920772

TECHNICAL REPORT AFAL-TR-74-128



"Distribution limited to U. S. Government agencies only; test and evaluation results reported; May 1974. Other requests for this document must be referred to AFAL/TEM, Wright-Patterson Air Force Base, Ohio 45433"

**Air Force Avionics Laboratory
Air Force Systems Command
Wright-Patterson Air Force Base, Ohio**

AFAL-TR-74-128

BROADBAND RADOME TECHNIQUES

H. L. Bassett, D. G. Bodnar, G. K. Huddleston, et al.

"Distribution limited to U. S. Government agencies only; test and evaluation results reported; May 1974. Other requests for this document must be referred to AFAL/TEM, Wright-Patterson Air Force Base, Ohio 45433"

FOREWORD

This report was prepared by the Engineering Experiment Station of the Georgia Institute of Technology, Atlanta, Georgia, under USAF Contract No. F33615-71-C-1694. This contract was initiated under Project No. 2002, Task 4161, AFAL, Wright-Patterson Air Force Base, and is administered under the direction of Messrs. Harold Weber and Paul W. Springer, AFAL/TEM.

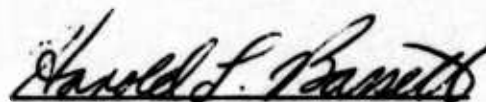
The period of performance covered by this report extends from 17 May 1971 to 27 February 1974 and this final report was submitted in April 1974. An interim report was published in January 1973 which covered the dates 17 May 1971 to 1 November 1972.

The report authors are: Harold L. Bassett, Donald G. Bodnar, G. Keith Huddleston and Joe M. Newton.

This research program was completed under the direction of Mr. J. W. Dees, Chief, Special Techniques Division and under the general supervision of Dr. R. C. Johnson, Assistant Director, Engineering Experiment Station.

Publication of this report does not constitute Air Force approval of the report's findings or conclusions. It is published only for the exchange and stimulation of ideas.

WILLIAM J. EDWARDS
Chief, Radar and Microwave
Technology Branch
Electronic Technology Division
Air Force Avionics Laboratory


Harold L. Bassett
Project Director


J. W. Dees, Chief
Special Techniques Division

ABSTRACT

The significance of this research and development to the Air Force is that a new type of electromagnetic window panel was designed and tested that exhibited a bandwidth of 10:1 or greater. Empirical data are included on both flat panels and curved panels. A typical panel that operates from 4 GHz to 40 GHz, having 90 percent or better transmission coefficient from 0° to 60° angle of incidence range, is 1.5-inches in thickness. The inner and outer surfaces of the panel are either grooves or pyramids. This type panel design has excellent circular polarization characteristics, since the amplitudes of the parallel and perpendicular components are near equal and since the insertion phase delays for the two components are approximately the same. Antenna radiation pattern measurements are included that also verify the broadband characteristics of these panels. Data are also presented on a computer analysis program of transmission through an anisotropic media. The analytical results compare favorably with the measured data.

TABLE OF CONTENTS

	<u>Page</u>
I. INTRODUCTION	1
II. ELECTRICAL THEORY	3
1. Introduction	3
2. Initial Panel Concept	3
3. Anisotropic Panel Analysis - Formulation of Problem	6
III. BROADBAND PANEL DESIGN	35
1. Panel No. 1	35
2. Panel No. 2	37
3. Pyramidal Panel	37
a. Mylar Coating	39
b. Rain Erosion Coating	39
c. Foam Filled Grooves	39
4. Curved Panel Design	39
5. High Dielectric Constant Panel Design (Panel No. 3)	40
IV. MEASURED RESULTS	43
1. Free-Space Measurement Technique	43
2. Panel No. 1 and Panel No. 2 Measured Results	44
3. Pyramidal Panel	44
a. Mylar Coated Pyramidal Grooves	49
b. Rain Erosion Coating over Pyramidal Grooves	49
c. Pyramidal Plate After Foaming	51
3. Curved Panel Measured Results	55
a. Transmission Data	55
b. Pyramidal Horn Radiation Patterns	55
c. Air Force Array Antenna Radiation Patterns	55
d. Curved Panel with Fiberglass Outer Shell	68
V. COMPARISON OF PREDICTED DATA TO MEASURED DATA	69
VI. PROBLEM AREAS	83
VII. CONCLUSIONS AND RECOMMENDATIONS	85

LIST OF FIGURES

	<u>Page</u>
1. Initial Broadband Panel Design (Panel No. 1)	5
2. Geometry of Homogeneous, Anisotropic Slabs	8
3. Orientation of the Unit Vectors and the \vec{D} Field in Layer m	12
4. Orientation of the Optic Axis in the m -th Region	12
5. Direction of Propagation of Incident Wave	12
6. Panel No. 1 (Groove Spacing = 0.25")	36
7. Photograph of Pyramidal Grooved Panel	38
8. Cylindrical Broadband Panel	41
9. Panel No. 1 Transmission Properties - Vertical Polarization .	45
10. Panel No. 1 Transmission Properties - Horizontal Polarization	46
11. Panel No. 2 Transmission Properties - Vertical Polarization .	47
12. Panel No. 2 Transmission Properties - Horizontal Polarization	48
13. Insertion Loss of Pyramidal Grooved Flat Panel With and Without Foam, Foam + Mylar, 0.020-inch Rain Erosion Coating, Horizontal Polarization, $f = 11.0$ GHz	52
14. Insertion Loss of Pyramidal Grooved Flat Panel With and Without Foam, Foam + Mylar, 0.020-inch Rain Erosion Coating, Vertical Polarization, $f = 11.0$ GHz	53
15. Insertion Phase Delay - Pyramidal Flat Plate with 0.020-inch Rain Erosion Coating	54
16. Radiation Pattern of Mid-Band Array, $f = 8$ GHz	56
17. Radiation Pattern of Mid-Band Array Mounted Flush with Inner Surface of Broadband Cylindrical Panel, $f = 8$ GHz . . .	57
18. Radiation Pattern of Mid-Band Array Mounted Toward Rear of Broadband Cylindrical Panel, $f = 8$ GHz	58

LIST OF FIGURES (Continued)

	<u>Page</u>
19. Radiation Pattern of Mid-Band Array, $f = 9$ GHz	59
20. Radiation Pattern of Mid-Band Array Mounted Flush with Inner Surface of Broadband Cylindrical Panel, $f = 9$ GHz . . .	60
21. Radiation Pattern of Mid-Band Array Mounted Toward Rear of Broadband Cylindrical Panel, $f = 9$ GHz	61
22. Radiation Pattern of Mid-Band Array, $f = 10$ GHz	62
23. Radiation of Mid-Band Array Mounted Flush with Inner Surface of Broadband Cylindrical Panel, $f = 10$ GHz	63
24. Radiation Pattern of Mid-Band Array Mounted Toward Rear of Broadband Cylindrical Panel, $f = 10$ GHz	64
25. Radiation Pattern of Mid-Band Array, $f = 11$ GHz	65
26. Radiation Pattern of Mid-Band Array Mounted Flush with Inner Surface of Broadband Cylindrical Panel, $f = 11$ GHz	66
27. Radiation Pattern of Mid-Band Array Mounted Toward Rear of Broadband Cylindrical Panel, $f = 11$ GHz	67
28. Grooved Broadband Panel Design	70
29. Steps in Determining Dielectric Constants of Layers in Grooved Dielectric Panel	71
30. Transmission Loss of Perpendicular Polarized Component for Panel No. 1	74
31. Transmission Loss of Parallel Polarized Component for Panel No. 1	75
32. Insertion Phase Delay of Perpendicular Polarized Component for Panel No. 1	76
33. Insertion Phase Delay of Parallel Polarized Component for Panel No. 1	77
34. Transmission Loss of Perpendicular Polarized Component for Panel No. 2	78
35. Transmission Loss of Parallel Polarized Component for Panel No. 2	79

LIST OF FIGURES (CONCLUDED)

	<u>Page</u>
36. Insertion Phase Delay of Perpendicular Polarized Component for Panel No. 2	80
37. Insertion Phase Delay of Parallel Polarized Component for Panel No. 2	81
38. Medium Parameter at the Interface at $z = z_m$	90
39. The Splitting of Two Waves Into Four When Passing Into a New Medium	90
40. Phase/Amplitude Plots, Horn Antenna, Vertical Pol., 11 GHz	98
41. Phase/Amplitude Plots Horn Antenna and Cylindrical Panel, Vertical Pol., 11 GHz, Panel Horizontal	99
42. Phase/Amplitude Plots, Horn Antenna and Cylindrical Panel, Vertical Pol., 11 GHz, Panel Horizontal; Fiberglass Cover	100
43. Phase/Amplitude Plots, Horn Antenna, Horizontal Pol., 11 GHz	101
44. Phase/Amplitude Plots, Horn Antenna and Cylindrical Panel, Horizontal Pol., 11 GHz; Panel Horizontal	102
45. Phase/Amplitude Plots, Horn Antenna and Cylindrical Panel, Horizontal Pol., 11 GHz; Panel Horizontal; Fiberglass Cover	103

LIST OF TABLES

	<u>Page</u>
I. PROPERTIES OF TWO TESTED PANELS	73
II. COMPARISON OF MEASURED AND PREDICTED TRANSMISSION LOSS AND INSERTION PHASE DELAY FOR PANEL NUMBER 1	82
III. COMPARISON OF MEASURED AND PREDICTED TRANSMISSION LOSS AND INSERTION PHASE DELAY FOR PANEL NUMBER 2	83

SECTION I

INTRODUCTION

This report describes the results of a research program to design, fabricate, and test broadband panels (both flat and curved). The transmission tests covered the 2-36 GHz frequency range.

The main goal of the program was to develop techniques whereby the panels would operate from 2 GHz through 36 GHz with a transmission efficiency of at least 70 percent for all incident angles up to $\pm 60^\circ$. Based on weight and thickness considerations, the panel designs presented herein operate from near 4 GHz through at least 40 GHz.

The basic panel design is discussed in detail in Interim Report No. 1 [1] and is reviewed in Section II of this report. Also, the anisotropic dielectric panel analysis is reviewed in Section II. A computer program has been developed which allows predictions to be made of the performance of any anisotropic dielectric panel.

The designs of broadband flat panels and curved panels are outlined in Section III. The design details are presented in this Section and the measured transmission data are included in Section IV. A rain erosion coating placed on the panel surface was used in some of the tests and these results are also presented. Radiation patterns of an array were measured using the curved panel as a radome and these patterns are shown in Section IV.

Comparisons of measured data and predicted data are made in Section V. The comparisons are very good indicating that the computer analysis accounts

for all reflections. A few of the problem areas associated with this type structure are presented in Section VI.

The Conclusions and Recommendations are covered in Section VII. An evaluation of propagation constants and directions of propagation that aid in the explanation of the computer analysis program is found in Appendix A. Appendix B is a compilation of typical transmission data and radiation pattern data utilizing the broadband panels.

SECTION II

ELECTRICAL THEORY

1. Introduction

The proposed broadband panel concept was based on previous work at Georgia Tech sponsored by the Air Force Avionics Laboratory [2,3]. The rationale for this concept and the initial design analysis are summarized in this Section. It was apparent during the first phase of the program that accurate prediction techniques were required to determine the transmission properties of the broadband panel concept, because the measurement of these properties in the laboratory was very time consuming. A computer aided anisotropic dielectric panel analysis has been generated and is discussed in this Section.

2. Initial Panel Concept

Reflections from panels can be eliminated by smoothly changing the dielectric constant of the panel from a value of 1.0 at the inner and outer surfaces to an arbitrary value in the interior [4]. This method of obtaining broadband panels is an application of Richmond's [4] WKB solution for plane wave transmission through inhomogeneous plane layers. For the case of a lossless panel with a relative dielectric constant near unity just inside the panel on both sides, the interface reflection coefficients are near zero for both polarizations. Under the conditions for which the WKB solution is valid [4], the transmission coefficients for both polarizations are unity, the insertion phase delays of the parallel and perpendicular components are equal, and the phase of the transmitted wave depends only

on the average value of the expression $\sqrt{\kappa_r(z) - \sin^2 \theta}$ in a panel of thickness d , where κ_r is the relative dielectric constant of the dielectric panel, z is the distance measured from the surface of the panel toward the interior, and θ is the angle of incidence.

The main problem with applying these results is that of realizing a practical structure that has the required variation, $\kappa_r(z)$, of dielectric constant. That is,

$$(1) \quad \kappa_r(0) = 1.0 \text{ (incident point),}$$

$$(2) \quad \kappa_r(d) = 1.0 \text{ (exit point), and}$$

$$(3) \quad \left| \frac{d \kappa_r(z)}{dz} \right| \ll 2k [\kappa_r(z) - \sin^2 \theta]^{3/2}.$$

In utilizing these results for the design of panel No. 1 (Figure 1), additional design data were required. As previously reported [1], the spacing restriction between the grooves is:

$$2l/\lambda_0 = \frac{1.0}{\sqrt{\kappa_2} + \sqrt{\kappa_1} |\sin \theta_1|}, \quad (1)$$

where

θ_1 = angle of incidence,

κ_1 = 1 (free space dielectric constant),

κ_2 = dielectric constant of panel material, and

$2l$ = center-to-center spacing of the strips.

There is also a restriction on the rate of change of the dielectric constant

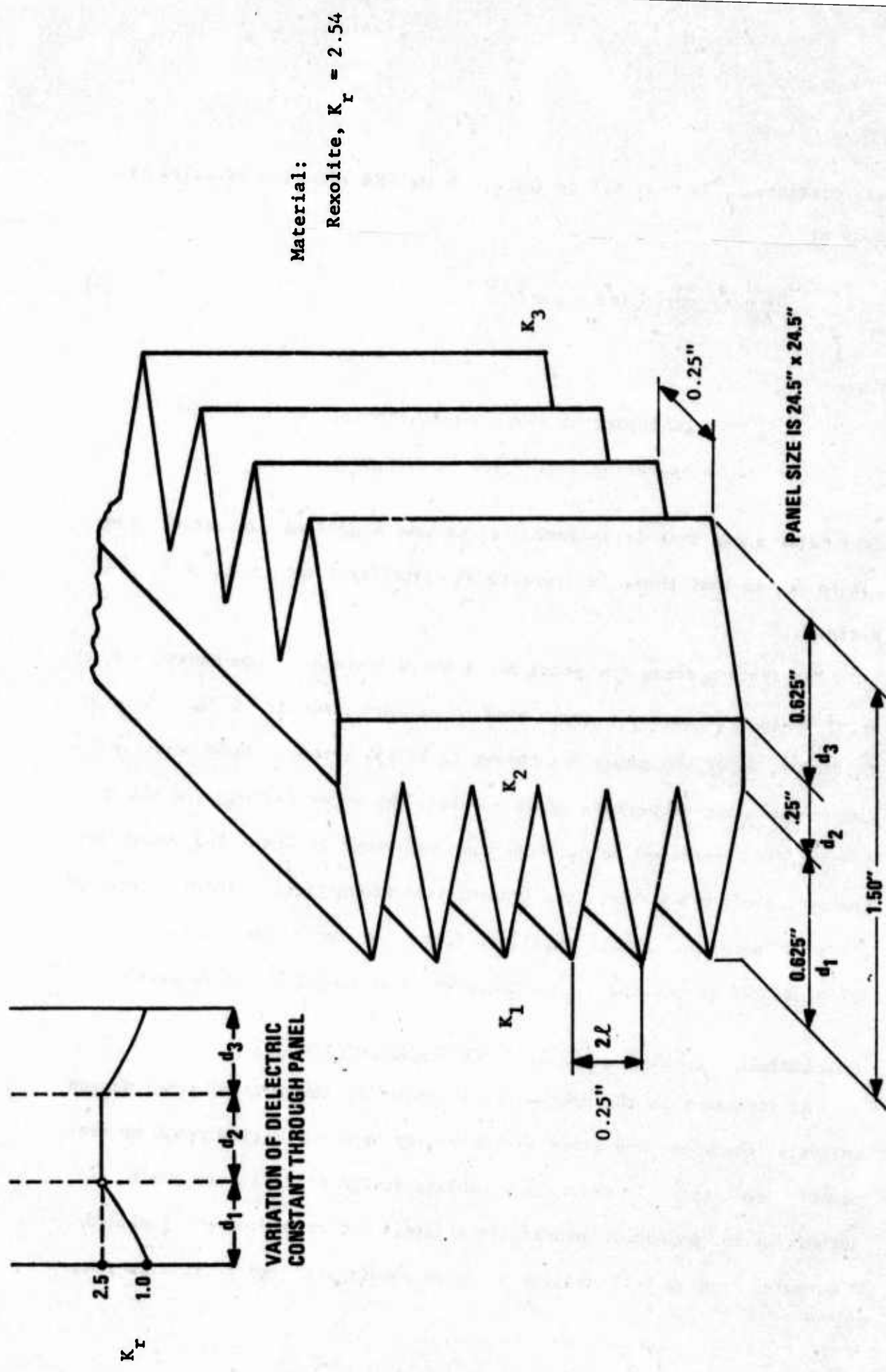


Figure 1. Initial Broadband Panel Design (Panel No. 1).

with distance. The restriction for which the WKB solution is valid is given by

$$|\frac{\partial r}{\partial z}| \ll \frac{4\pi}{\lambda_0} [\kappa_r(z) - \sin^2 \theta]^{3/2}, \quad (2)$$

where

$\kappa_r(z)$ = real part of complex permittivity function, and

λ_0 = operating free-space wavelength.

It is also known that it is necessary to have a gradual transition from air to κ_2 , so that there is a practical restriction on the taper of the strips.

The strip spacing for panel No. 1 was 0.25-inch. From Equation 2, the upper frequency limit was calculated to be approximately 18 GHz. A total thickness, d , of the panel was chosen to be 1.5 inches. Upon measuring the transmission properties of this panel, the upper frequency where the transmission decreased below 90 percent was about 18 GHz. The lower frequency cut-off was 4 GHz. The transmission properties, both amplitude and phase, of panel No. 1 were excellent from 4 GHz to 18 GHz. These data are presented in Section IV and compared to calculated data in Section V.

3. Anisotropic Panel Analysis - Formulation of Problem

As indicated in the preceding discussion of the initial panel design analysis, the upper and lower frequency limits of operation could be reasonably predicted. In order to establish design criteria and prediction techniques for broadband panels, an analysis was completed and included a computer program that modeled the type panels designed on this program.

Consider a series of planar slabs, as shown in Figure 2, that are infinite in the $\pm x$ and $\pm y$ directions, that are perpendicular to the z axis, and each of which is linear and homogeneous in permittivity and permeability but possibly anisotropic in its permittivity. Let there be a total of N slabs including the semi-infinite isotropic-dielectric regions on either side of the central slabs. In the m -th slab (for $m = 1, 2, \dots, N$) assume that the rectangular components of the permittivity tensor are given by

$$\tilde{\epsilon}_m = \begin{bmatrix} \epsilon_{x_m} & 0 & 0 \\ 0 & \epsilon_{y_m} & 0 \\ 0 & 0 & \epsilon_{z_m} \end{bmatrix} = \epsilon_0 \begin{bmatrix} \kappa_{x_m} & 0 & 0 \\ 0 & \kappa_{y_m} & 0 \\ 0 & 0 & \kappa_{z_m} \end{bmatrix} \quad (3)$$

where ϵ_{x_m} , ϵ_{y_m} , and ϵ_{z_m} are all constants, ϵ_0 is the free space permittivity, and κ_{x_m} , κ_{y_m} , and κ_{z_m} are the dielectric constants in the principal coordinate directions. Also assume that the permeability of all layers is μ where μ is a scalar constant. Let the m -th slab start at $z = d_{m-1}$, end at $z = d_m$ and have a thickness ℓ_m . The total thickness of all finite thickness dielectric slabs will be L .

Let \tilde{E}_m and \tilde{H}_m be the total electric and magnetic fields, respectively, in the m -th region. The field, \tilde{E}_m will, in general, be composed of an incident field \tilde{E}_{i_m} and a reflected field \tilde{E}_{r_m} so that

$$\tilde{E}_m = \tilde{E}_{i_m} + \tilde{E}_{r_m} \quad (4)$$

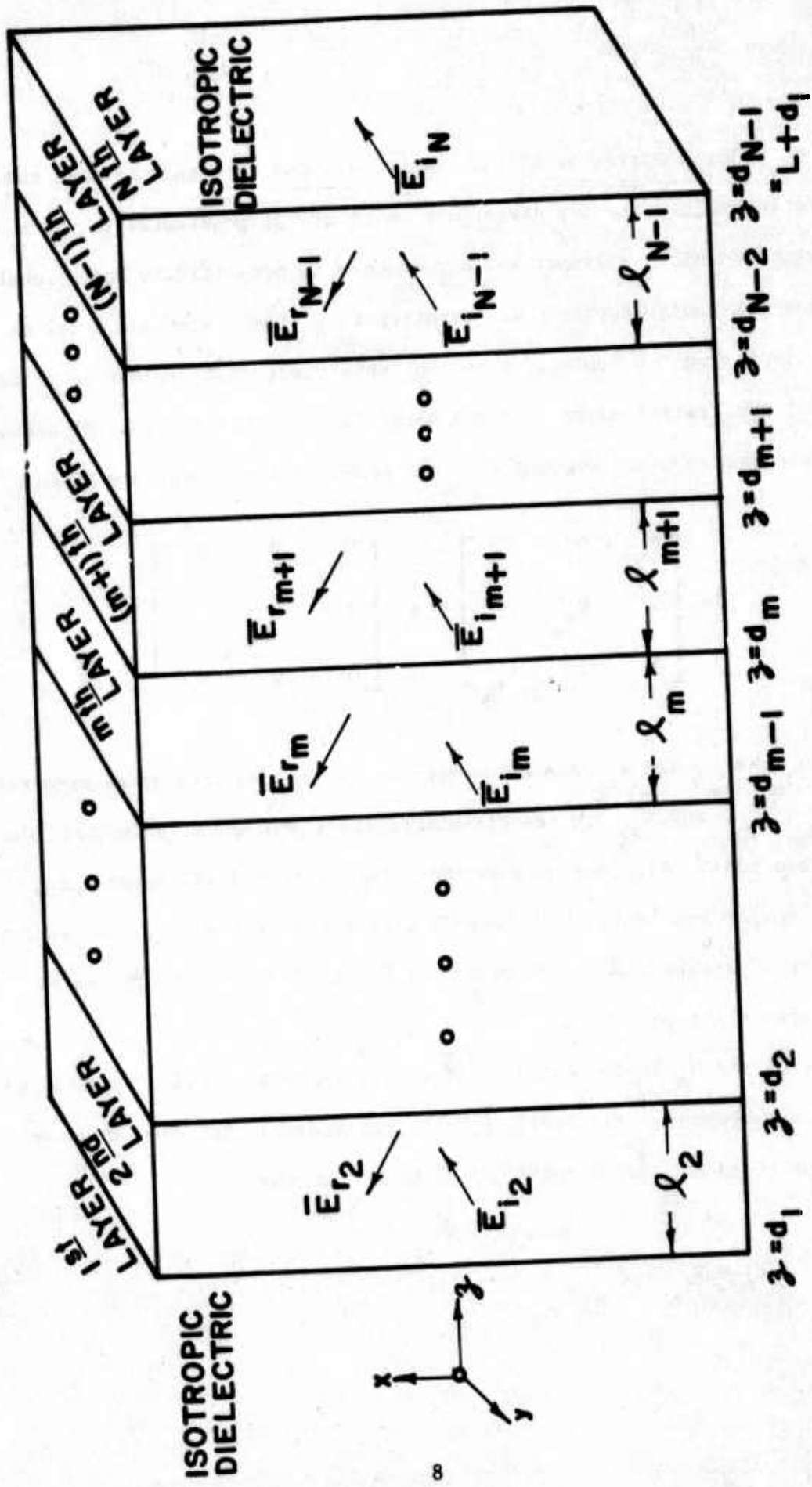


Figure 2. Geometry of Homogeneous, Anisotropic Slabs.

Let us now assume that only plane waves exist in each layer. Since each layer is dielectrically anisotropic, in general, then both the incident and the reflected fields will in general contain ordinary and extra-ordinary wave components [5,6]. Hence the incident and reflected fields can be written as

$$\begin{aligned}\bar{E}_{i_m} &= \bar{E}_{i_m}^o + \bar{E}_{i_m}^e \\ \bar{E}_{r_m} &= \bar{E}_{r_m}^o + \bar{E}_{r_m}^e\end{aligned}\quad (5)$$

In general, $\bar{E}_{i_m}^o$ consists of many waves traveling in different directions with different propagation constants. The same statement can be made for $\bar{E}_{i_m}^e$, $\bar{E}_{r_m}^o$, and $\bar{E}_{r_m}^e$. To illustrate this point, consider a single wave incident from region 1 onto region 2. This wave will split into two components [7] when it strikes the anisotropic region 2. Upon striking region 3, each wave from region 2 will split in two. Hence, progressively more waves are present as one moves from left to right. Handling all of these components gets very complicated; therefore, a simplification is made. It is shown in Appendix A that if (a) each slab is uniaxial (or isotropic), (b) the optical axis of each layer lies in the x-y plane, and (c) each optical axis is either parallel or perpendicular to all other optical axes then (1) only one ordinary and one extraordinary component exists for each $\bar{E}_{i_m}^o$ (similarly for $\bar{E}_{i_m}^e$, $\bar{E}_{r_m}^o$, $\bar{E}_{r_m}^e$) and (2) the incident and reflected waves in a medium have the same ordinary (and extraordinary) propagation constants. Assumptions (a), (b), and (c) will be made in all that follows.

Hence, let β_m^o and β_m^e be the propagation constants of the ordinary and extraordinary waves, respectively, in the m -th region, and let \bar{n}_i^o , \bar{n}_i^e , $\bar{n}_r^o_m$, and $\bar{n}_r^e_m$ be the direction of propagation of $\bar{E}_i^o_m$, $\bar{E}_i^e_m$, $\bar{E}_r^o_m$ and $\bar{E}_r^e_m$, respectively.

By assumption (a) above, each slab is uniaxial. According to Born and Wolf [5] and to Jones [8], for a uniaxial crystal the electric flux density \bar{D} of the ordinary wave is perpendicular to the principal plane while \bar{D} of the extraordinary wave lies in the principal plane. The principal plane is defined to be the plane containing the optic axis and the direction of propagation. Thus in each region there are four principal planes, one for each of the four components in (5).

A rectangular coordinate system will now be established for each of these four components in terms of the principal planes. For brevity, let \bar{n}_m represent any of the four directions of propagation vectors $\bar{n}_i^o_m$, $\bar{n}_i^e_m$, $\bar{n}_r^o_m$, and $\bar{n}_r^e_m$. Let \bar{u}_o_m be a unit vector in the direction of the optical axis in the m -th region. Notice that \bar{u}_o_m is independent of which of the four direction of propagation vectors is selected for \bar{n}_m . Let $\bar{u}_{\perp m}$ be a unit vector perpendicular to both the optical axis and the direction of propagation \bar{n}_m such that

$$\bar{u}_{\perp m} = \frac{\bar{n}_m \times \bar{u}_o_m}{|\bar{n}_m \times \bar{u}_o_m|} \quad (6)$$

Notice that $\bar{u}_{\perp m}$ depends on which direction of propagation is selected for \bar{n}_m . Finally, an orthogonal coordinate system will be completed by defining a unit vector $\bar{u}_{\parallel m}$ in the principal plane such that

$$\bar{u}_{\parallel m} = \frac{\bar{u}_{o_m} \times \bar{u}_{\perp m}}{|\bar{u}_{o_m} \times \bar{u}_{\perp m}|} \quad (7)$$

Substituting (6) into (7) gives

$$\bar{u}_{\parallel m} = \frac{\bar{u}_{o_m} \times (\bar{n}_m \times \bar{u}_{o_m})}{|\bar{u}_{o_m} \times (\bar{n}_m \times \bar{u}_{o_m})|}$$

or

$$\bar{u}_{\parallel m} = \frac{\bar{n}_m - \bar{u}_{o_m} (\bar{n}_m \cdot \bar{u}_{o_m})}{|\bar{n}_m - \bar{u}_{o_m} (\bar{n}_m \cdot \bar{u}_{o_m})|} \quad (8)$$

The orientation of \bar{u}_{o_m} , $\bar{u}_{\perp m}$, $\bar{u}_{\parallel m}$, and \bar{n}_m are shown in Figure 3. Notice that \bar{u}_{o_m} , $\bar{u}_{\parallel m}$ and \bar{n}_m are coplanar in the principal plane and that $\bar{u}_{\perp m}$ is perpendicular to this plane.

The unit vectors \bar{u}_{o_m} , $\bar{u}_{\perp m}$, and $\bar{u}_{\parallel m}$ form a right-handed rectangular coordinate system. The ordinary component of \bar{D} is colinear with $\bar{u}_{\perp m}$ and the extraordinary component of \bar{D} lies in the principal plane as shown in Figure 3. Since each layer is uniaxial, the dielectric constant is independent of direction in any plane transverse to the optic axis. Thus, by choosing \bar{u}_{o_m} , $\bar{u}_{\perp m}$, and $\bar{u}_{\parallel m}$ as the axes, the permeability tensor can be reduced to diagonal form with the $\bar{u}_{\perp m}$ and $\bar{u}_{\parallel m}$ components of the tensor being identical. Thus, the components of \bar{E} along the \bar{u}_{o_m} and $\bar{u}_{\parallel m}$ transfer into the extraordinary component of \bar{D} and the component of \bar{E} along $\bar{u}_{\perp m}$ transfers into the ordinary component of \bar{D} .

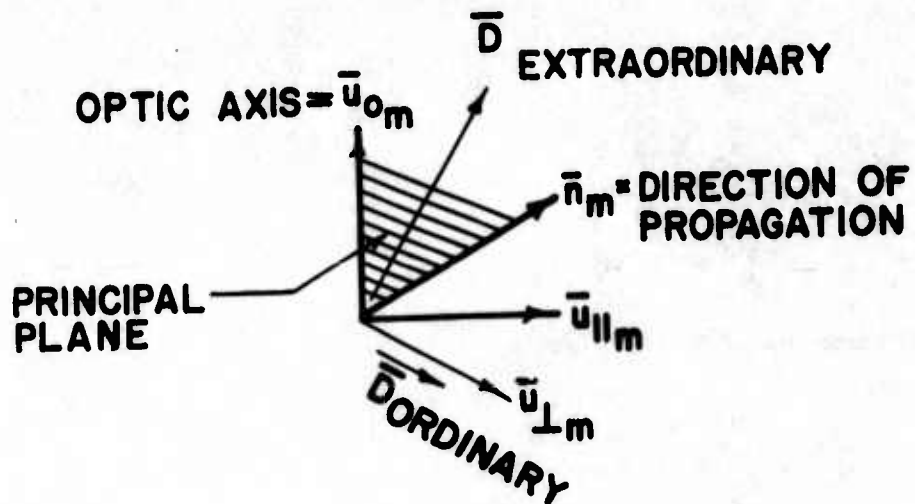


Figure 3. Orientation of the Unit Vectors and the \bar{D} Field in Layer m .

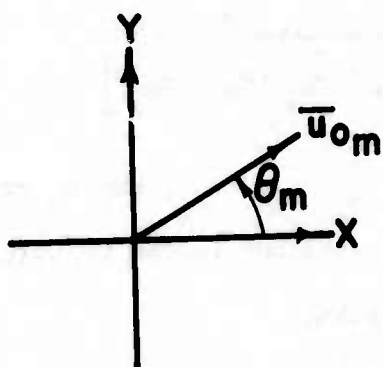


Figure 4. Orientation of the Optic Axis in the m -th Region.

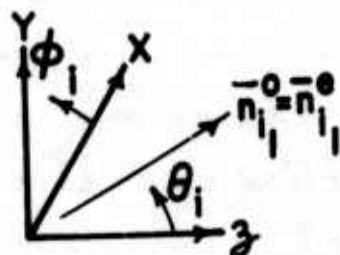


Figure 5. Direction of Propagation of Incident Wave.

From the preceding observations and the above notation, the components of the field in (5) may be written as

$$\begin{aligned}
 \bar{E}_{i_m}^o &= \bar{u}_{\perp_m}^i \bar{E}_{\perp_m}^i \exp(-j\beta_m^o \bar{n}_{i_m}^o \cdot \bar{r}) \\
 \bar{E}_{i_m}^e &= (\bar{u}_{o_m}^e \bar{E}_{o_m}^e + \bar{u}_{\parallel_m}^i \bar{E}_{\parallel_m}^i) \exp(-j\beta_m^e \bar{n}_{i_m}^e \cdot \bar{r}) \\
 \bar{E}_{r_m}^o &= \bar{u}_{\perp_m}^r \bar{E}_{\perp_m}^r \exp(-j\beta_m^o \bar{n}_{r_m}^o \cdot \bar{r}) \\
 \bar{E}_{r_m}^e &= (\bar{u}_{o_m}^r \bar{E}_{o_m}^r + \bar{u}_{\parallel_m}^r \bar{E}_{\parallel_m}^r) \exp(-j\beta_m^e \bar{n}_{r_m}^e \cdot \bar{r}) \quad (9)
 \end{aligned}$$

where $\bar{E}_{o_m}^i$, $\bar{E}_{\perp_m}^i$, $\bar{E}_{\parallel_m}^i$, $\bar{E}_{o_m}^r$, $\bar{E}_{\perp_m}^r$, and $\bar{E}_{\parallel_m}^r$ are complex constants representing the complex amplitude coefficients and

$$\begin{aligned}
 \bar{u}_{\perp_m}^i &\triangleq \frac{\bar{n}_{i_m}^o \times \bar{u}_{o_m}^o}{\left| \bar{n}_{i_m}^o \times \bar{u}_{o_m}^o \right|} \triangleq (u_{x_{\perp_m}}^i, u_{y_{\perp_m}}^i, u_{z_{\perp_m}}^i) \\
 \bar{u}_{\perp_m}^r &\triangleq \frac{\bar{n}_{r_m}^o \times \bar{u}_{o_m}^o}{\left| \bar{n}_{r_m}^o \times \bar{u}_{o_m}^o \right|} \triangleq (u_{x_{\perp_m}}^r, u_{y_{\perp_m}}^r, u_{z_{\perp_m}}^r) \\
 \bar{u}_{\parallel_m}^i &\triangleq \frac{\bar{n}_{i_m}^e - \bar{u}_{o_m}^o (\bar{n}_{i_m}^e \cdot \bar{u}_{o_m}^o)}{\left| \bar{n}_{i_m}^e - \bar{u}_{o_m}^o (\bar{n}_{i_m}^e \cdot \bar{u}_{o_m}^o) \right|} \triangleq (u_{x_{\parallel_m}}^i, u_{y_{\parallel_m}}^i, u_{z_{\parallel_m}}^i) \\
 \bar{u}_{\parallel_m}^r &\triangleq \frac{\bar{n}_{r_m}^e - \bar{u}_{o_m}^o (\bar{n}_{r_m}^e \cdot \bar{u}_{o_m}^o)}{\left| \bar{n}_{r_m}^e - \bar{u}_{o_m}^o (\bar{n}_{r_m}^e \cdot \bar{u}_{o_m}^o) \right|} \triangleq (u_{x_{\parallel_m}}^r, u_{y_{\parallel_m}}^r, u_{z_{\parallel_m}}^r) \quad (10)
 \end{aligned}$$

and the symbol \triangleq means "defined as".

The magnetic field, \bar{H}_m , associated with \bar{E}_m can be obtained from the Maxwell equation

$$\nabla \times \bar{E}_m = -j\omega\mu\bar{H}_m$$

This last equation combined with (4) and (5) gives

$$\bar{H}_m = \frac{-1}{j\omega\mu} [\nabla \times \bar{E}_{i_m}^0 + \nabla \times \bar{E}_{r_m}^0 + \nabla \times \bar{E}_{i_m}^e + \nabla \times \bar{E}_{r_m}^e] \quad (11)$$

Substituting (9) into (11) produces

$$\begin{aligned} \bar{H}_m = & \frac{\beta^0}{\omega\mu} [\bar{n}_{i_m}^0 \times \bar{u}_{\perp_m}^i \bar{E}_{\perp_m}^i] \exp(-j\beta_m^0 \bar{n}_{i_m}^0 \cdot \bar{r}) \\ & + \frac{\beta^0}{\omega\mu} [\bar{n}_{r_m}^0 \times \bar{u}_{\perp_m}^r \bar{E}_{\perp_m}^r] \exp(-j\beta_m^0 \bar{n}_{r_m}^0 \cdot \bar{r}) \\ & + \frac{\beta^e}{\omega\mu} [\bar{n}_{i_m}^e \times \bar{u}_{o_m}^e \bar{E}_{o_m}^i + \bar{n}_{i_m}^e \times \bar{u}_{\parallel_m}^i \bar{E}_{\parallel_m}^i] \exp(-j\beta_m^e \bar{n}_{i_m}^e \cdot \bar{r}) \\ & + \frac{\beta^e}{\omega\mu} [\bar{n}_{r_m}^e \times \bar{u}_{o_m}^e \bar{E}_{o_m}^r + \bar{n}_{r_m}^e \times \bar{u}_{\parallel_m}^r \bar{E}_{\parallel_m}^r] \exp(-j\beta_m^e \bar{n}_{r_m}^e \cdot \bar{r}) \end{aligned} \quad (12)$$

The next major objective in the derivation is to match the tangential components of the electric and magnetic intensity vectors at each interface. To accomplish this, it is expedient to have explicit expressions for the tangential components of \bar{E}_m and \bar{H}_m . To facilitate this matching of the fields and since the optic axes have been constrained to lie in the x-y plane, the optic axis in the m-th region will be specified by an orientation angle θ_m with respect to the x axis as shown in Figure 4. Thus,

$$\bar{u}_{o_m} = \cos \theta_m \bar{a}_x + \sin \theta_m \bar{a}_y + 0 \bar{a}_z \quad (13)$$

Matching tangential \bar{E} and \bar{H} at $z = d_m$ requires that

$$E_{x_{m+1}} = E_{x_m} \quad (14)$$

$$E_{y_{m+1}} = E_{y_m} \quad (15)$$

$$H_{x_{m+1}} = H_{x_m} \quad (16)$$

$$H_{y_{m+1}} = H_{y_m} \quad (17)$$

at $z = d_m$. Equation 14 can be written out explicitly using (4), (5), (9), and (10). The result is

$$\begin{aligned} & \cos \theta_{m+1} E_{o_{m+1}}^i e^{-j\beta_e^{m+1} n_{zi_{m+1}}^e d_m} + u_{x_{\perp m+1}}^i E_{\perp m+1}^i e^{-j\beta_e^o n_{zi_{m+1}}^o d_m} \\ & + u_{x_{\parallel m+1}}^i E_{\parallel m+1}^i e^{-j\beta_e^{m+1} n_{zi_{m+1}}^e d_m} + \cos \theta_{m+1} E_{o_{m+1}}^r e^{-j\beta_e^o n_{zr_{m+1}}^e d_m} \\ & + u_{x_{\perp m+1}}^r E_{\perp m+1}^r e^{-j\beta_e^o n_{zr_{m+1}}^o d_m} + u_{x_{\parallel m+1}}^r E_{\parallel m+1}^r e^{-j\beta_e^o n_{zr_{m+1}}^e d_m} \\ & = \cos \theta_m E_{o_m}^i e^{-j\beta_e^m n_{zi_m}^e d_m} + u_{x_{\perp m}}^i E_{\perp m}^i e^{-j\beta_e^o n_{zi_m}^o d_m} \\ & + u_{x_{\parallel m}}^i E_{\parallel m}^i e^{-j\beta_e^m n_{zi_m}^e d_m} + \cos \theta_m E_{o_m}^r e^{-j\beta_e^o n_{zr_m}^e d_m} \end{aligned}$$

$$+ u_{x_{\perp m}}^r E_{\perp m}^r e^{-j\beta_m^0 n_{zr_m}^o d_m} + u_{x_{\parallel m}}^r E_{\parallel m}^r e^{-j\beta_m^e n_{zr_m}^e d_m} \quad (18)$$

In a similar fashion (15) can be written as

$$\begin{aligned}
 & \sin \theta_{m+1} E_{o_{m+1}}^i e^{-j\beta_{m+1}^e n_{zi_{m+1}}^e d_m} + u_{y_{\perp m+1}}^i E_{\perp m+1}^i e^{-j\beta_{m+1}^0 n_{zi_{m+1}}^o d_m} \\
 & + u_{y_{\parallel m+1}}^i E_{\parallel m+1}^i e^{-j\beta_{m+1}^e n_{zi_{m+1}}^e d_m} + \sin \theta_{m+1} E_{o_{m+1}}^r e^{-j\beta_{m+1}^e n_{zr_{m+1}}^e d_m} \\
 & + u_{y_{\perp m+1}}^r E_{\perp m+1}^r e^{-j\beta_{m+1}^0 n_{zr_{m+1}}^o d_m} + u_{y_{\parallel m+1}}^r E_{\parallel m+1}^r e^{-j\beta_{m+1}^e n_{zr_{m+1}}^e d_m} \\
 & = \sin \theta_m E_{o_m}^i e^{-j\beta_m^e n_{zi_m}^e d_m} + u_{y_{\perp m}}^i E_{\perp m}^i e^{-j\beta_m^0 n_{zi_m}^o d_m} \\
 & + u_{y_{\parallel m}}^i E_{\parallel m}^i e^{-j\beta_m^e n_{zi_m}^e d_m} + \sin \theta_m E_{o_m}^r e^{-j\beta_m^e n_{zr_m}^e d_m} \\
 & + u_{y_{\perp m}}^r E_{\perp m}^r e^{-j\beta_m^0 n_{zr_m}^o d_m} + u_{y_{\parallel m}}^r E_{\parallel m}^r e^{-j\beta_m^e n_{zr_m}^e d_m} \quad (19)
 \end{aligned}$$

To simplify manipulations, it will be helpful to define the following terms. Let

$$e_m^o(d) = e^{-j\beta_m^0 n_{zi_m}^o d}$$

$$e_m^e(d) = e^{-j\beta_m^e n_{zi_m}^e d}$$

Then

$$\begin{aligned}
 e_{m+1}^0(d_m) &= e^{-j\beta_{m+1}^0 n_{zi_{m+1}}^0 d_m} \\
 e_{m+1}^e(d_m) &= e^{-j\beta_{m+1}^e n_{zi_{m+1}}^e d_m}
 \end{aligned} \tag{20}$$

and

$$\begin{aligned}
 e_m^0(d_m) &= e^{-j\beta_m^0 n_{zi_m}^0 d_m} \\
 e_m^e(d_m) &= e^{-j\beta_m^e n_{zi_m}^e d_m}
 \end{aligned} \tag{21}$$

Equations (20) and (21) will be used as a shorthand notation for the exponential terms in (18) and (19). Notice that since $n_{zr_m}^0 = -n_{zi_m}^0$ and $n_{zr_m}^e = -n_{zi_m}^e$, all exponential terms in (18) and (19) can be expressed by (20) or (21) or by their conjugates, e.g.,

$$e^{-j\beta_{m+1}^e n_{zr_{m+1}}^e d_m} = e_{m+1}^{e*}(d_m) \tag{22}$$

By linearity, each of the electric intensity components in (1-3) must satisfy the Maxwell equation

$$\bar{n} \cdot \bar{D} = \bar{n} \cdot \bar{\epsilon} \cdot \bar{E} = 0$$

or

$$\bar{n} \cdot \bar{\kappa} \cdot \bar{E} = 0 \tag{23}$$

For $\bar{E}_{i_m}^e$, (23) becomes with the aid of (9)

$$\bar{n}_{i_m}^e \cdot \left[\bar{\kappa}_m \cdot (\bar{u}_{o_m}^i E_{o_m}^i + \bar{u}_{\parallel_m}^i E_{\parallel_m}^i) \right] = 0$$

or

$$\begin{aligned} \bar{n}_{i_m}^e \cdot & \left[\bar{a}_x (\kappa_{x_m} \cos \theta_m E_{o_m}^i + \kappa_{x_m} u_{x\parallel_m}^i E_{\parallel_m}^i) \right. \\ & + \bar{a}_y (\kappa_{y_m} \sin \theta_m E_{o_m}^i + \kappa_{y_m} u_{y\parallel_m}^i E_{\parallel_m}^i) \\ & \left. + \bar{a}_z (\kappa_{z_m} u_{z\parallel_m}^i E_{\parallel_m}^i) \right] = 0 \end{aligned}$$

or

$$\begin{aligned} & \left[n_{x_i_m}^e \kappa_{x_m} \cos \theta_m + n_{y_i_m}^e \kappa_{y_m} \sin \theta_m \right] E_{o_m}^i \\ & + \left[n_{x_i_m}^e \kappa_{x_m} u_{x\parallel_m}^i + n_{y_i_m}^e \kappa_{y_m} u_{y\parallel_m}^i + n_{z_i_m}^e \kappa_{z_m} u_{z\parallel_m}^i \right] E_{\parallel_m}^i = 0 \end{aligned}$$

or

$$E_{\parallel_m}^i = C_{\parallel i_m} E_{o_m}^i \quad (24)$$

where

$$C_{\parallel i_m} = - \frac{n_{x_i_m}^e \kappa_{x_m} \cos \theta_m + n_{y_i_m}^e \kappa_{y_m} \sin \theta_m}{n_{x_i_m}^e \kappa_{x_m} u_{x\parallel_m}^i + n_{y_i_m}^e \kappa_{y_m} u_{y\parallel_m}^i + n_{z_i_m}^e \kappa_{z_m} u_{z\parallel_m}^i} \quad (25)$$

Equation (23) can also be applied to $\bar{E}_{r_m}^e$. Noting the similarity in form from (9) between $\bar{E}_{i_m}^e$ and $\bar{E}_{r_m}^e$, we can replace i by r in (24) and (25) and obtain

$$E_{\parallel_m}^r = C_{\parallel r_m} E_{o_m}^r \quad (26)$$

where

$$C_{\parallel r_m} = - \frac{n_{xr_m}^e \kappa_{x_m} \cos \theta_m + n_{yr_m}^e \kappa_{y_m} \sin \theta_m}{n_{xr_m}^e \kappa_{x_m} u_{x\parallel_m}^r + n_{yr_m}^e \kappa_{y_m} u_{y\parallel_m}^r + n_{zr_m}^e \kappa_{z_m} u_{z\parallel_m}^r} \quad (27)$$

Equations (24) and (26) can be used to eliminate the parallel components of the field in (19) and (20) and obtain

$$\begin{aligned}
 & \left[\cos \theta_{m+1} e_{m+1}^e(d_m) + u_{x\parallel_{m+1}}^i e_{m+1}^e(d_m) C_{\parallel i_{m+1}} \right] E_{o_{m+1}}^i \\
 & + \left[u_{x\perp_{m+1}}^i e_{m+1}^o(d_m) \right] E_{\perp_{m+1}}^i \\
 & + \left[\cos \theta_{m+1} e_{m+1}^{e*}(d_m) + u_{x\parallel_{m+1}}^r e_{m+1}^{e*}(d_m) C_{\parallel r_{m+1}} \right] E_{o_{m+1}}^r \\
 & + \left[u_{x\perp_{m+1}}^r e_{m+1}^{o*}(d_m) \right] E_{\perp_{m+1}}^r \\
 & = \left[\cos \theta_m e_m^e(d_m) + u_{x\parallel_m}^i e_m^e(d_m) C_{\parallel i_m} \right] E_{o_m}^i \\
 & + \left[u_{x\perp_m}^i e_m^o(d_m) \right] E_{\perp_m}^i \\
 & + \left[\cos \theta_m e_m^{e*}(d_m) + u_{x\parallel_m}^r e_m^{e*}(d_m) C_{\parallel r_m} \right] E_{o_m}^r \\
 & + \left[u_{x\perp_m}^r e_m^{o*}(d_m) \right] E_{\perp_m}^r \quad (28)
 \end{aligned}$$

and

$$\begin{aligned}
& \left[\sin \theta_{m+1} e_m^e(d_m) + u_{y\parallel m+1}^i e_m^e(d_m) c_{\parallel i_{m+1}} \right] E_{o_{m+1}}^i \\
& + \left[u_{y\perp m+1}^i e_m^o(d_m) \right] E_{\perp m+1}^i \\
& + \left[\sin \theta_{m+1} e_m^e(d_m) + u_{y\parallel m+1}^r e_m^e(d_m) c_{\parallel r_{m+1}} \right] E_{o_{m+1}}^r \\
& + \left[u_{y\perp m+1}^r e_m^o(d_m) \right] E_{\perp m+1}^r \\
& = \left[\sin \theta_m e_m^e(d_m) + u_{y\parallel m}^i e_m^e(d_m) c_{\parallel i_m} \right] E_{o_m}^i \\
& + \left[u_{y\perp m}^i e_m^o(d_m) \right] E_{\perp m}^i \\
& + \left[\sin \theta_m e_m^e(d_m) + u_{y\parallel m}^r e_m^e(d_m) c_{\parallel r_m} \right] E_{o_m}^r \\
& + \left[u_{y\perp m}^r e_m^o(d_m) \right] E_{\perp m}^r \tag{29}
\end{aligned}$$

The x and y components of (12) must be obtained in order to equate the magnetic field components at the interfaces. Obtaining these components is facilitated by using the vector identity

$$\bar{A} \times \bar{B} = \bar{a}_x (A_y B_z - A_z B_y) + \bar{a}_y (A_z B_x - A_x B_z) + \bar{a}_z (A_x B_y - A_y B_x)$$

Applying this identity to (12) allows (16) and (17) to be written, respectively, as

$$\begin{aligned}
& \beta_{m+1}^e \left[-n_{zi_{m+1}}^e \sin \theta_{m+1} \right] E_{o_{m+1}}^i e^{-j\beta_{m+1}^e n_{zi_{m+1}}^e d_m} \\
& + \beta_{m+1}^o \left[n_{yi_{m+1}}^o u_{z_{\perp m+1}}^i - n_{zi_{m+1}}^o u_{y_{\perp m+1}}^i \right] E_{\perp_{m+1}}^i e^{-j\beta_{m+1}^o n_{zi_{m+1}}^o d_m} \\
& + \beta_{m+1}^e \left[n_{yi_{m+1}}^e u_{z_{\parallel m+1}}^i - n_{zi_{m+1}}^e u_{y_{\parallel m+1}}^i \right] E_{\parallel_{m+1}}^i e^{-j\beta_{m+1}^e n_{zi_{m+1}}^e d_m} \\
& + \beta_{m+1}^e \left[-n_{zr_{m+1}}^e \sin \theta_{m+1} \right] E_{o_{m+1}}^r e^{-j\beta_{m+1}^e n_{zr_{m+1}}^e d_m} \\
& + \beta_{m+1}^o \left[n_{yr_{m+1}}^o u_{z_{\perp m+1}}^r - n_{zr_{m+1}}^o u_{y_{\perp m+1}}^r \right] E_{\perp_{m+1}}^r e^{-j\beta_{m+1}^o n_{zr_{m+1}}^o d_m} \\
& + \beta_{m+1}^e \left[n_{yr_{m+1}}^e u_{z_{\parallel m+1}}^r - n_{zr_{m+1}}^e u_{y_{\parallel m+1}}^r \right] E_{\parallel_{m+1}}^r e^{-j\beta_{m+1}^e n_{zr_{m+1}}^e d_m} \\
& = \beta_m^e \left[-n_{zi_m}^e \sin \theta_m \right] E_{o_m}^i e^{-j\beta_m^e n_{zi_m}^e d_m} \\
& + \beta_m^o \left[n_{yi_m}^o u_{z_{\perp m}}^i - n_{zi_m}^o u_{y_{\perp m}}^i \right] E_{\perp_m}^i e^{-j\beta_m^o n_{zi_m}^o d_m} \\
& + \beta_m^e \left[n_{yi_m}^e u_{z_{\parallel m}}^i - n_{zi_m}^e u_{y_{\parallel m}}^i \right] E_{\parallel_m}^i e^{-j\beta_m^e n_{zi_m}^e d_m} \\
& + \beta_m^e \left[-n_{zr_m}^e \sin \theta_m \right] E_{o_m}^r e^{-j\beta_m^e n_{zr_m}^e d_m} \\
& + \beta_m^o \left[n_{yr_m}^o u_{z_{\perp m}}^r - n_{zr_m}^o u_{y_{\perp m}}^r \right] E_{\perp_m}^r e^{-j\beta_m^o n_{zr_m}^o d_m} \\
& + \beta_m^e \left[n_{yr_m}^e u_{z_{\parallel m}}^r - n_{zr_m}^e u_{y_{\parallel m}}^r \right] E_{\parallel_m}^r e^{-j\beta_m^e n_{zr_m}^e d_m} \tag{30}
\end{aligned}$$

and

$$\begin{aligned}
& \beta_m^e \left[n_{zi_{m+1}}^e \cos \theta_{m+1} \right] E_{o_{m+1}}^i e^{-j\beta_{m+1}^e n_{zi_{m+1}}^e d_m} \\
& + \beta_m^o \left[n_{zi_{m+1}}^o u_{x_{\perp m+1}}^i - n_{xi_{m+1}}^o u_{z_{\perp m+1}}^i \right] E_{\perp_{m+1}}^i e^{-j\beta_{m+1}^o n_{zi_{m+1}}^o d_m} \\
& + \beta_m^e \left[n_{zi_{m+1}}^e u_{x_{\parallel m+1}}^i - n_{xi_{m+1}}^e u_{z_{\parallel m+1}}^i \right] E_{\parallel_{m+1}}^i e^{-j\beta_{m+1}^e n_{zi_{m+1}}^e d_m} \\
& + \beta_m^e \left[n_{zr_{m+1}}^e \cos \theta_{m+1} \right] E_{o_{m+1}}^r e^{-j\beta_{m+1}^e n_{zr_{m+1}}^e d_m} \\
& + \beta_m^o \left[n_{zr_{m+1}}^o u_{x_{\perp m+1}}^r - n_{xr_{m+1}}^o u_{z_{\perp m+1}}^r \right] E_{\perp_{m+1}}^r e^{-j\beta_{m+1}^o n_{zr_{m+1}}^o d_m} \\
& + \beta_m^e \left[n_{zr_{m+1}}^e u_{x_{\parallel m+1}}^r - n_{xr_{m+1}}^e u_{z_{\parallel m+1}}^r \right] E_{\parallel_{m+1}}^r e^{-j\beta_{m+1}^e n_{zr_{m+1}}^e d_m} \\
& = \beta_m^e \left[n_{zi_m}^e \cos \theta_m \right] E_{o_m}^i e^{-j\beta_m^e n_{zi_m}^e d_m} \\
& + \beta_m^o \left[n_{zi_m}^o u_{x_{\perp m}}^i - n_{xi_m}^o u_{z_{\perp m}}^i \right] E_{\perp_m}^i e^{-j\beta_m^o n_{zi_m}^o d_m} \\
& + \beta_m^e \left[n_{zi_m}^e u_{x_{\parallel m}}^i - n_{xi_m}^e u_{z_{\parallel m}}^i \right] E_{\parallel_m}^i e^{-j\beta_m^e n_{zi_m}^e d_m} \\
& + \beta_m^e \left[n_{zr_m}^e \cos \theta_m \right] E_{o_m}^r e^{-j\beta_m^e n_{zr_m}^e d_m} \\
& + \beta_m^o \left[n_{zr_m}^o u_{x_{\perp m}}^r - n_{xr_m}^o u_{z_{\perp m}}^r \right] E_{\perp_m}^r e^{-j\beta_m^o n_{zr_m}^o d_m}
\end{aligned}$$

$$+ \beta_m^e \left[n_{zr_m}^e u_{x\parallel m}^r - n_{xr_m}^e u_{z\parallel m}^r \right] E_{\parallel m}^r e^{-j\beta_m^e n_{zr_m}^e d_m} \quad (31)$$

Equations 30 and 31 can be simplified by using (20) and (21), (24) and (26).

The results, respectively, are

$$\begin{aligned}
& \beta_{m+1}^e \left[-n_{zi_{m+1}}^e \sin \theta_{m+1} e_{m+1}^e (d_m) + \left(n_{yi_{m+1}}^e u_{z\parallel m+1}^i - n_{zi_{m+1}}^e u_{y\parallel m+1}^i \right) \right. \\
& \quad \left. e_{m+1}^e (d_m) C_{\parallel i_{m+1}} \right] E_{\parallel i_{m+1}}^i \\
& + \beta_{m+1}^o \left[n_{yi_{m+1}}^o u_{z\perp m+1}^i - n_{zi_{m+1}}^o u_{y\perp m+1}^i \right] e_{m+1}^o (d_m) E_{\perp m+1}^i \\
& + \beta_{m+1}^e \left[-n_{zr_{m+1}}^e \sin \theta_{m+1} e_{m+1}^e (d_m) + \left(n_{yr_{m+1}}^e u_{z\parallel m+1}^r - n_{zr_{m+1}}^e u_{y\parallel m+1}^r \right) \right. \\
& \quad \left. e_{m+1}^e (d_m) C_{\parallel r_{m+1}} \right] E_{\parallel r_{m+1}}^r \\
& + \beta_{m+1}^o \left[n_{yr_{m+1}}^o u_{z\perp m+1}^r - n_{zr_{m+1}}^o u_{y\perp m+1}^r \right] e_{m+1}^o (d_m) E_{\perp m+1}^r \\
& = \beta_m^e \left[-n_{zi_m}^e \sin \theta_m e_m^e (d_m) + \left(n_{yi_m}^e u_{z\parallel m}^i - n_{zi_m}^e u_{y\parallel m}^i \right) \right. \\
& \quad \left. e_m^e (d_m) C_{\parallel i_m} \right] E_{\parallel i_m}^i \\
& + \beta_m^o \left[n_{yi_m}^o u_{z\perp m}^i - n_{zi_m}^o u_{y\perp m}^i \right] e_m^o (d_m) E_{\perp m}^i \\
& + \beta_m^e \left[-n_{zr_m}^e \sin \theta_m e_m^e (d_m) + \left(n_{yr_m}^e u_{z\parallel m}^r - n_{zr_m}^e u_{y\parallel m}^r \right) \right. \\
& \quad \left. e_m^e (d_m) C_{\parallel r_m} \right] z_{\parallel r_m}^r \\
& + \beta_m^o \left[n_{yr_m}^o u_{z\perp m}^r - n_{zr_m}^o u_{y\perp m}^r \right] e_m^o (d_m) E_{\perp m}^r
\end{aligned} \quad (32)$$

and

$$\begin{aligned}
 & \beta_{m+1}^e \left[n_{zi_{m+1}}^e \cos \theta_{m+1} e_{m+1}^e(d_m) + \left(n_{zi_{m+1}}^e u_{x \parallel m+1}^i - n_{xi_{m+1}}^e u_{z \parallel m+1}^i \right) \right. \\
 & \quad \left. e_{m+1}^e(d_m) C_{\parallel i_{m+1}} \right] E_{o_{m+1}}^i \\
 & + \beta_{m+1}^o \left[n_{zi_{m+1}}^o u_{x \perp m+1}^i - n_{xi_{m+1}}^o u_{z \perp m+1}^i \right] e_{m+1}^o(d_m) E_{\perp m+1}^i \\
 & + \beta_{m+1}^e \left[n_{zr_{m+1}}^e \cos \theta_{m+1} e_{m+1}^{e^*}(d_m) + \left(n_{zr_{m+1}}^e u_{x \parallel m+1}^r - n_{xr_{m+1}}^e u_{z \parallel m+1}^r \right) \right. \\
 & \quad \left. e_{m+1}^{e^*}(d_m) C_{\parallel r_{m+1}} \right] E_{o_{m+1}}^r \\
 & + \beta_{m+1}^o \left[n_{zr_{m+1}}^o u_{x \perp m+1}^r - n_{xr_{m+1}}^o u_{z \perp m+1}^r \right] e_{m+1}^{o^*}(d_m) E_{\perp m+1}^r \\
 & = \beta_m^e \left[n_{zi_m}^e \cos \theta_m e_m^e(d_m) + \left(n_{zi_m}^e u_{x \parallel m}^i - n_{xi_m}^e u_{z \parallel m}^i \right) \right] e_m^e(d_m) C_{\parallel i_m} \\
 & + \beta_m^o \left[n_{zi_m}^o u_{x \perp m}^i - n_{xi_m}^o u_{z \perp m}^i \right] e_m^o(d_m) E_{\perp m}^i \\
 & + \beta_m^e \left[n_{zr_m}^e \cos \theta_m e_m^{e^*}(d_m) + \left(n_{zr_m}^e u_{x \parallel m}^r - n_{xr_m}^e u_{z \parallel m}^r \right) \right] e_m^{e^*}(d_m) C_{\parallel r_m} \\
 & + \beta_m^o \left[n_{zr_m}^o u_{x \perp m}^r - n_{xr_m}^o u_{z \perp m}^r \right] e_m^{o^*}(d_m) E_{\perp m}^r \tag{33}
 \end{aligned}$$

An examination of (28), (29), (32), and (33) reveals that these four equations can be written in the following tensor form:

$$\bar{A}_{m+1}(d_m) \cdot \bar{E}_{m+1} = \bar{A}_m(d_m) \cdot \bar{E}_m \tag{34}$$

where \bar{E}_m and \bar{E}_{m+1} are column vectors and

$$\bar{E}_m = \begin{bmatrix} E^i_{\parallel m} \\ E^i_{\perp m} \\ E^r_{\parallel m} \\ E^r_{\perp m} \end{bmatrix} \quad (35)$$

and \bar{E}_{m+1} has the same form as \bar{E}_m with m replaced by $m+1$.

The tensors \bar{A}_m and \bar{A}_{m+1} have the same form only the subscripts are different. The argument d_m of these tensor functions, however, is the same for both. For an argument d , the form of these tensors is as follows:

$$\bar{A}_m(d) = \begin{bmatrix} A_{11} & A_{12} & A_{13} & A_{14} \\ A_{21} & A_{22} & A_{23} & A_{24} \\ A_{31} & A_{32} & A_{33} & A_{34} \\ A_{41} & A_{42} & A_{43} & A_{44} \end{bmatrix} \quad (36)$$

where

$$A_{11} = \left(\cos \theta_m + C_{\parallel i_m} u_{x\parallel m}^i \right) e_m^e(d)$$

$$A_{12} = u_{x\perp m}^i e_m^o(d)$$

$$A_{13} = \left(\cos \theta_m + C_{\parallel r_m} u_{x\parallel m}^r \right) e_m^{e^*}(d)$$

$$A_{14} = u_{x_{\perp m}}^r e_m^o (d)^*$$

$$A_{21} = \left(\sin \theta_m + c_{\parallel i_m} u_{y_{\parallel m}}^i \right) e_m^e (d)$$

$$A_{22} = u_{y_{\perp m}}^i e_m^o (d)$$

$$A_{23} = \left(\sin \theta_m + c_{\parallel r_m} u_{y_{\parallel m}}^r \right) e_m^e (d)^*$$

$$A_{24} = u_{y_{\perp m}}^r e_m^o (d)^*$$

$$A_{31} = \beta_m^e \left[-n_{zi_m}^e \sin \theta_m + c_{\parallel i_m} \left(n_{yi_m}^o u_{z_{\parallel m}}^i - n_{zi_m}^e u_{y_{\parallel m}}^i \right) \right] e_m^e (d)$$

$$A_{32} = \beta_m^o \left(n_{yi_m}^o u_{z_{\perp m}}^i - n_{zi_m}^o u_{y_{\perp m}}^i \right) e_m^o (d)$$

$$A_{33} = \beta_m^e \left[-n_{zr_m}^e \sin \theta_m + c_{\parallel r_m} \left(n_{yr_m}^e u_{z_{\parallel m}}^r - n_{zr_m}^e u_{y_{\parallel m}}^r \right) \right] e_m^e (d)^*$$

$$A_{34} = \beta_m^o \left(n_{yr_m}^o u_{z_{\perp m}}^r - n_{zr_m}^o u_{y_{\perp m}}^r \right) e_m^o (d)^*$$

$$A_{41} = \beta_m^e \left[n_{zi_m}^e \cos \theta_m + c_{\parallel i_m} \left(n_{zi_m}^e u_{x_{\parallel m}}^i - n_{xi_m}^e u_{z_{\parallel m}}^i \right) \right] e_m^e (d)$$

$$A_{42} = \beta_m^o \left(n_{zi_m}^o u_{x_{\perp m}}^i - n_{xi_m}^o u_{z_{\perp m}}^i \right) e_m^o (d)$$

$$\begin{aligned}
 A_{43} &= \beta_m^e \left[n_{zr_m}^e \cos \theta_m + C_{\parallel r_m} \left(n_{zr_m}^e u_{x\parallel_m}^r - n_{xr_m}^e u_{z\parallel_m}^r \right) \right] e_m^e (d) \\
 A_{44} &= \beta_m^o \left(n_{zr_m}^o u_{x\perp_m}^r - n_{xr_m}^o u_{z\perp_m}^r \right) e_m^o (d)
 \end{aligned} \tag{37}$$

The system of equations (34) applies at each interface. This group of equations can be solved by the following procedure. First, invert the tensor on the left side of (34) and obtain

$$\bar{E}_{m+1} = \bar{B}_m \cdot \bar{E}_m \tag{38}$$

where

$$\bar{B}_m = \bar{A}_{m+1}^{-1}(d_m) \cdot \bar{A}_m(d_m) \tag{39}$$

Thus

$$\begin{aligned}
 \bar{E}_2 &= \bar{B}_1 \cdot \bar{E}_1 \\
 \bar{E}_3 &= \bar{B}_2 \cdot \bar{E}_2 \\
 &\vdots \\
 \bar{E}_N &= \bar{B}_{N-1} \cdot \bar{E}_{N-1}
 \end{aligned} \tag{40}$$

From (40) it can be seen that

$$\bar{E}_N = \bar{C} \cdot \bar{E}_1 \tag{41}$$

where

$$\bar{C} = \bar{B}_{N-1} \cdot \bar{B}_{N-2} \cdot \bar{B}_{N-3} \cdots \bar{B}_2 \cdot \bar{B}_1 \tag{42}$$

Since medium N is semi-infinite, there is no reflected field in this region; hence, $E_{o_N}^r = E_{\perp m}^r = 0$. Thus, the tensor equation (41) can be partitioned in the following manner

$$\begin{bmatrix} E_{o_N}^i \\ E_{\perp N}^i \\ 0 \\ 0 \end{bmatrix} = \begin{bmatrix} C_{11} & C_{12} & C_{13} & C_{14} \\ C_{21} & C_{22} & C_{23} & C_{24} \\ C_{31} & C_{32} & C_{33} & C_{34} \\ C_{41} & C_{42} & C_{43} & C_{44} \end{bmatrix} \cdot \begin{bmatrix} E_{o_1}^i \\ E_{\perp 1}^i \\ E_{o_1}^r \\ E_{\perp 1}^r \end{bmatrix} \quad (43)$$

This last equation can be rewritten as

$$\begin{aligned} \bar{E}_t &= \bar{F}_1 \cdot \bar{E}_i + \bar{F}_2 \cdot \bar{E}_r \\ \bar{0} &= \bar{F}_3 \cdot \bar{E}_i + \bar{F}_4 \cdot \bar{E}_r \end{aligned} \quad (44)$$

where

$$\bar{E}_t = \begin{bmatrix} E_{o_N}^i \\ E_{\perp N}^i \end{bmatrix} \quad (45)$$

$$\bar{E}_i = \begin{bmatrix} E_{o_1}^i \\ E_{\perp 1}^i \end{bmatrix} \quad (46)$$

$$\bar{E}_r = \begin{bmatrix} E_{o_1}^r \\ E_{\perp 1}^r \end{bmatrix} \quad (47)$$

$$\begin{aligned}
 \bar{\mathbf{F}}_1 &= \begin{bmatrix} c_{11} & c_{12} \\ c_{21} & c_{22} \end{bmatrix} & \bar{\mathbf{F}}_2 &= \begin{bmatrix} c_{13} & c_{14} \\ c_{23} & c_{24} \end{bmatrix} \\
 \bar{\mathbf{F}}_3 &= \begin{bmatrix} c_{31} & c_{32} \\ c_{41} & c_{42} \end{bmatrix} & \bar{\mathbf{F}}_4 &= \begin{bmatrix} c_{33} & c_{34} \\ c_{43} & c_{44} \end{bmatrix}
 \end{aligned} \tag{48}$$

and $\bar{0}$ is a two element column matrix of zeros.

In most applications, the incident field \bar{E}_i is known and the transmitted field \bar{E}_t and the reflected field \bar{E}_r must be found. These two fields can be obtained from (44) and are

$$\bar{E}_r = -\bar{\mathbf{F}}_4^{-1} \cdot \bar{\mathbf{F}}_3 \cdot \bar{E}_i \tag{49}$$

$$\bar{E}_t = (\bar{\mathbf{F}}_1 - \bar{\mathbf{F}}_2 \cdot \bar{\mathbf{F}}_4^{-1} \cdot \bar{\mathbf{F}}_3) \cdot \bar{E}_i \tag{50}$$

The incident, reflected and transmitted fields in (49) and (50) are specified in terms of optic axis coordinate systems. For more convenient usage they need to be expressed in terms of rectangular coordinate components. If the incident field in rectangular components in medium given by

$$\bar{E}_i = (E_x, E_y, E_z) \tag{51}$$

then

$$E_{o_1}^i = \bar{E}_i \cdot \bar{u}_{o_1}$$

or

$$E_{o_1}^i = E_x \cos \theta_1 + E_y \sin \theta_1 \quad (52)$$

Also

$$E_{\perp 1}^i = \bar{E}_i \cdot \bar{u}_{\perp 1}^i$$

or

$$E_{\perp 1}^i = E_x u_{x\perp 1}^i + E_y u_{y\perp 1}^i + E_z u_{z\perp 1}^i \quad (53)$$

From (46) it can be seen that (50) through (53) specify \bar{E}_i .

If the incident wave in region 1 is propagating in a direction specified by the spherical coordinate angles (θ_i, ϕ_i) shown in Figure 5, then

$$\bar{n}_{i_1}^o = (n_{xi_1}^o, n_{yi_1}^o, n_{zi_1}^o) \quad (54)$$

where

$$n_{xi_1}^o = \sin \theta_i \cos \phi_i$$

$$n_{yi_1}^o = \sin \theta_i \sin \phi_i$$

$$n_{zi_1}^o = \cos \theta_i \quad (55)$$

It will be assumed, of course, that only one wave, the ordinary wave, is incident in region 1.

The transmitted \bar{E}_t and reflected field \bar{E}_r are expressed in optic-axis coordinate components and need to be converted in rectangular components. If $\bar{E} = (E_o, E_{\perp}, E_{\parallel})$ is the optic axis representation, then the rectangular components are

$$E_x = \bar{E} \cdot \bar{a}_x$$

$$E_y = \bar{E} \cdot \bar{a}_y$$

$$E_z = \bar{E} \cdot \bar{a}_z$$

Now

$$\bar{u}_o = \cos \theta \bar{a}_x + \sin \theta \bar{a}_y + 0 \bar{a}_z$$

$$\bar{u}_\perp = u_{x\perp} \bar{a}_x + u_{y\perp} \bar{a}_y + u_{z\perp} \bar{a}_z$$

$$\bar{u}_{\parallel} = u_{x\parallel} \bar{a}_x + u_{y\parallel} \bar{a}_y + u_{z\parallel} \bar{a}_z$$

Thus

$$\begin{bmatrix} \bar{a}_x \\ \bar{a}_y \\ \bar{a}_z \end{bmatrix} = \bar{P}^{-1} \cdot \begin{bmatrix} \bar{u}_o \\ \bar{u}_\perp \\ \bar{u}_{\parallel} \end{bmatrix} = \begin{bmatrix} Q_{11} & Q_{12} & Q_{13} \\ Q_{21} & Q_{22} & Q_{23} \\ Q_{31} & Q_{32} & Q_{33} \end{bmatrix} \cdot \begin{bmatrix} \bar{u}_o \\ \bar{u}_\perp \\ \bar{u}_{\parallel} \end{bmatrix}$$

where $\bar{Q} = \bar{P}^{-1}$ and where

$$\bar{P} = \begin{bmatrix} \cos \theta & \sin \theta & 0 \\ u_{x\perp} & u_{y\perp} & u_{z\perp} \\ u_{x\parallel} & u_{y\parallel} & u_{z\parallel} \end{bmatrix}$$

Thus

$$E_x = E_o Q_{11} + E_\perp Q_{12} + E_{\parallel} Q_{13}$$

$$E_y = E_o Q_{21} + E_\perp Q_{22} + E_{\parallel} Q_{23}$$

$$E_z = E_o Q_{31} + E_\perp Q_{32} + E_{\parallel} Q_{33}$$

Thus for the reflected field

$$\begin{aligned}
 E_{x_1}^r &= E_{o_1}^r Q_{11} + E_{\perp_1}^r Q_{12} + E_{\parallel_1}^r Q_{13} \\
 E_{y_1}^r &= E_{o_1}^r Q_{21} + E_{\perp_1}^r Q_{22} + E_{\parallel_1}^r Q_{23} \\
 E_{z_1}^r &= E_{o_1}^r Q_{31} + E_{\perp_1}^r Q_{32} + E_{\parallel_1}^r Q_{33}
 \end{aligned} \tag{56}$$

where

$$\bar{Q} = \bar{P}^{-1} \tag{57}$$

and

$$\bar{P} = \begin{bmatrix} \cos \theta_1 & \sin \theta_1 & 0 \\ u_{x\perp_1}^r & u_{y\perp_1}^r & u_{z\perp_1}^r \\ u_{x\parallel_1}^r & u_{y\parallel_1}^r & u_{z\parallel_1}^r \end{bmatrix} \tag{58}$$

while for the transmitted field

$$\begin{aligned}
 E_{x_N}^i &= E_{o_N}^i S_{11} + E_{\perp_N}^i S_{12} + E_{\parallel_N}^i S_{13} \\
 E_{y_N}^i &= E_{o_N}^i S_{21} + E_{\perp_N}^i S_{22} + E_{\parallel_N}^i S_{23} \\
 E_{z_N}^i &= E_{o_N}^i S_{31} + E_{\perp_N}^i S_{32} + E_{\parallel_N}^i S_{33}
 \end{aligned} \tag{59}$$

where

$$\bar{S} = \bar{T}^{-1} \tag{60}$$

and

$$T = \begin{bmatrix} \cos \theta_N & \sin \theta_N & 0 \\ u_x^i & u_y^i & u_z^i \\ u_x^i & u_y^i & u_z^i \end{bmatrix} \quad (61)$$

The components of E parallel to the optic axes can be eliminated using (26) and (24) which give, respectively,

$$E_{\parallel 1}^r = C_{\parallel r_1} E_{o_1}^r$$

$$E_{\parallel N}^i = C_{\parallel i_N} E_{o_N}^i$$

This analysis has been programmed on a digital computer, and the broad-band panels have been evaluated. The predicted transmission data versus the measured data are presented in Section V.

SECTION III
BROADBAND PANEL DESIGN

The design of the panels that were tested during this program are presented in this section.

1. Panel No. 1

The spacing, 2ℓ , of the grooves and the thickness, d , of the panel were chosen to be 0.25-inch and 1.5 inches, respectively, as indicated in Section II. The spacing of the grooves was chosen on the basis of designing a panel that would operate satisfactorily from 9 GHz through 16 GHz. The depth of the grooves was chosen to be 0.625-inch and it was felt that this would be a sufficient depth for operation over the 9-16 GHz frequency band.

The panel was machined from a 1.5-inch thickness Rexolite[®] 1522 material which has a relative dielectric constant of 2.54 and a loss tangent of 0.0002. The grooves were machined horizontally on the front surface and vertically on the rear surface. This type groove orientation was chosen to obtain the same insertion phase delays for horizontal and vertical polarization.

The panel dimensions were 24 inches by 24 inches by 1.5 inches. This was sufficient size to obtain free space transmission measurement data. These data were measured at incidence angles of 0° to 60° in 5° increments for both polarizations. These data are presented in Section IV. A photograph of Panel No. 1 is shown in Figure 6.

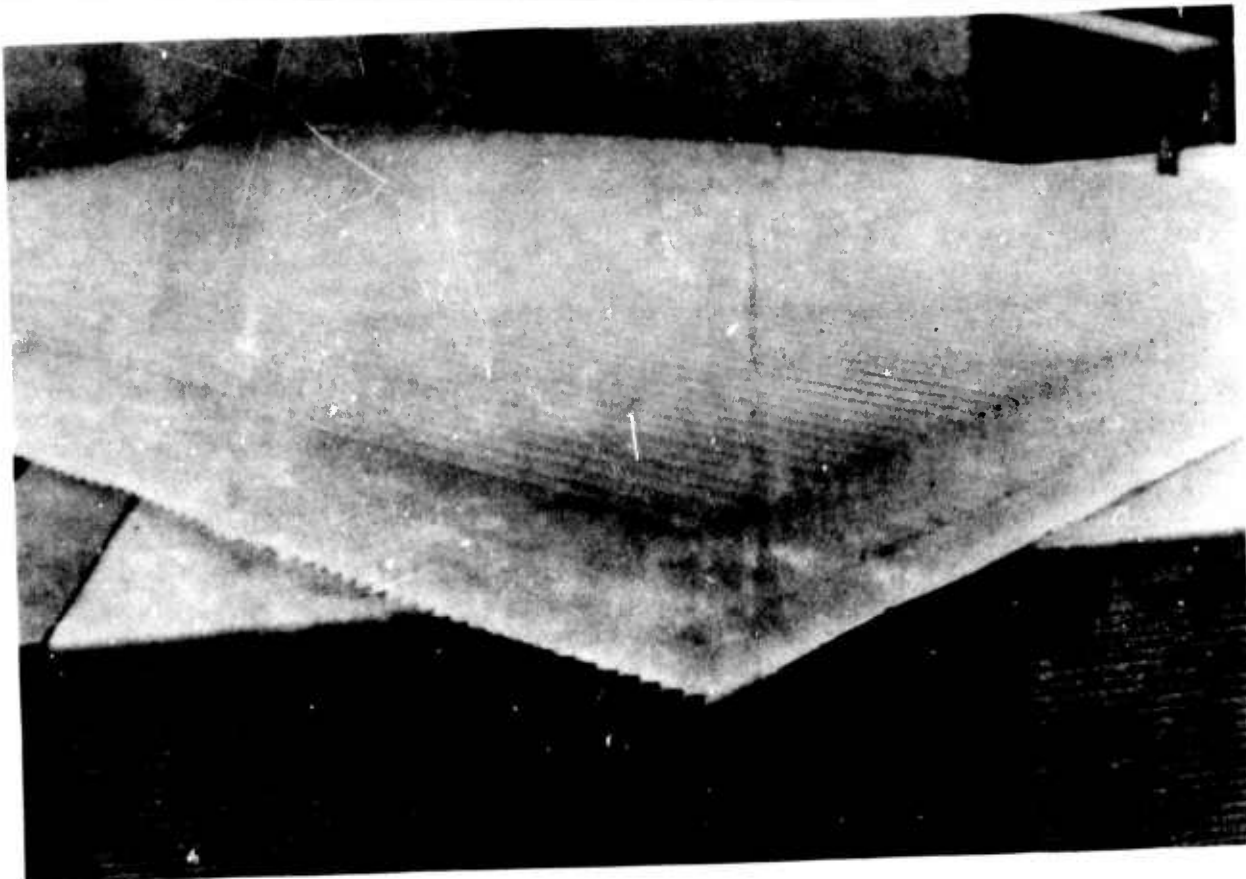


Figure 6. Panel No. 1 (Groove Spacing = 0.25").

2. Panel No. 2

To increase the upper frequency to at least 36 GHz, Panel No. 2 was designed with a groove spacing of 0.125-inch. All other dimensions were the same as Panel No. 1. Rexolite[®] 1522 was again used as the panel material. The tapered grooves were machined and due to the close spacing between grooves, sharp edges of the tips could not be maintained. This was not noticeable in the measurement data.

Free space transmission measurements were made on Panel No. 2 from 2 GHz to 36 GHz, and these data are presented in Section IV. The bandwidth of the panel was from 4 GHz to 36 GHz (bandwidth is defined herein as 90 percent or better power transmission coefficient).

3. Pyramidal Panel

A third Rexolite[®] panel was machined with pyramids on each surface instead of the grooves. The tip-to-tip spacing of the pyramids was 0.25-inch which was similar to Panel No. 1. Again, the overall dimensions of the panel were 24 inches by 24 inches by 1.5 inches. Transmission data were taken on this panel and differed very little from the data of Panel No. 1. Some of these results are presented in Section IV. A photograph of the pyramidal panel is shown in Figure 7.

The pyramidal panel was then modified in a number of ways to determine the effects of a rain erosion coating on the outer surface and to determine the effects of foam-filled grooves.

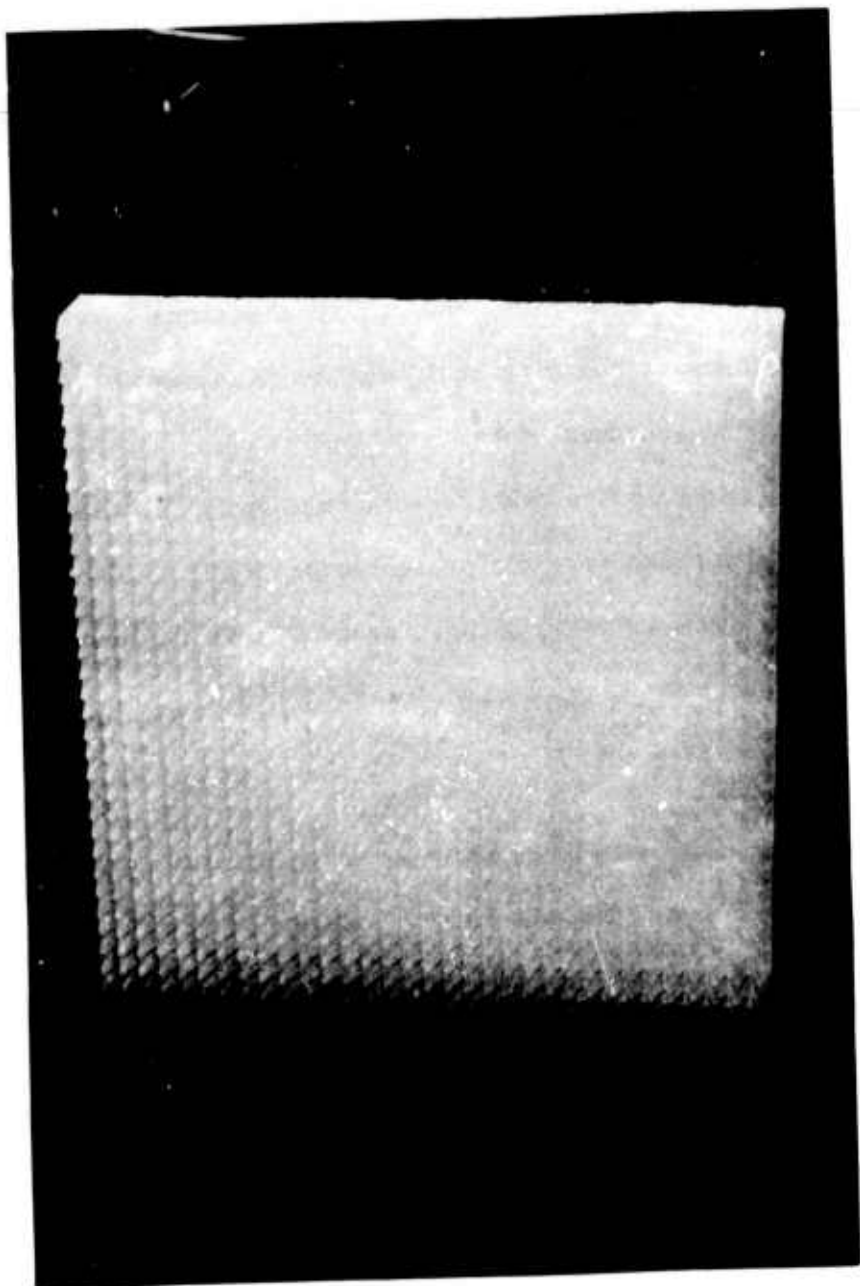


Figure 7. Pyramidal Grooved Panel.

a. Mylar Coating

Since the grooved or pyramidal panels do not present a smooth exterior surface, it was decided to place a rain erosion coating over the pyramidal panel. A sheet of 0.005-inch thick Mylar was first placed over one surface of the pyramidal panel. Measurements were performed to determine the change in transmission characteristics due to the Mylar sheet. These data are presented in Section IV.

b. Rain Erosion Coating

A standard Astrocoat 7110 rain erosion coating was painted onto the Mylar surface of the pyramidal panel. Three thicknesses were used: 0.005-inch, 0.010-inch and 0.020-inch. Free space transmission measurements were performed for each thickness and these data are discussed in Section IV.

c. Foam Filled Grooves

Another technique used in obtaining a smooth outer surface without degrading the broadband characteristics of the pyramidal panel was that of filling the grooves with a low density, low loss foam. Type EP-3 Isofoam was used to fill the grooves of the pyramidal panel. Free space transmission measurements were performed on the panel as well as antenna radiation patterns of an antenna placed behind the panel. These data are presented in Section IV.

4. Curved Panel Design

An important application of a broadband antenna window is that of protecting aircraft ECM antennas. Some of these multi-band antennas are located on the leading edge of the aircraft wing. To simulate this case, a curved

broadband panel was designed and fabricated. The radius of curvature of the panel was 2.5 inches. The panel shape was that of a half-cylinder with a length of 16 inches. Vertically tapered grooves were machined into the outer surface and on the inner surface were machined horizontally tapered grooves (Figure 8). The spacing of the grooves was 0.25-inch, similar to Panel No. 1.

To better compare the effects of panel curvature, the thickness of the tapered grooves and the groove spacing were the same as Panel No. 1. Transmission tests and antenna radiation pattern data were also made with this panel.

To determine the effects of a thin protective cover, a fiber glass sheet was placed over the exterior surface of the curved panel. Amplitude and phase transmission data were obtained on this configuration. In addition, antenna radiation patterns were made, and all of the data are presented in Section IV.

5. High Dielectric Constant Panel Design (Panel No. 3)

To observe the effect of a higher dielectric constant on the panel design, a third panel was machined with the following parameters:

$$d = 0.625 \text{ inch},$$

$$2l = 0.25 \text{ inch},$$

$$\frac{K_r}{r} = 9.0$$

total thickness = 1.5 inches,

height = 24 inches,

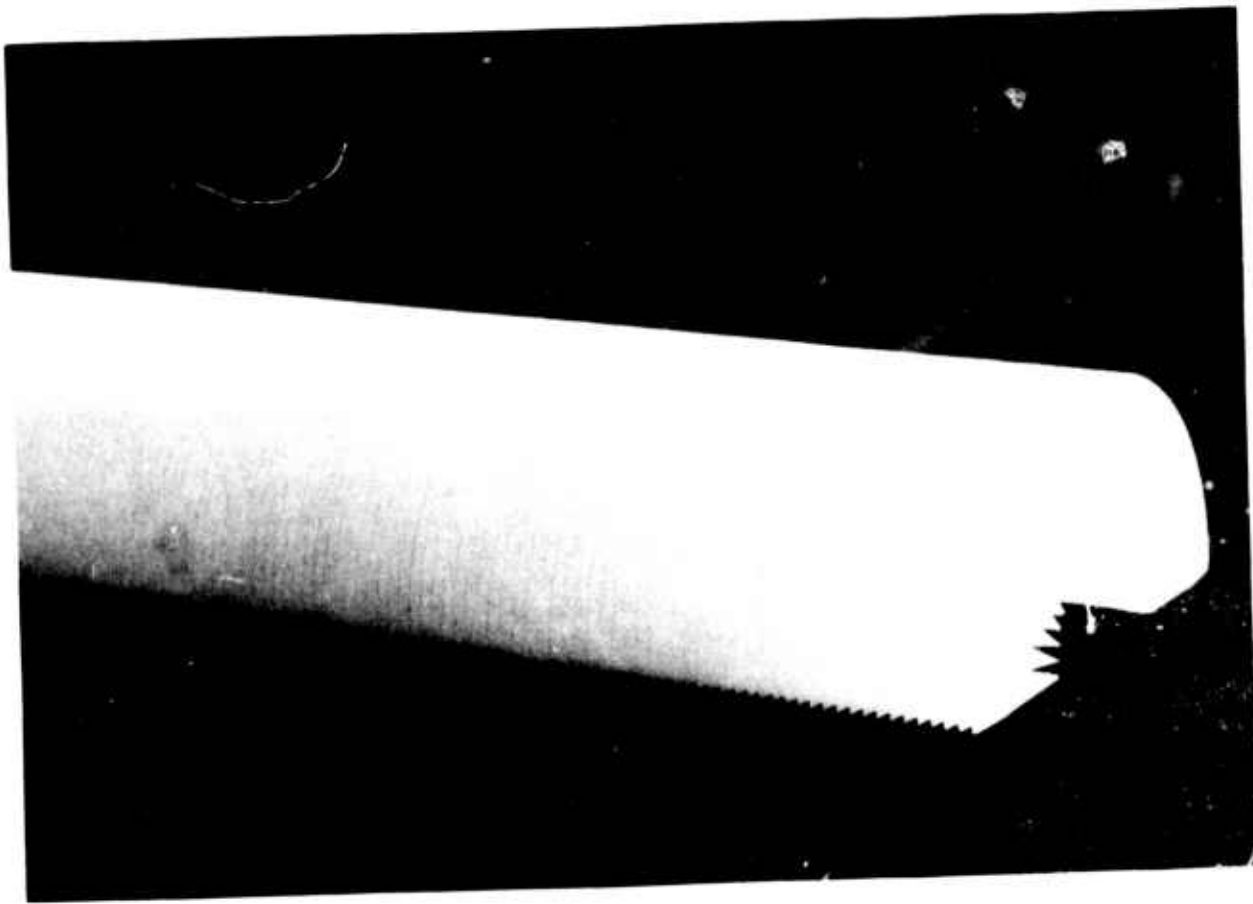


Figure 8. Cylindrical Broadband Panel.

width = 24 inches, and

material = Emerson and Cuming Styrocast Hi-K.

In summary, the bandwidth of the third panel decreased considerably as compared to the lower dielectric constant panels. This is partly evident from Equation 1, since an increase in dielectric constant will cause an increase in the denominator of Equation 1. Thus, the groove spacing decreases as dielectric constant increases. Since Panel No. 3 was machined with a groove spacing of 0.25 inch, the bandwidth decreased considerably.

SECTION IV

MEASURED RESULTS

Most of the data on Panels No. 1 and No. 2 have been presented in the Interim Report [1]. For completeness, these data are included in this section of this report. Additional data included are the results of the Mylar cover over the pyramidal panel, the rain erosion coating and the foam filled grooves of the pyramidal panel. The transmission data obtained on the curved panel and the antenna radiation pattern measurements are also included in this section.

1. Free-Space Measurement Technique

The transmission properties of each panel were determined by using a microwave phase shift bridge technique. The insertion phase and insertion loss of each panel were measured as functions of frequency, incidence angle, and polarization. The microwave bridge was composed of a reference arm and a sample arm so that phase information could be obtained.

Two horn antennas were mounted in the sample arm. A reference test panel was mounted perpendicular to the horn transmission axis, and the data measuring system was adjusted and calibrated so that the reference test panel measured transmission properties approached those of a theoretical flat panel. Upon completion of the reference flat panel measurements, the test panel under consideration was placed into the test fixture. Transmission measurements were performed at 1.0 GHz intervals over each waveguide band of interest. Radiation pattern measurements were made at selected frequencies using the panels as antenna windows.

2. Panel No. 1 and Panel No. 2 Measured Results

The insertion loss and insertion phase shift of these two panels are presented in Figures 9, 10, 11 and 12. The plots are for the 0° and 60° cases only. The data of incidence angles between 0° and 60°, in general, fell between the two curves on each graph. Both horizontal and vertical polarization data are shown. In comparing the phase data, it is significant to note that the insertion phase shifts of the two polarizations are nearly the same. This indicates that the panel has good circular polarization transmission properties.

The amplitude data for both panels show very little insertion loss over the broad frequency range. As indicated in Figure 9, the insertion loss for Panel No. 1 is very low from about 4 GHz to 18 GHz. Panel No. 2 has excellent transmission properties from 4 GHz to at least 36 GHz. This is a 9:1 frequency bandwidth which is remarkable for a panel fabricated from a single material.

3. Pyramidal Panel

As previously stated, the transmission properties of the pyramidal panel are about the same as those of Panel No. 1. The upper and lower cut-off frequencies are about the same as Panel No. 1. This is due to the 0.25-inch groove spacing and to the depth of the groove.

The pyramidal panel was used for a number of experiments during the program. There has been apprehension about the aerodynamics of the broad-band panel, so three methods of smoothing the outer surface of the panel have been evaluated. They are discussed in the following paragraphs.

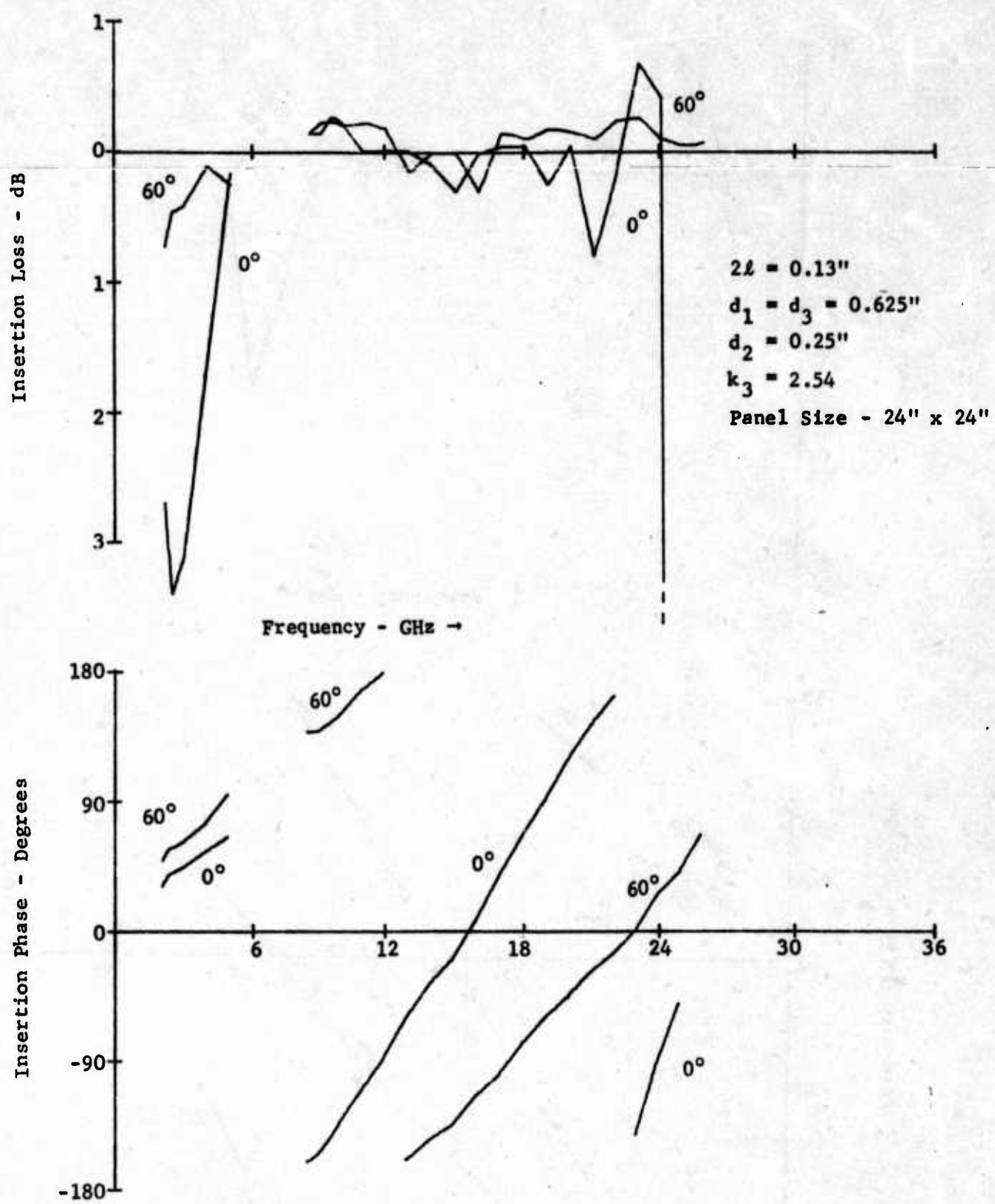


Figure 9. Panel #1 Transmission Properties - Vertical Polarization (0° and 60° Incidence Angles).

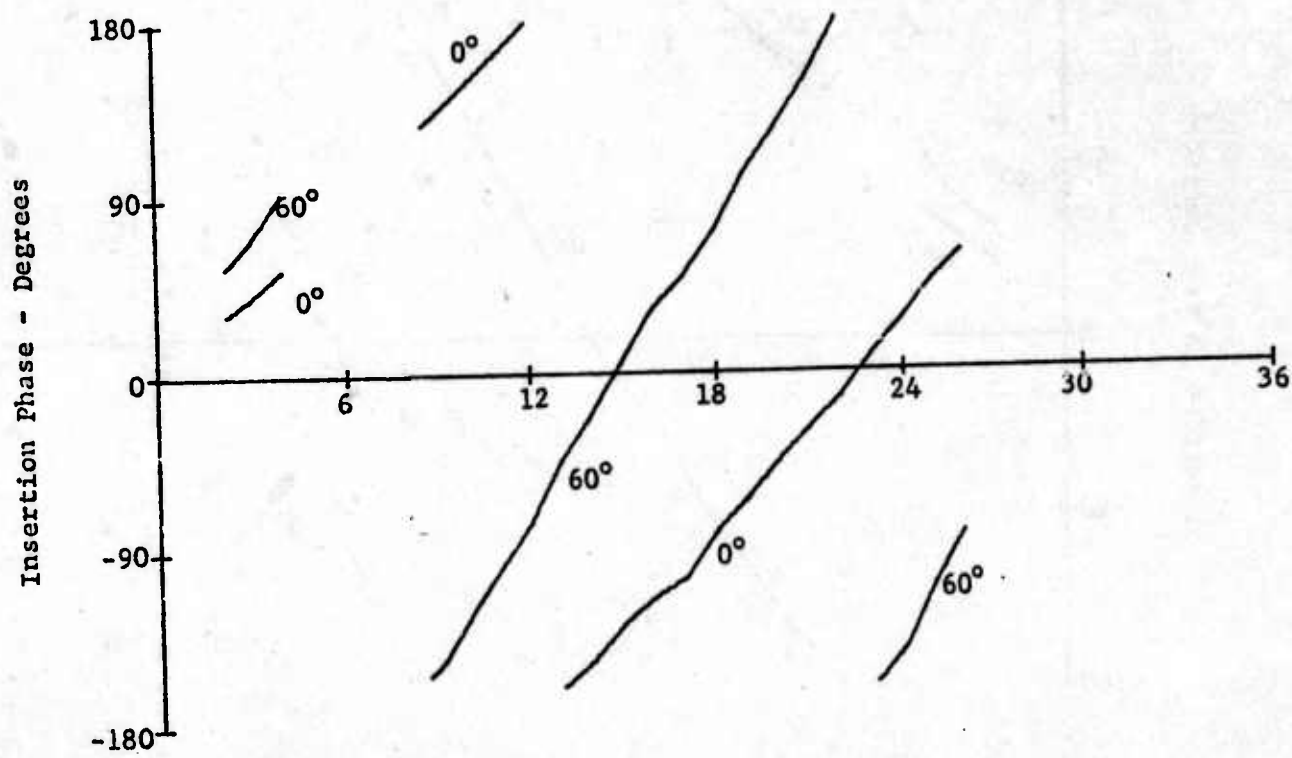
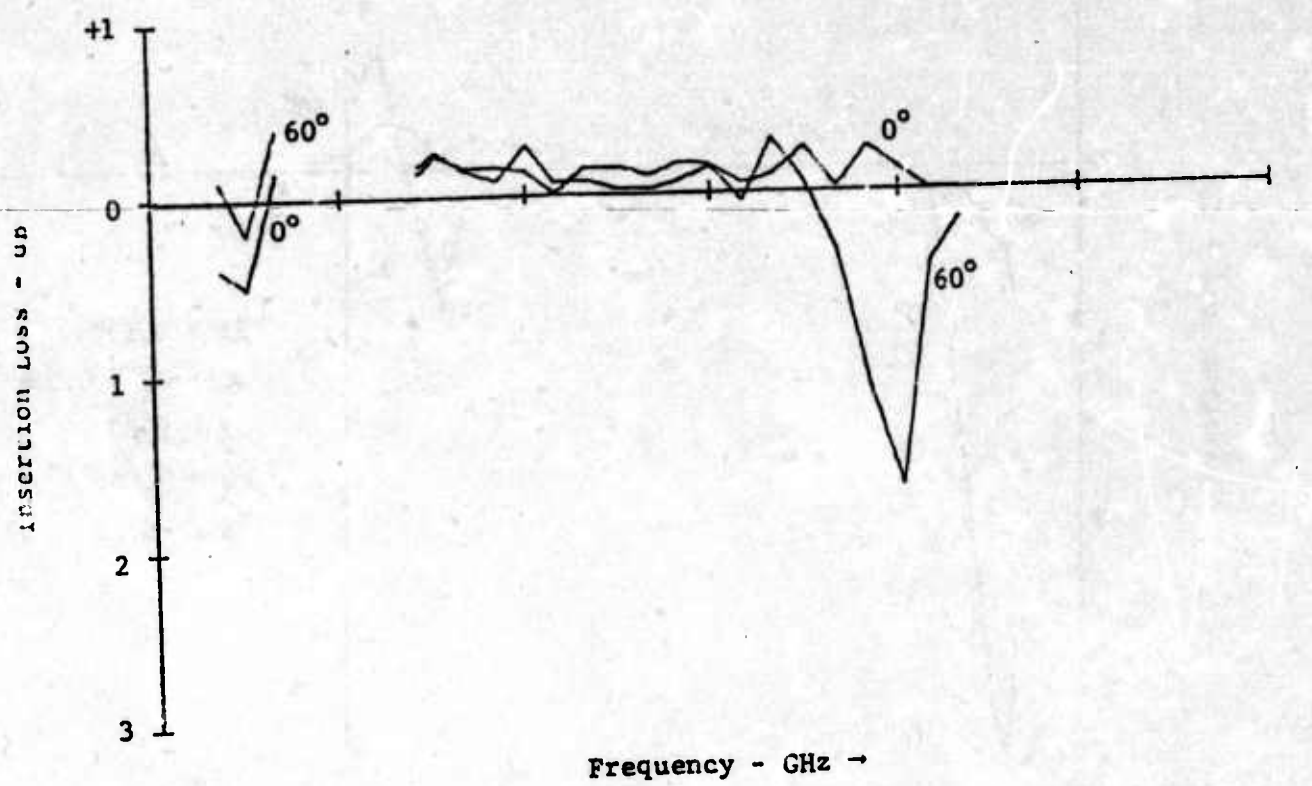


Figure 10. Panel #1 Transmission Properties -
Horizontal Polarization.

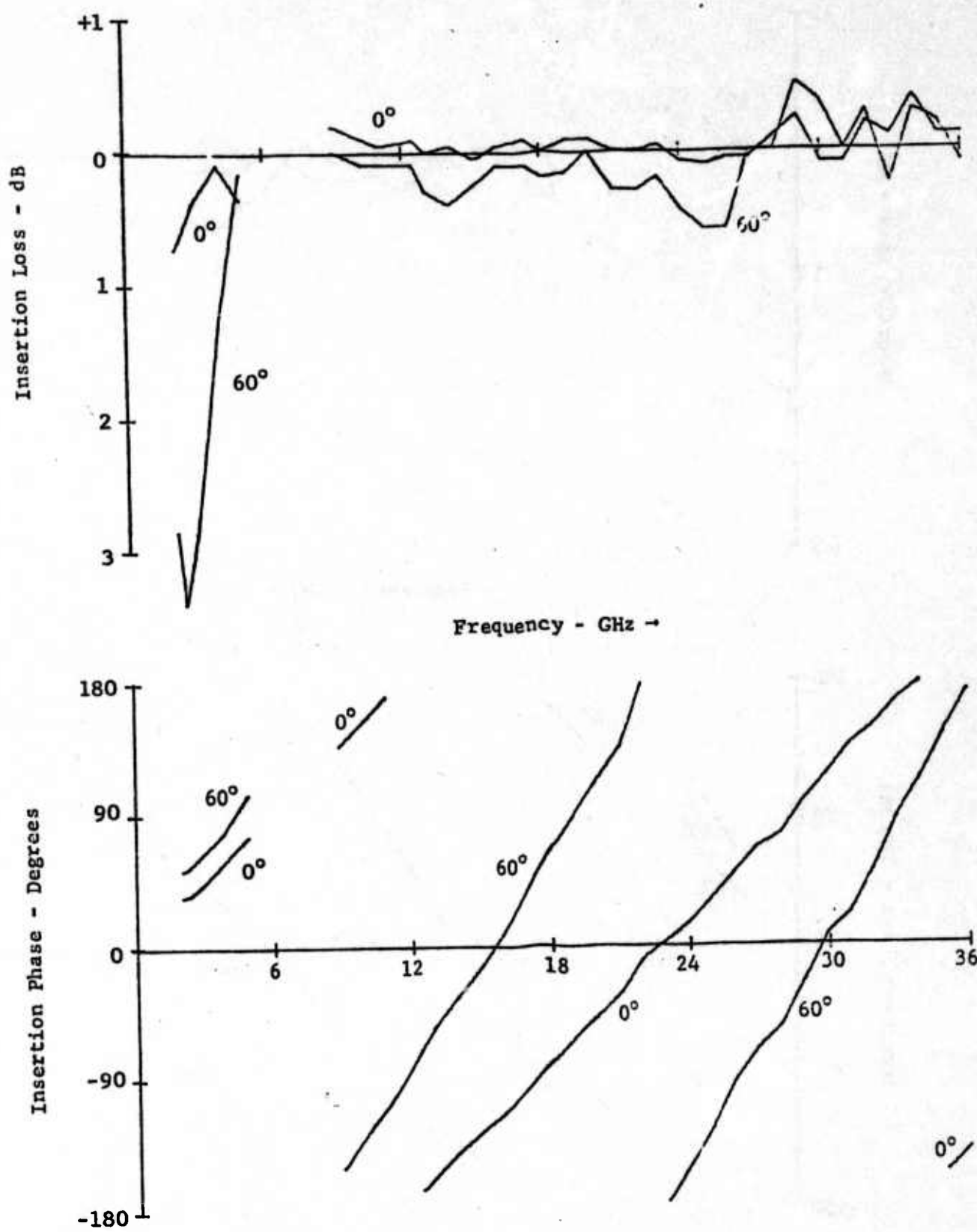


Figure 11. Panel #2 Transmission Properties - Vertical Polarization.

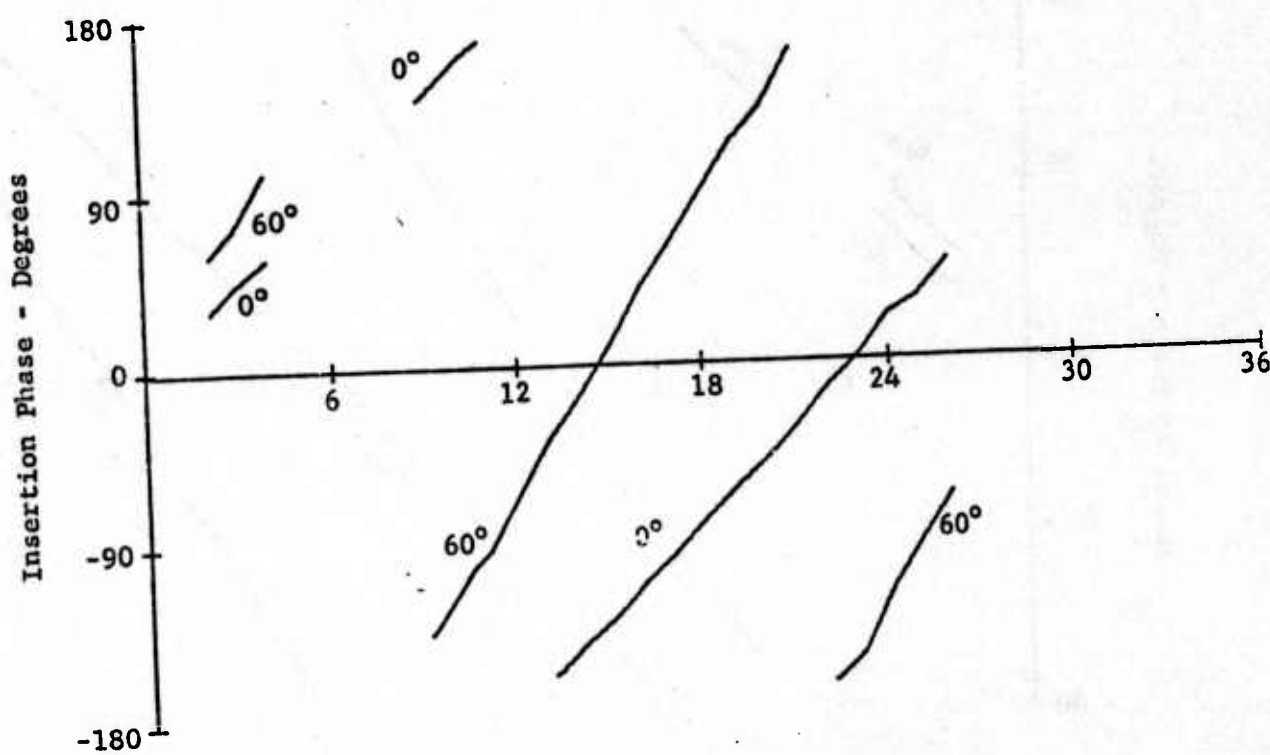
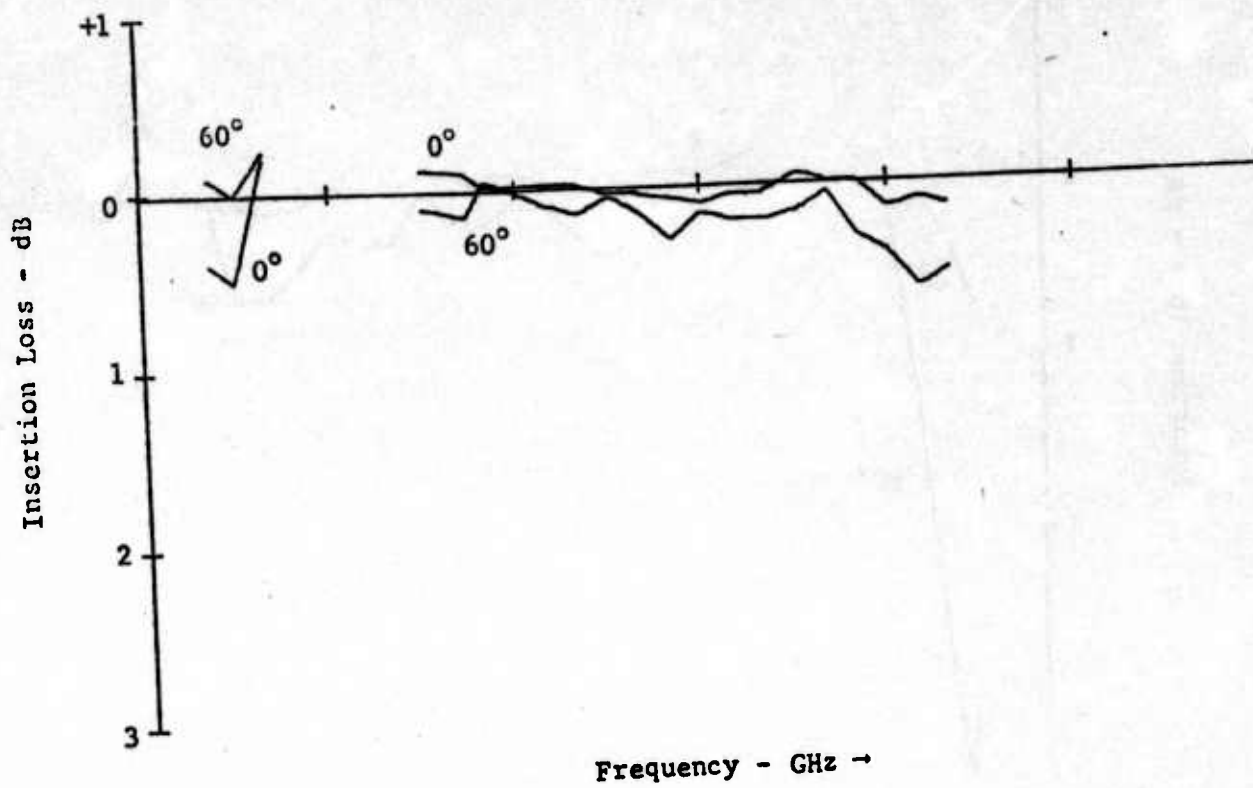


Figure 12. Panel #2 Transmission Properties -
Horizontal Polarization.

a. Mylar Coated Pyramidal Grooves

One of the approaches to obtain a smooth aerodynamic panel shape was to cover the external surface with a rain erosion coating. The rain erosion coating was applied to a thin sheet of Mylar and the combination Mylar/coating covered the pyramidal panel. Transmission tests were made of the panel and the mylar coating. Little, if any, effects were noted. A slight increase in insertion phase shift was measured.

b. Rain Erosion Coating over Pyramidal Grooves

The Olin Astrocoat 7110 rain erosion coating was applied in thicknesses of 0.005-inch, 0.010-inch, and 0.020-inch to the Mylar sheet. Transmission measurements were made on the broadband panel for each thickness coating. For the 0.005-inch rain erosion coating, the typical X-band insertion phase increased by about 5 degrees and the change in transmission loss was less than 0.1 dB from 0° to 60° angles of incidence. In the K_u -band frequency range, the transmission loss remained constant at 0.1 dB while the insertion phase delay increased from 5° to 9°. These values are valid for both linear polarizations.

The Mylar sheet was coated with a 0.010-inch thick rain erosion coating and placed on the outer surface of the pyramidal grooved panel. For frequencies between 8 GHz and 13 GHz, the measured transmission loss was near constant at about 0.3 dB while the insertion phase delay increased from 10° to 13°. These values hold for both linear polarizations and for angles of incidence less than 10°.

At frequencies between 14 GHz and 18 GHz, the transmission loss remained at 0.3 dB for horizontal polarization to 60° and for vertical

polarization to 40°. The vertical polarization transmission deteriorates above 40° incidence angle and decreased by 1.3 dB at 60° angle of incidence. The phase change was very smooth (13-17 degrees) to 60°.

The 0.005-inch thickness mylar sheet was coated with several layers of the Astrocoat until a combined thickness of 0.020-inch was obtained. This sheet was then used as a cover for the pyramidal plate, in both the foamed and unfoamed configurations, while transmission data were taken.

Very little amplitude change was noted for horizontal polarization, while significant changes occurred for vertical polarization. For low incidence angles, both the foamed and unfoamed panels caused a reduction of about 0.35 dB in the transmitted signal; however, as the incidence angle increased, the unfoamed panel produced a rapid signal loss, reaching a loss of 1.25 dB for the 8 GHz signal at 60 degrees angle of incidence. This signal loss was not apparent for the foamed panel. This panel showed almost uniform transmission across the 0 to 60 degree angle of incidence range.

In general, very little amplitude changes were noted with the Astrocoat layer. The improvement of the transmission characteristics with the foam added was probably due to better impedance matching of the pyramidal plate.

The phase data indicated that an additional phase delay of about 10 degrees can be expected when the 0.020-inch thick Astrocoat is placed on the outer surface of the pyramidal grooved panel. A look at horizontal and vertical polarization phase delays shows that they were essentially equal for all angles of incidence of interest.

c. Pyramidal Plate After Foaming

The outer surface of the pyramidal grooved plate was covered with a low density PE-3 Isofoam manufactured by Isocyanate Products, Inc. The foam was used only for experimental purposes and it is not recommended for use on an operating antenna window or radome. The foam's purpose was to provide a smooth aerodynamic shape to the pyramidal grooved panel.

A comparison of the transmission data of the unfoamed panel with the foamed panel (one side only) showed an average reduction in transmission amplitude of about 0.2 dB; the difference between the two is greater at angles near 60 degrees and is most likely due to the edge effects.

The vertically polarized wave transmission was slightly more attenuated by the foam panel than was the horizontally polarized wave. On the average, only about 0.15 dB separated the two sets of data.

A much more noticeable effect was seen in the phase data. Generally, the foamed panel's insertion phase delay was about 18 degrees larger at zero degrees incidence and increased to a value of 29 degrees for angles close to 60 degrees. These values were found to apply to both polarizations. Both polarizations exhibited very nearly the same phase change characteristics, with the horizontally polarized waves being delayed by about 15 degrees more at large off-axis angles. Typical data are plotted in Figures 13, 14 and 15 for the pyramidal panel with and without the foam coating, foam and Mylar, and the rain erosion coating. The insertion phase shift versus incidence angle showed a smooth increase.

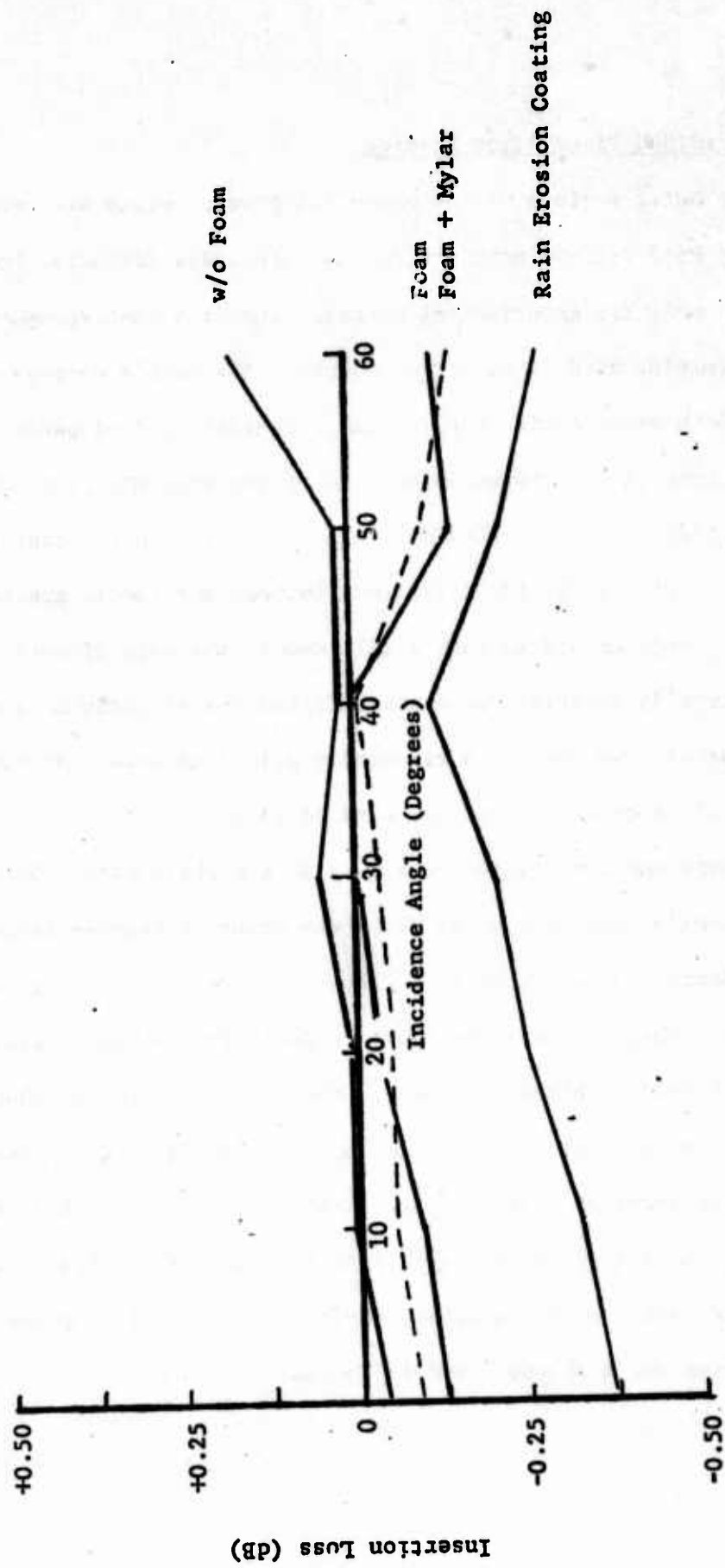


Figure 13. Insertion Loss of Pyramidal Grooved Flat Panel With and Without
Foam, Foam + Mylar, 0.020-inch Rain Erosion Coating,
Horizontal Polarization, $f = 11.0$ GHz.

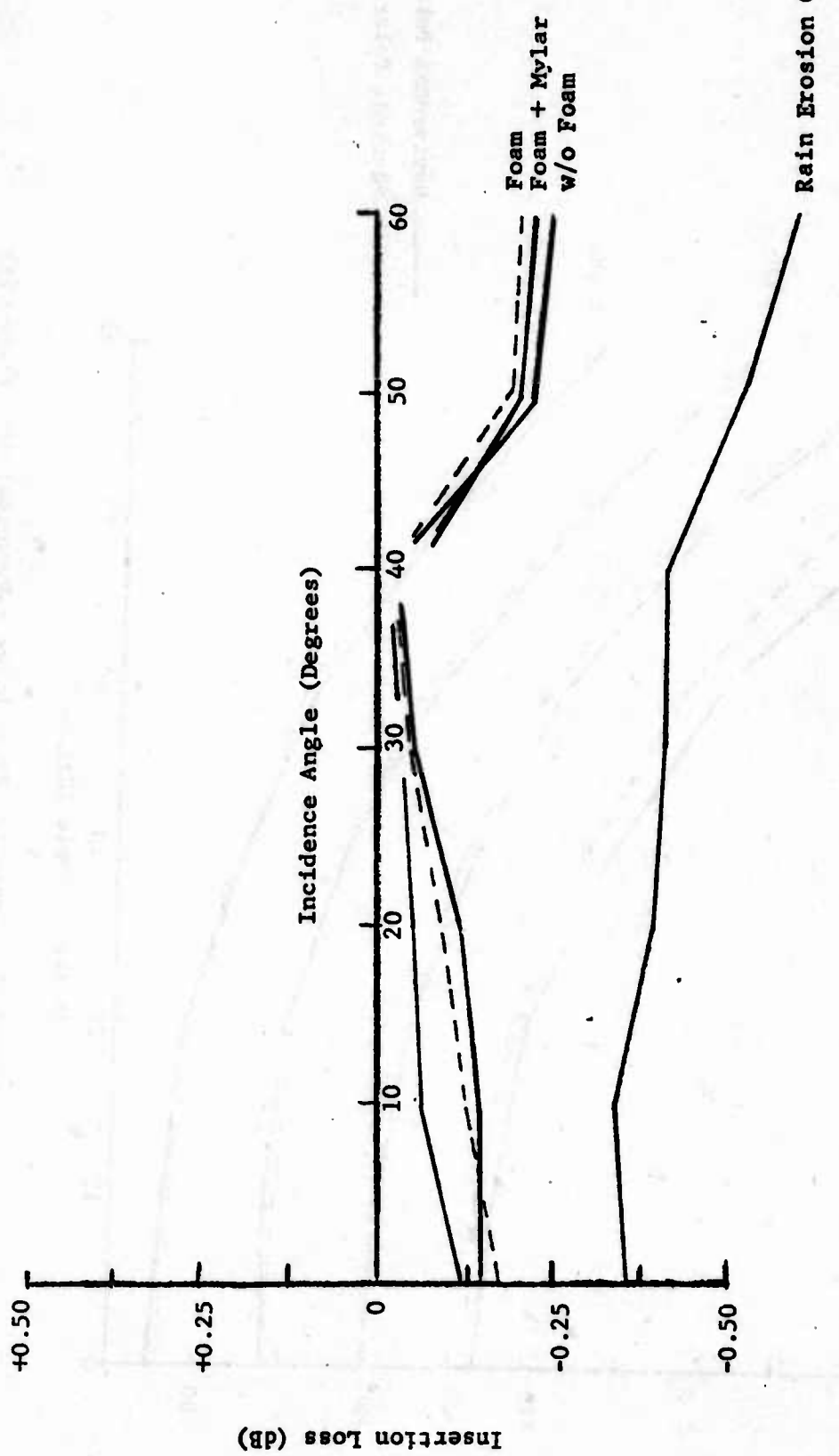


Figure 14. Insertion Loss of Pyramidal Grooved Flat Panel With and Without Foam, Foam + Mylar, 0.020-inch Rain Erosion Coating, Vertical Polarization, $f = 11.0$ GHz.

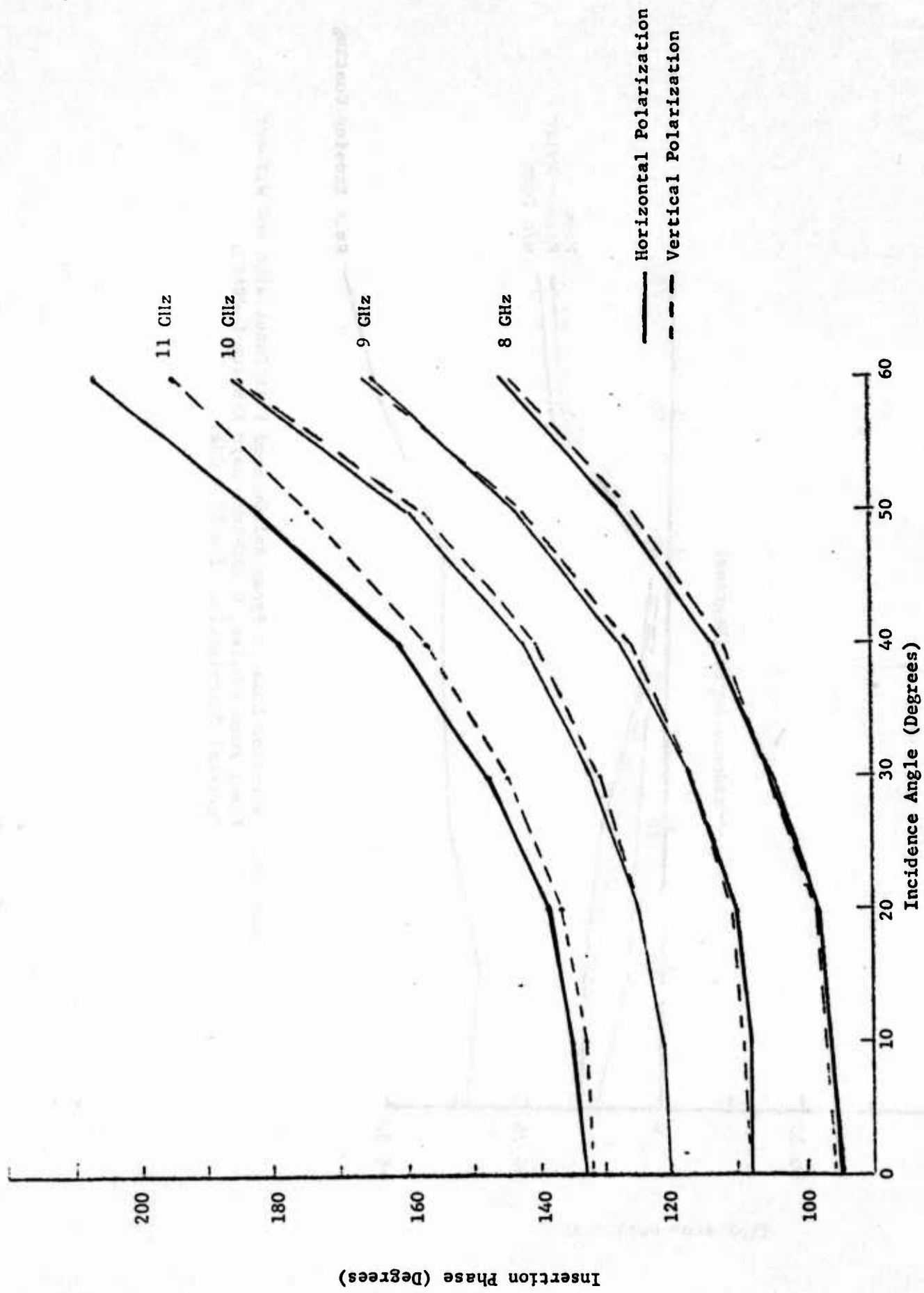


Figure 15. Insertion Phase Delay - Pyramidal Flat Plate With 0.020-inch Rain Erosion Coating.

3. Curved Panel Measured Results

a. Transmission Data

The transmission data for the cylindrically shaped grooved panel are presented in Appendix B. The significant results are (1) the panel has excellent broadband transmission characteristics, and (2) there is a lens effect that causes the transmission amplitude to increase over that of free space conditions.

b. Pyramidal Horn Radiation Patterns

The radiation patterns of a pyramidal horn antenna were measured with and without the cylindrical grooved panel. It was found that the amplitude characteristics of the horn with/without the curved panel are very similar. The phase characteristics are about the same to incidence angles up to $\pm 45^\circ$. A number of these patterns are included in Appendix B.

c. Air Force Array Antenna Radiation Patterns

The grooved cylindrical panel was used as an antenna window for an Air Force furnished array antenna. Radiation pattern measurements were performed on the mid-band array which had equal length phasing cables to the array elements. Typical radiation patterns are presented in Figures 16 through 27. At each measurement frequency (8 GHz, 9 GHz, 10 GHz, and 11 GHz) three radiation patterns were run; the first pattern is of the antenna array without the cylindrical broadband panel, the second is of the Mid-Band Array mounted flush against the cylindrical broadband panel, and the third is of the array mounted at the center of curvature of the cylindrical broadband panel. As noted in the radiation pattern plots, the panel had

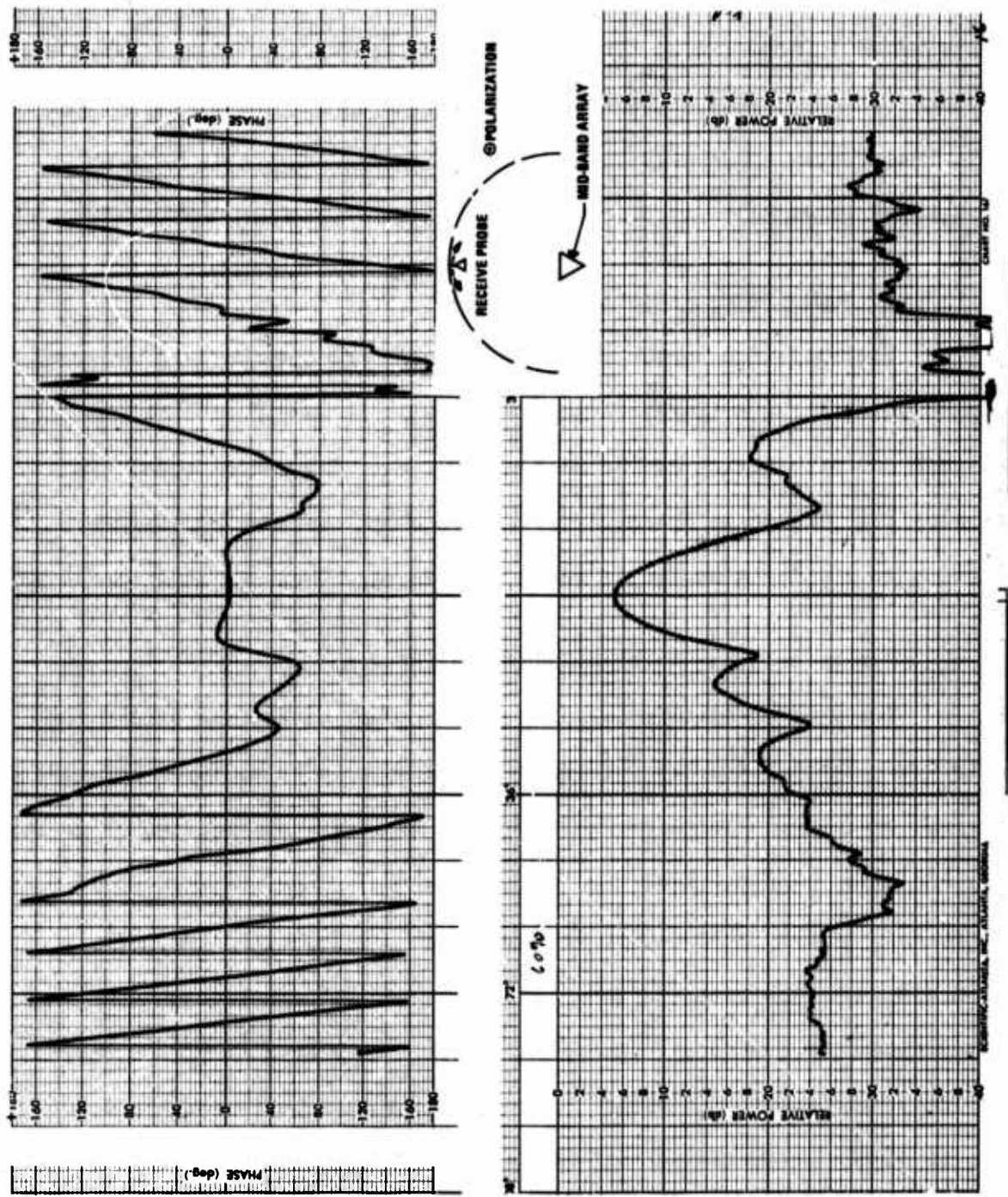


Figure 16. Radiation Pattern of Mid-Band Array, $f = 8$ GHz.

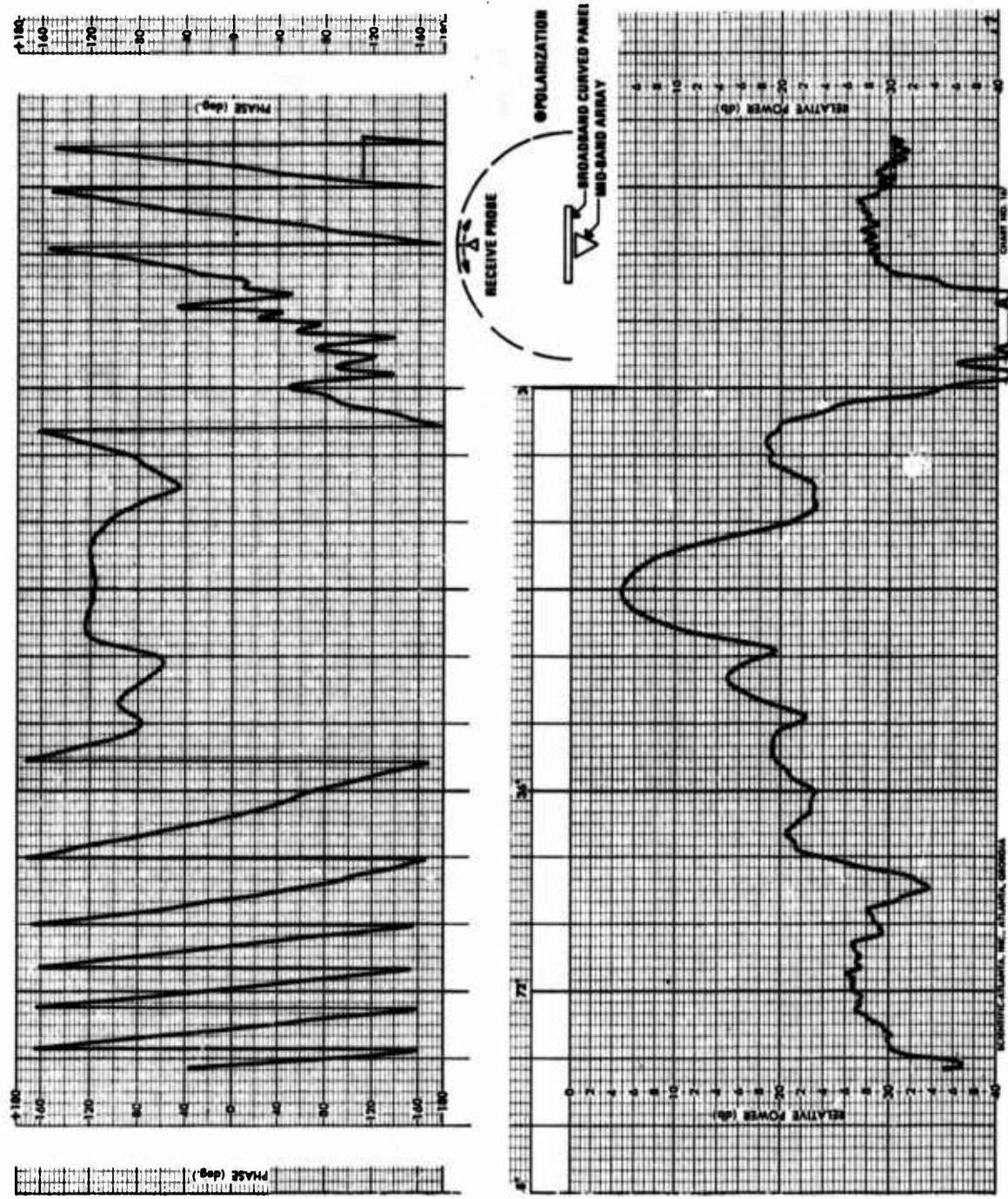


Figure 17. Radiation Pattern of Mid-Band Array Mounted Flush with Inner Surface of Broadband Cylindrical Panel, $f = 8$ GHz.

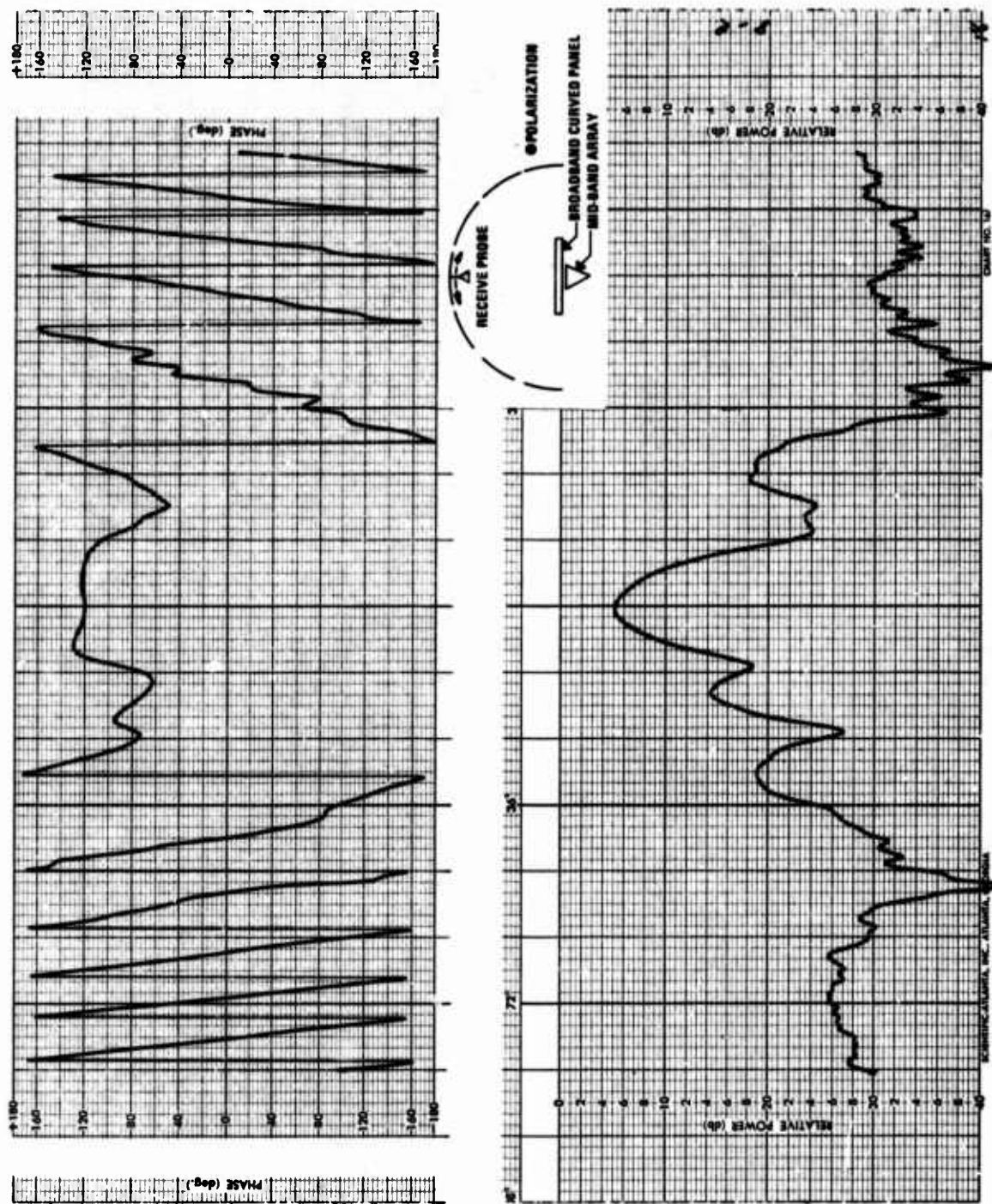


Figure 18. Radiation Pattern of Mid-Band Array Mounted Toward Rear of Broadband Cylindrical Panel, $f = 9$ GHz.

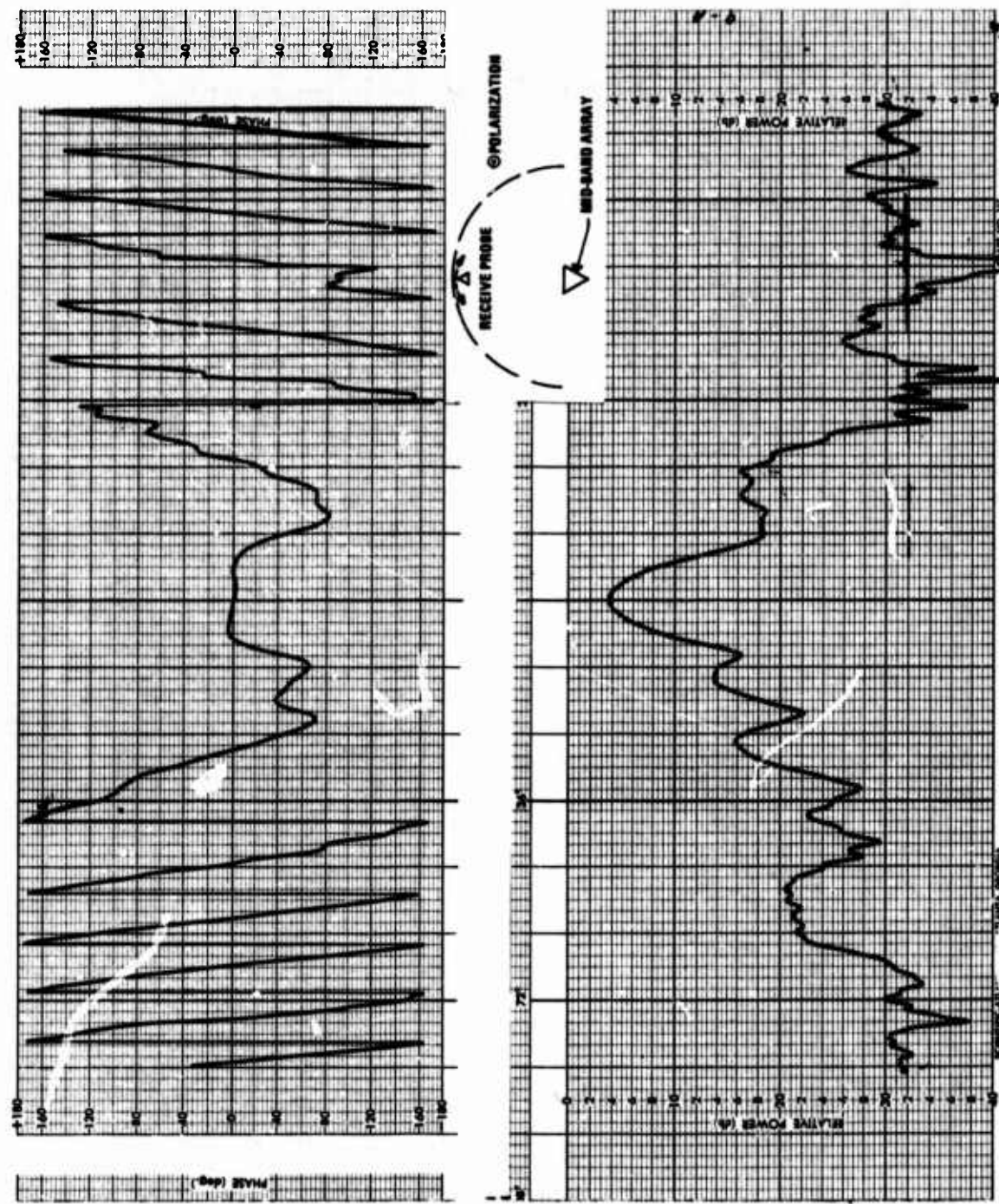


Figure 19. Radiation Pattern of Mid-Band Array, $f = 9$ GHz.

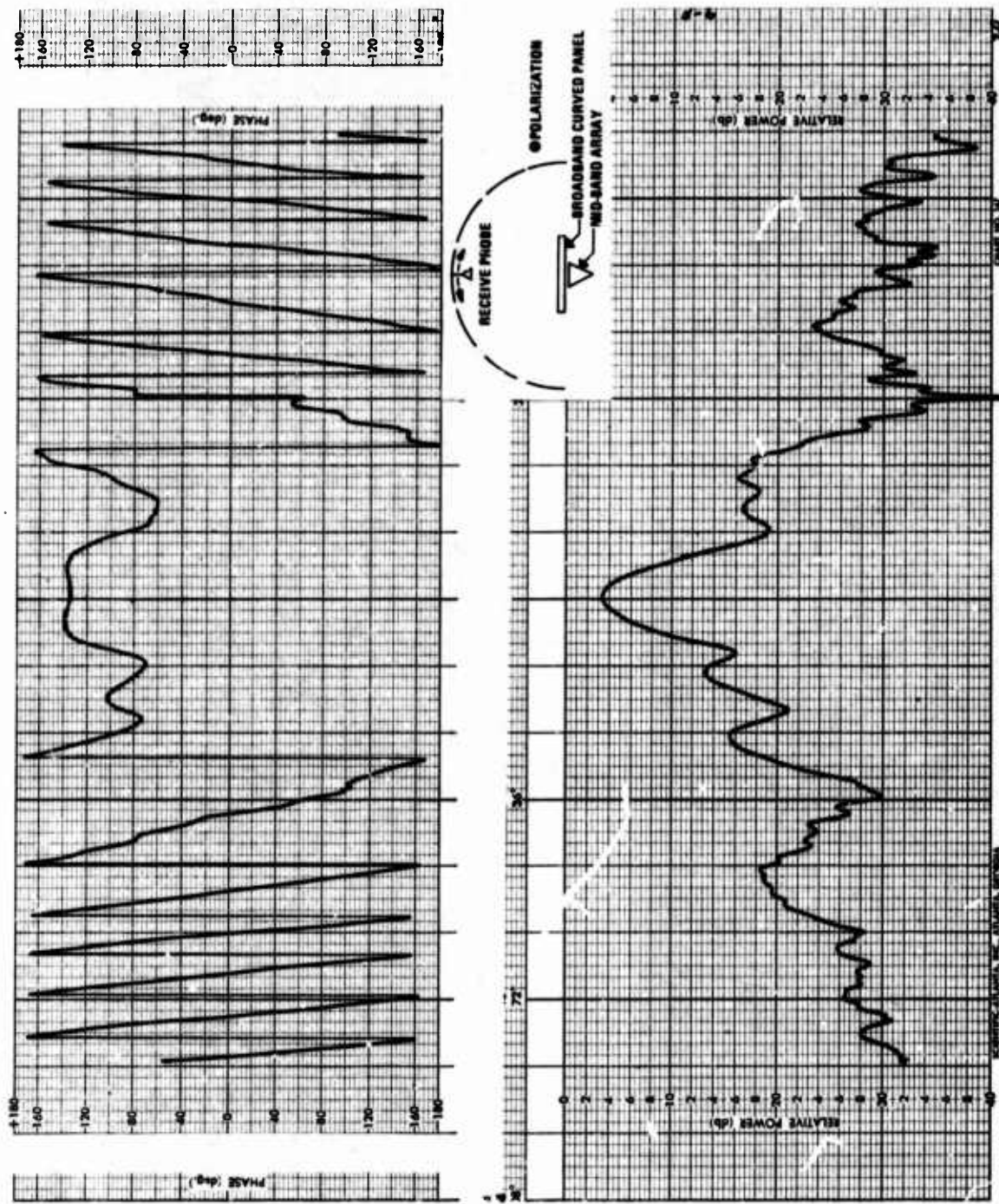


Figure 20. Radiation Pattern of Mid-Band Array Mounted Flush with Inner Surface of Broadband Cylindrical Panel, $f = 9$ GHz.

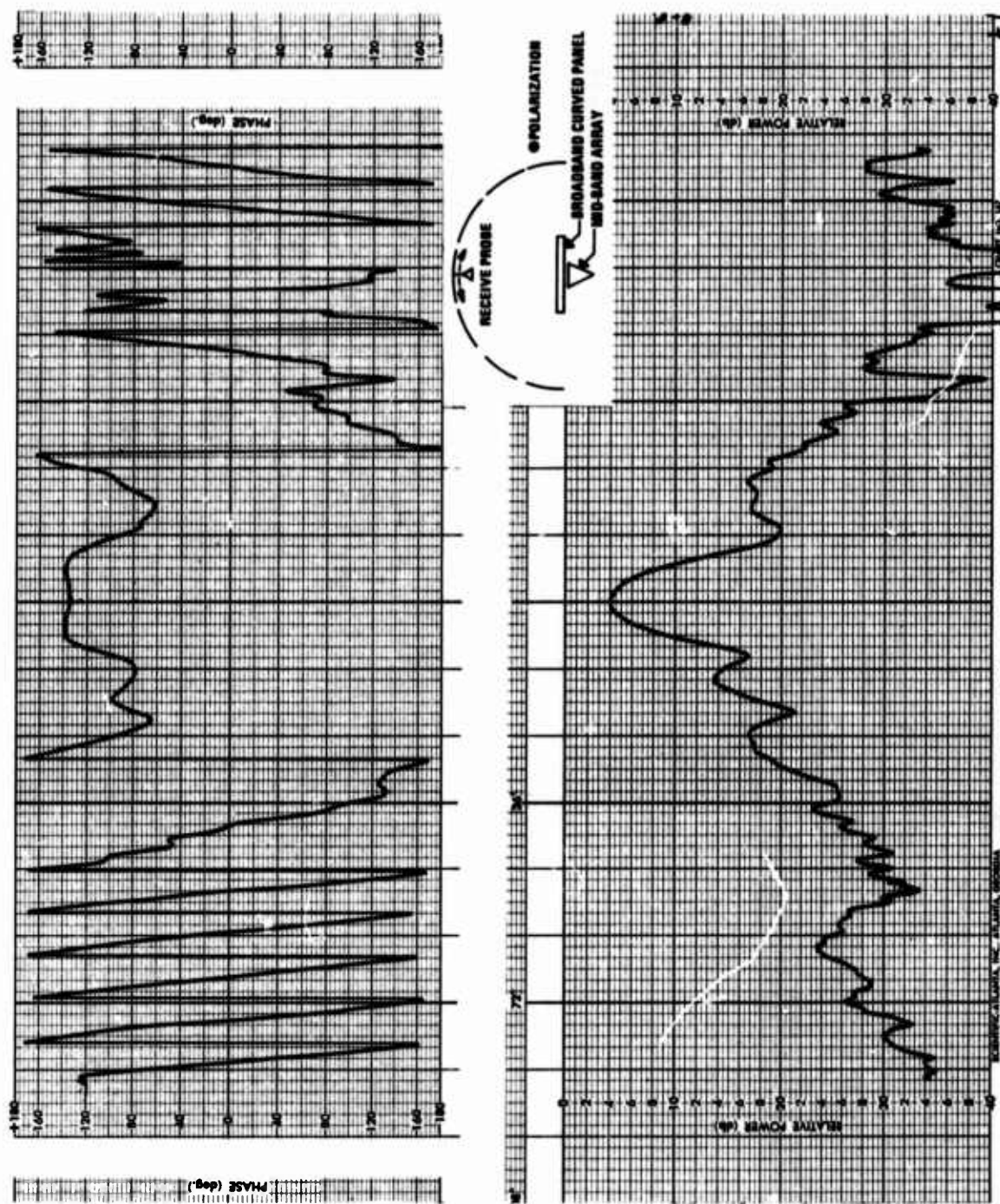


Figure 21. Radiation Patterns of Mid-Band Array Mounted Toward Rear of Broadband Cylindrical Panel, $f = 9$ GHz.

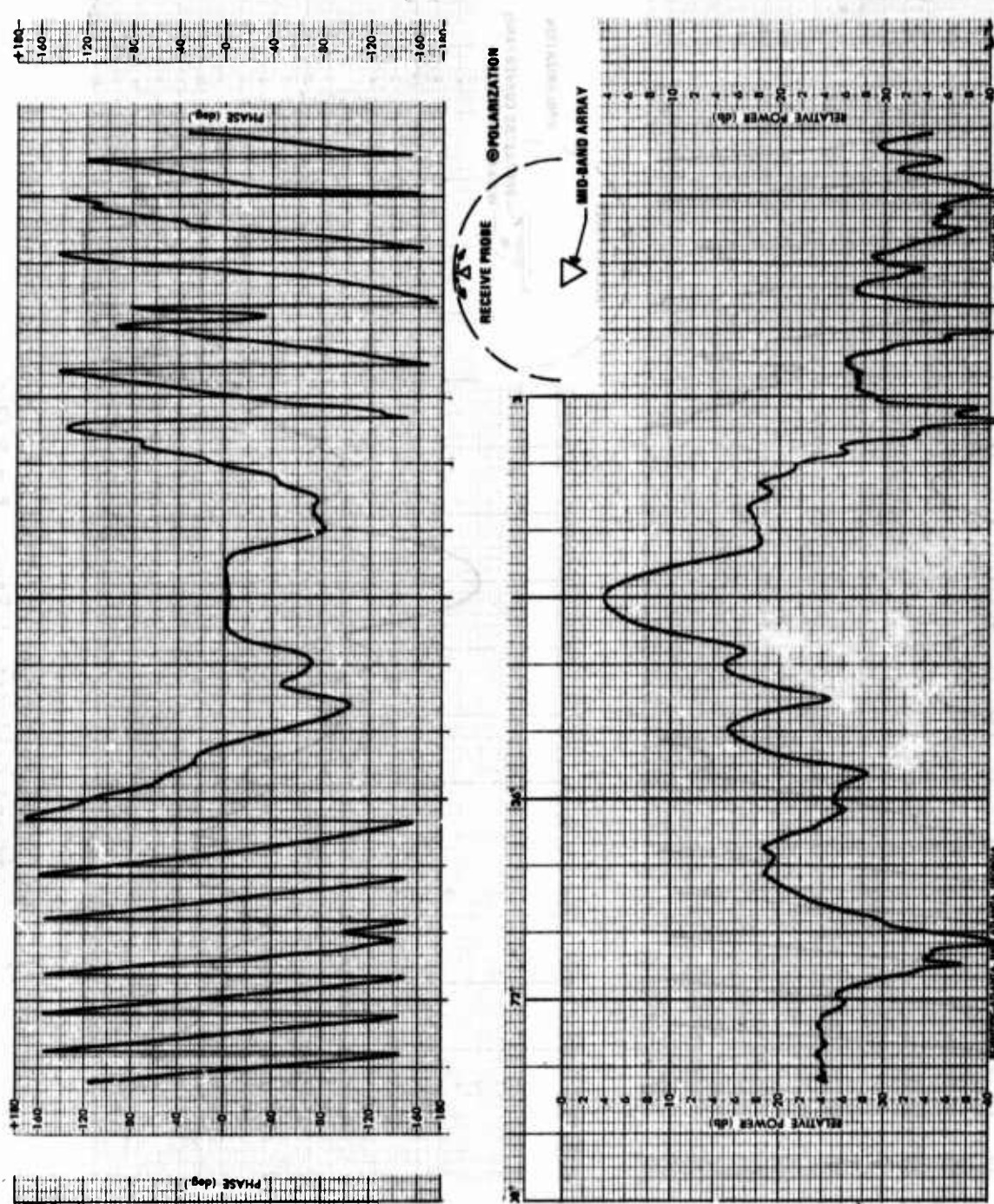


Figure 22. Radiation Pattern of Mid-Band Array, $f = 10$ GHz.

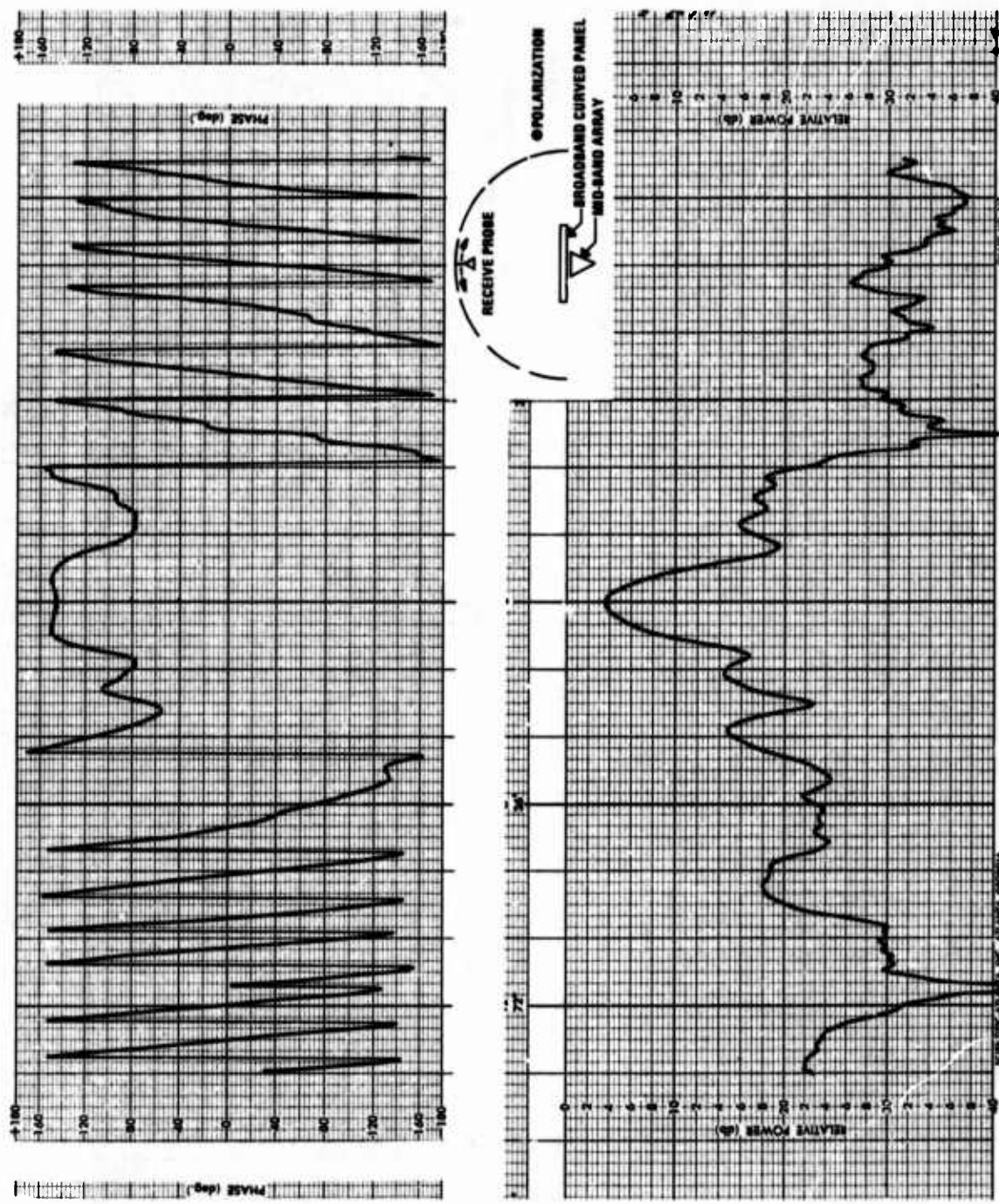


Figure 23. Radiation of Mid-Band Array Mounted Flush with Inner Surface of Broadband Cylindrical Panel, $f = 10$ GHz.

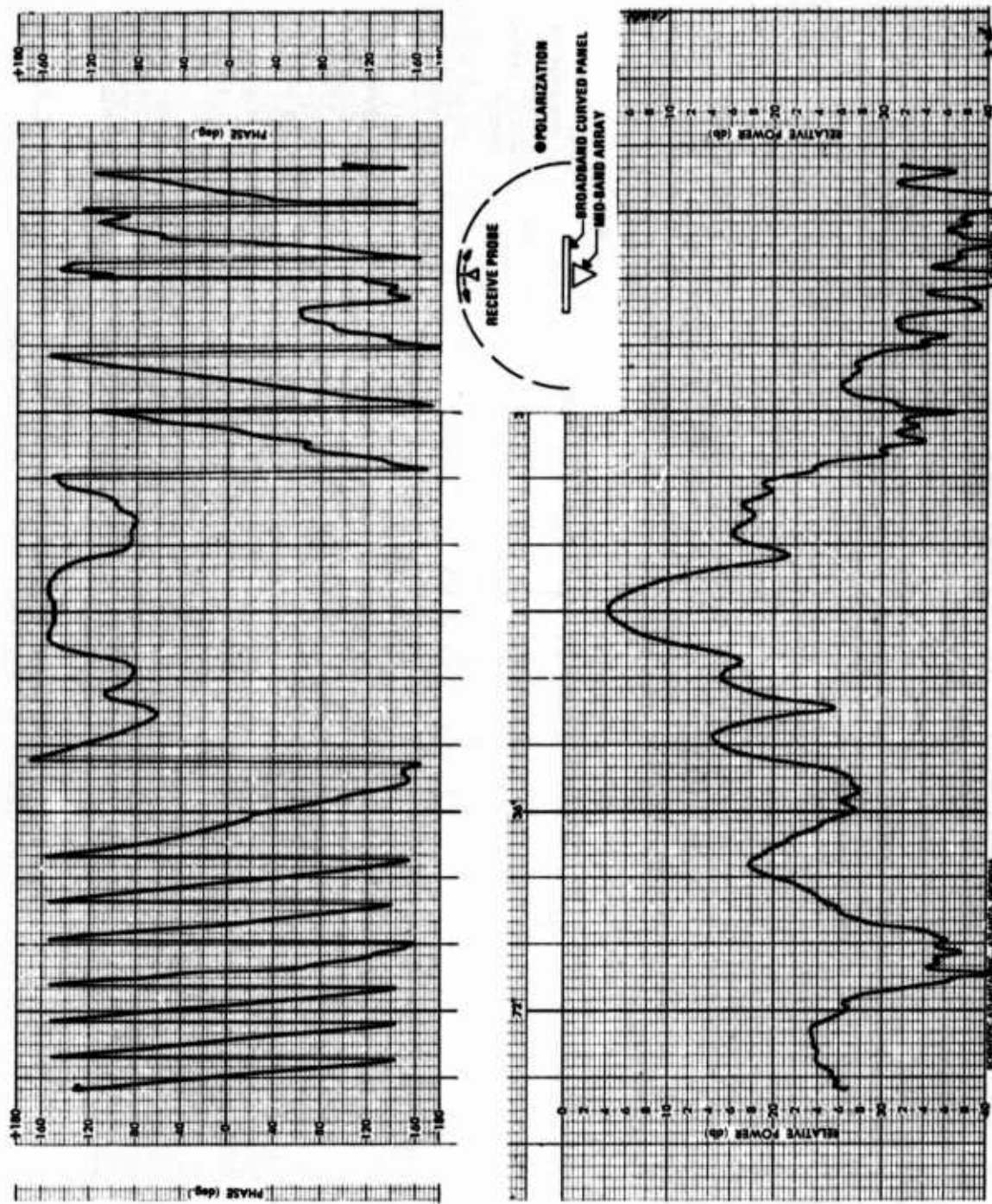


Figure 24. Radiation Pattern of Mid-Band Array Mounted Toward Rear of Broadband Cylindrical Panel, $f = 10$ GHz.

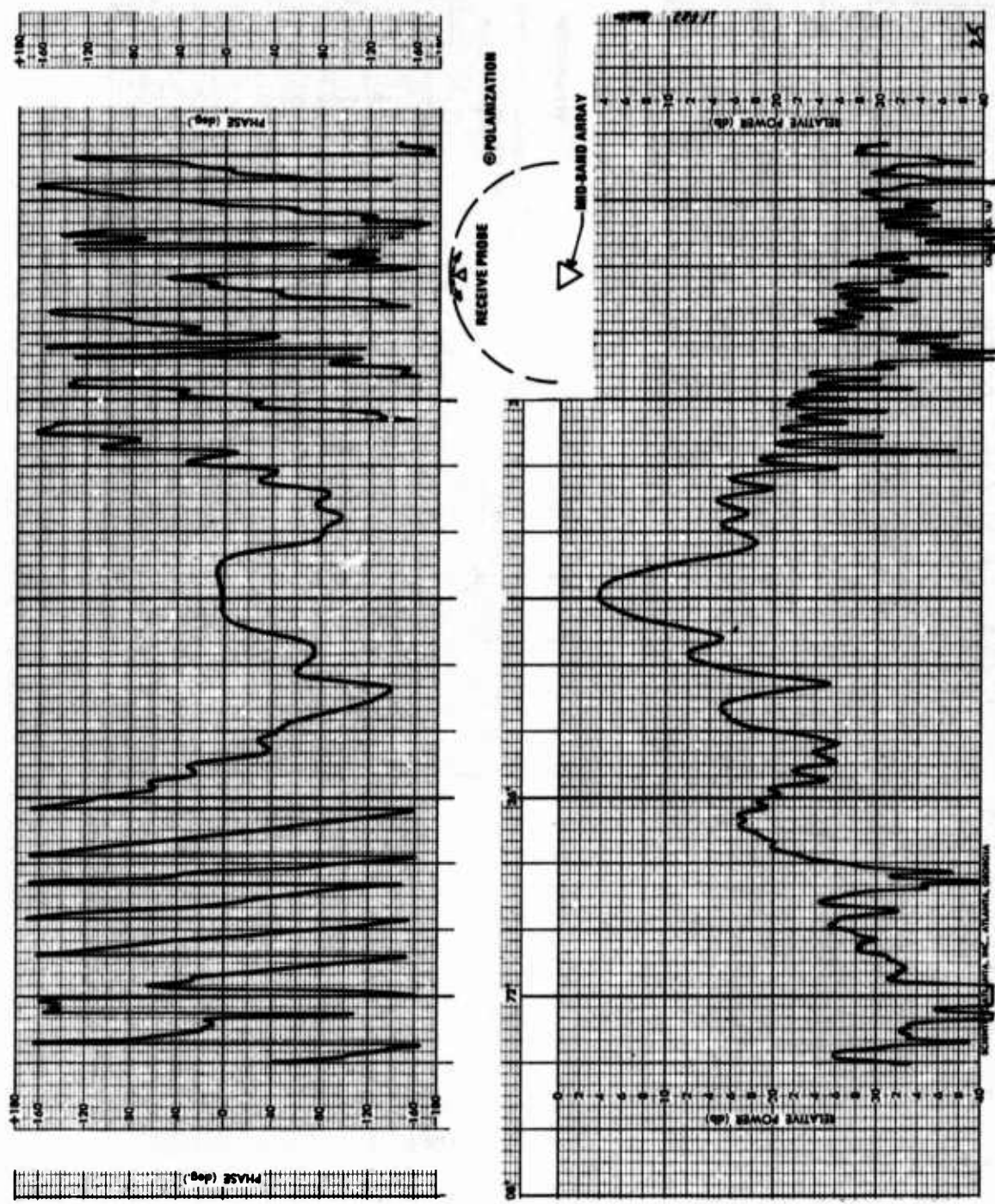


Figure 25. Radiation Pattern of Mid-Band Array, $f = 11$ GHz.

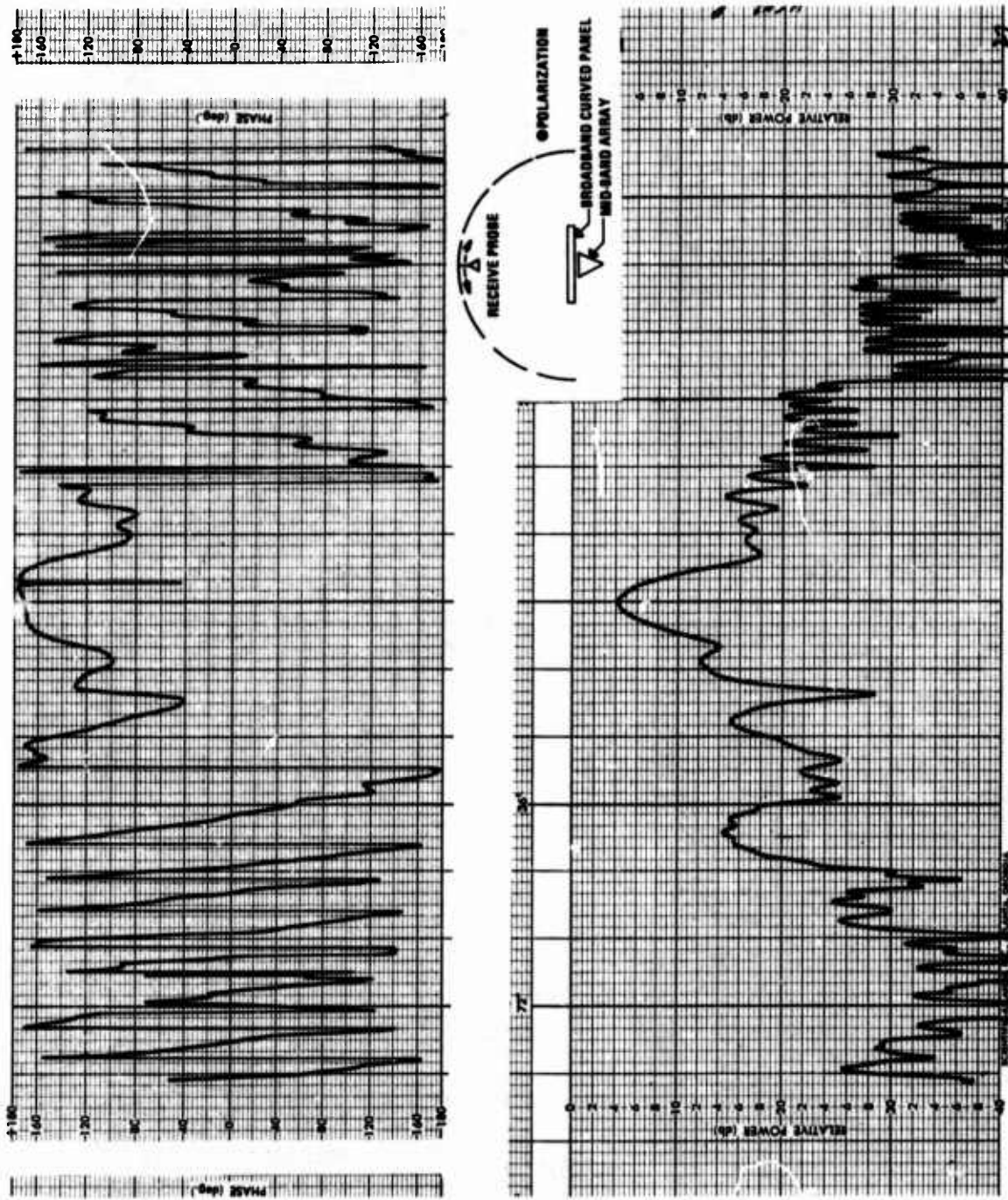


Figure 26. Radiation Pattern of Mid-Band Array Mounted Flush with Inner Surface of Broadband Cylindrical Panel, $f = 11$ GHz.

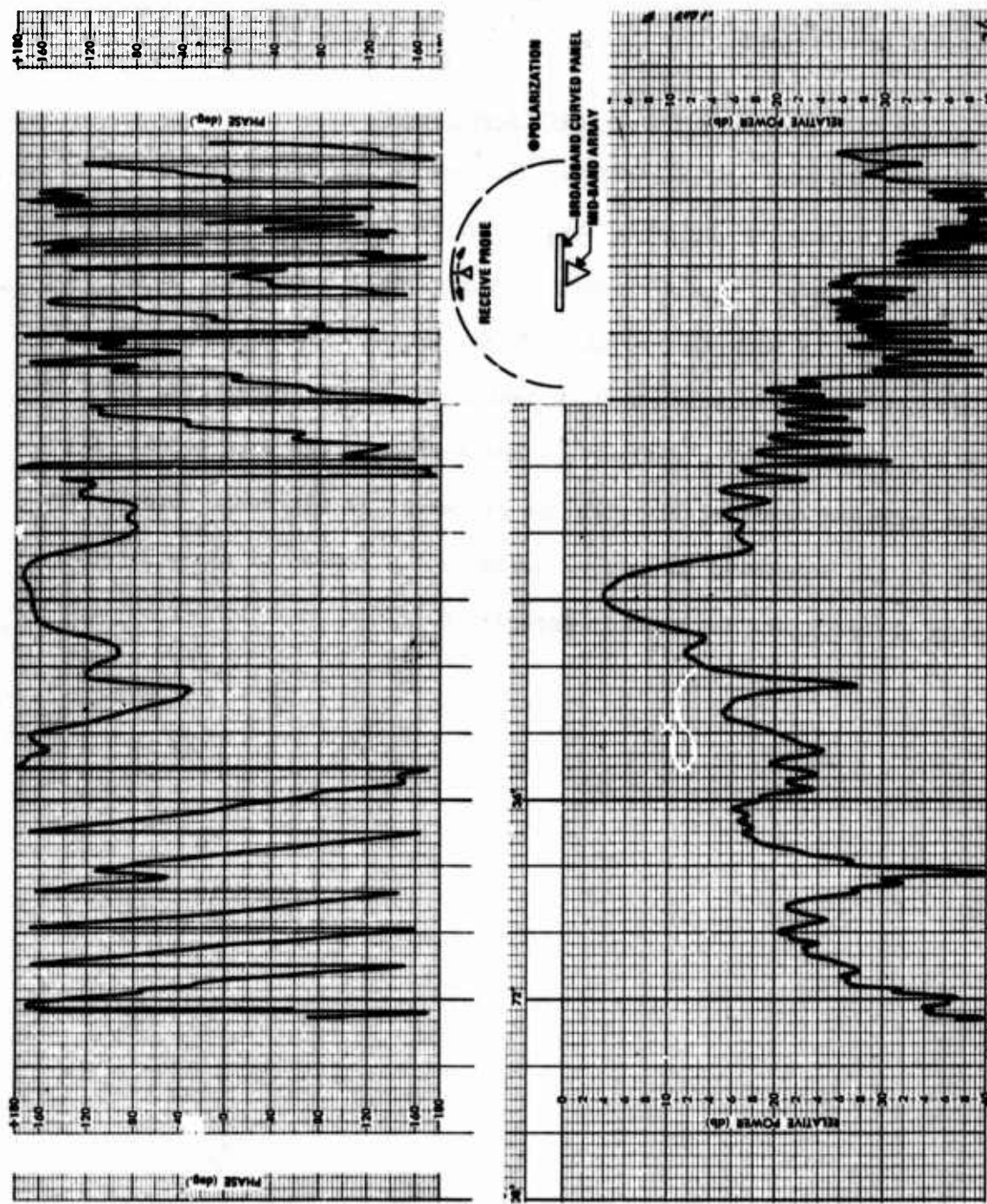


Figure 27. Radiation Pattern of Mid-Band Array Mounted Toward Rear of Broadband Cylindrical Panel, $f = 11$ GHz.

very little effect on the radiation pattern main lobe and the initial side-lobes. This was typical of the broadband panel as noted on numerous radiation pattern measurement plots.

d. Curved Panel with Fiberglass Outer Shell

A 0.063-inch thickness fiberglass shell was fabricated to simulate a protective coating on the outer surface of the broadband cylindrical panels. Radiation patterns were made of a pyramidal horn with the curved panel positioned in both the vertical and horizontal planes. The horn was positioned approximately one inch behind the curved structure, and pattern distortions due to reflections and surface waves were noted. The patterns improved considerably with the placement of microwave absorber on the rear of the broadband panel flat surfaces. A number of these X-band radiation patterns are included in Appendix B.

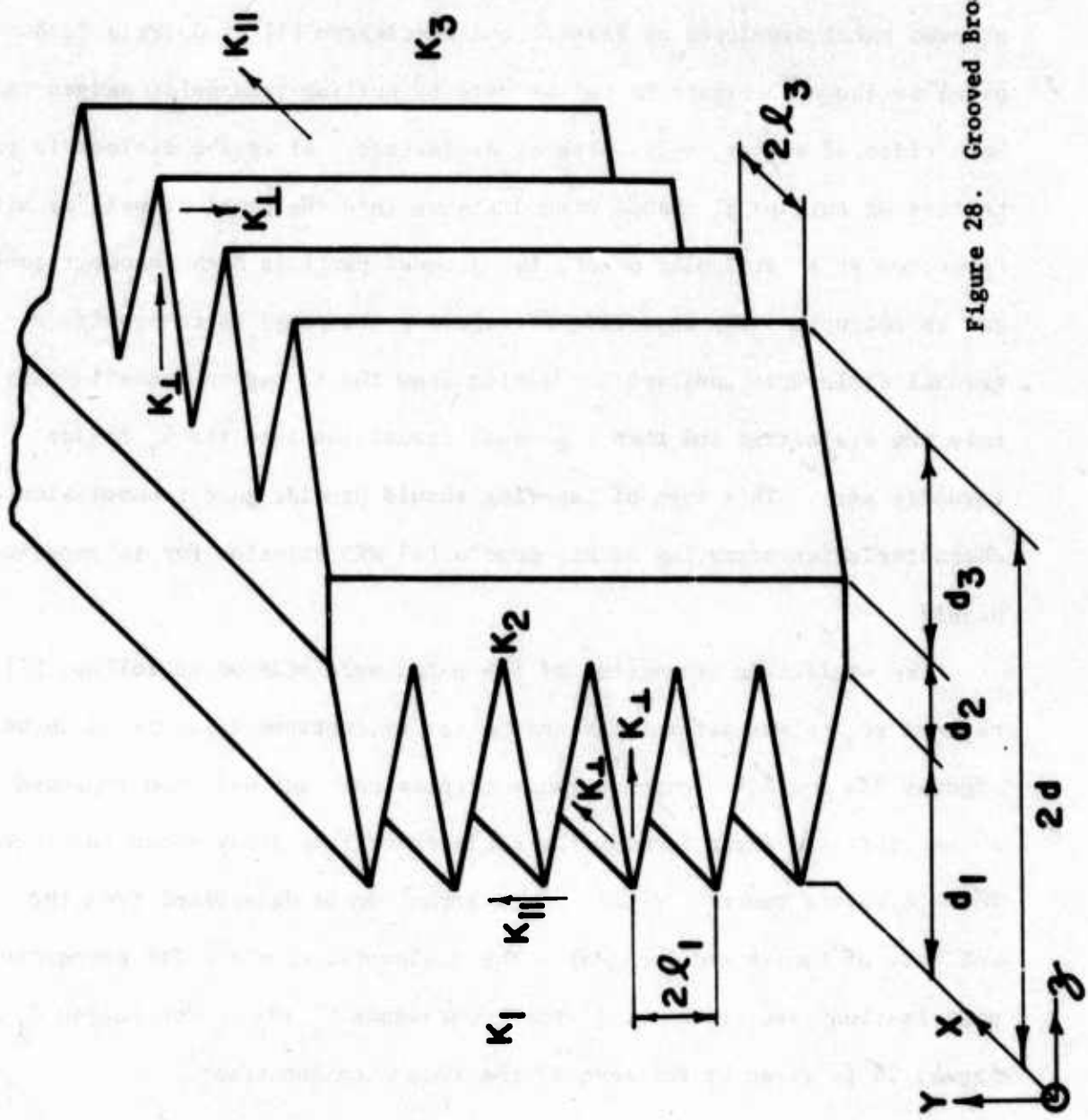
SECTION V

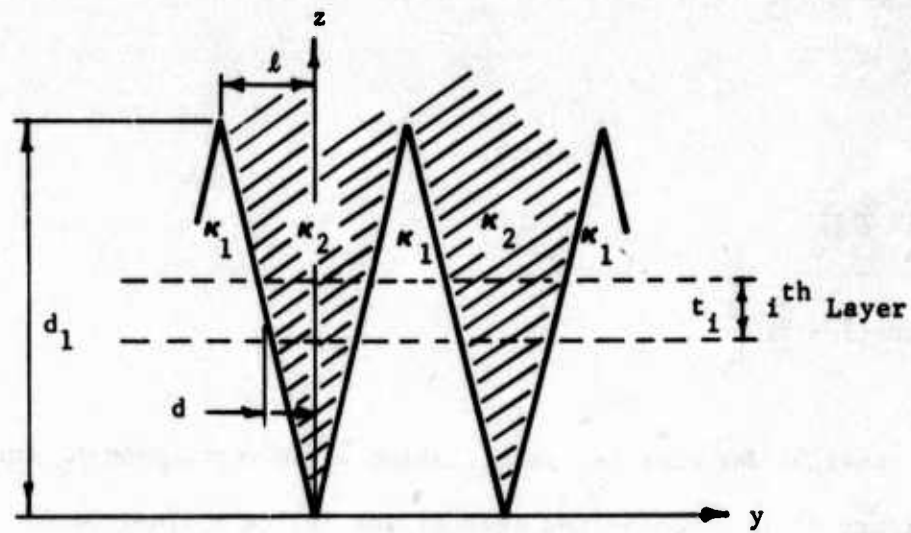
COMPARISON OF PREDICTED DATA TO MEASURED DATA

The analysis of Section II was performed in order to model a particular grooved panel developed by Bassett and Huddleston [1] at Georgia Tech. This panel is shown in Figure 28 and is made by cutting triangular wedges into both sides of a flat, solid slab of dielectric. Since the dielectric properties of this panel change with distance into the panel as well as with direction at a particular point, the grooved panel is both inhomogeneous and anisotropic. The objective of tapering the panel is to provide a gradual dielectric constant transition from the κ_1 region (usually air) into the dielectric and then a gradual transition into the κ_3 region (usually air). This type of tapering should provide good transmission characteristics according to Richmond's [4] WKB solution for inhomogeneous panels.

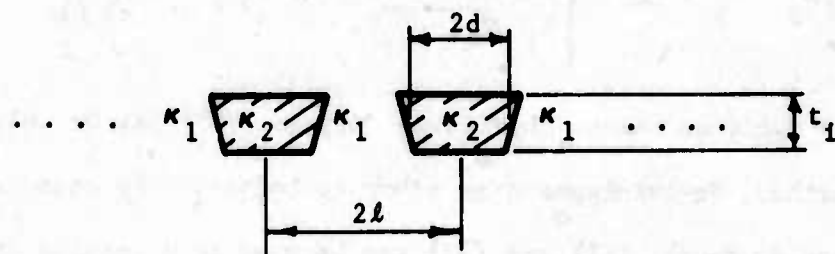
The dielectric properties of the panel were modeled as follows [1]. The tapered region was partitioned into a set of contiguous layers as shown in Figures 29a and 29b. Each of these trapezoidal rods was then replaced by a semi-infinite strip forming the dielectric strip array shown in Figure 6c. The dielectric tensor for this strip array can be determined from the analysis of Morita and Cohn [9]. The dielectric constant for perpendicular polarization (see Figure 29c) which represents κ_x and κ_z for region d_1 of Figure 28 is given by the zero of the following function:

$$f_1(\kappa_1) = -\frac{\pi}{2} + A \sqrt{\kappa_2 - \kappa_1} + \tan^{-1} \left[\sqrt{\frac{\kappa_2 - \kappa_1}{\kappa_1 - \kappa_1}} \coth \left(B \sqrt{\kappa_1 - \kappa_1} \right) \right] \quad (62)$$

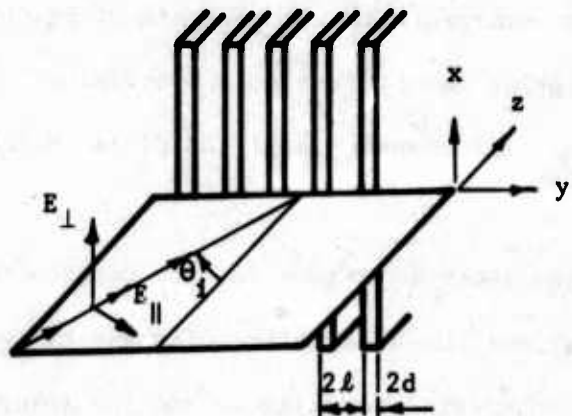




(a) Division of tapered region into discrete layers (top view)



(b) Representation of each layer as rectangular dielectric strips of finite thickness (top view)



(c) Appropriate case from analysis of dielectric strip array of semi-infinite depth (perspective view)

Figure 29. Steps in Determining Dielectric Constants of Layers in Grooved Dielectric Panel.

where

$$A = 2\pi \frac{d}{\lambda} \frac{\ell}{\lambda_0}$$

$$B = 2\pi \left(1 - \frac{d}{\lambda}\right) \frac{\ell}{\lambda_0} .$$

The dielectric constant for parallel polarization which represents κ_y for region d_1 of Figure 28 is given by the zero of the following function:

$$f_{\parallel}(\kappa_{\parallel}) = A \sqrt{\kappa_2 - \kappa_{\parallel}} - \tan^{-1} \left[\frac{\kappa_2 \sqrt{\kappa_{\parallel} - \kappa_1}}{\kappa_1 \sqrt{\kappa_2 - \kappa_{\parallel}}} \tanh \left(B \sqrt{\kappa_{\parallel} - \kappa_1} \right) \right] \quad (63)$$

and A and B are defined as above. Equations (61) and (62) can be solved using Muller's method, Newton-Raphson or other techniques. By using an appropriate change in terms, (61) and (62) can be used to determine the κ 's of region d_3 of Figure 28.

The above dielectric tensor model was used to describe the panel shown in Figure 28. This model combined with the analysis of Section I permits the evaluation of transmission and reflection properties of the panel for both perpendicular and parallel components of the field incident on the panel.

Two panels of the type shown in Figure 28 were constructed and measured at Georgia Tech. The physical characteristics of these two panels are given in Table I. The transmission coefficient and the insertion phase delay of these two panels is presented in Figures 30 through 37. A comparison of measured and predicted values is given in Tables II and III. From Tables II and III it can be seen that the predicted and measured

TABLE I
PROPERTIES OF TWO TESTED PANELS

Parameter	Panel 1	Panel 2
κ_1	1.00	1.00
κ_2	2.54	2.54
κ_3	1.00	1.00
d_1 (inches)	0.625	0.625
d_2 (inches)	0.250	0.250
d_3 (inches)	0.625	0.625
$2\ell_1$ (inches)	0.250	0.125
$2\ell_3$ (inches)	0.250	0.125

transmission coefficients agree with ± 0.2 dB while the insertion phase delay agrees within $\pm 4^\circ$ over the measured 2 to 35 GHz range. This excellent agreement indicates that the analysis and dielectric model are good.

Some general comments can be made regarding the transmission characteristic shown in Figures 30 through 37. At very low frequencies, below 1 GHz, the panel begins to behave as a thin wall radome and the transmission coefficient for both polarization approaches $1/0^0$. At around 2 to 2.5 GHz the panel is roughly $\lambda_0/4$ thick. The tapers are not electrically long enough to permit a slow change in dielectric constant from free space to a value of 2.54 at the center as required by the WKB solution [6]. Hence, a substantial reflection occurs. As the frequency is increased, the tapers look longer electrically and low loss transmission is obtained with this thick wall structure as expected from the WKB solution.

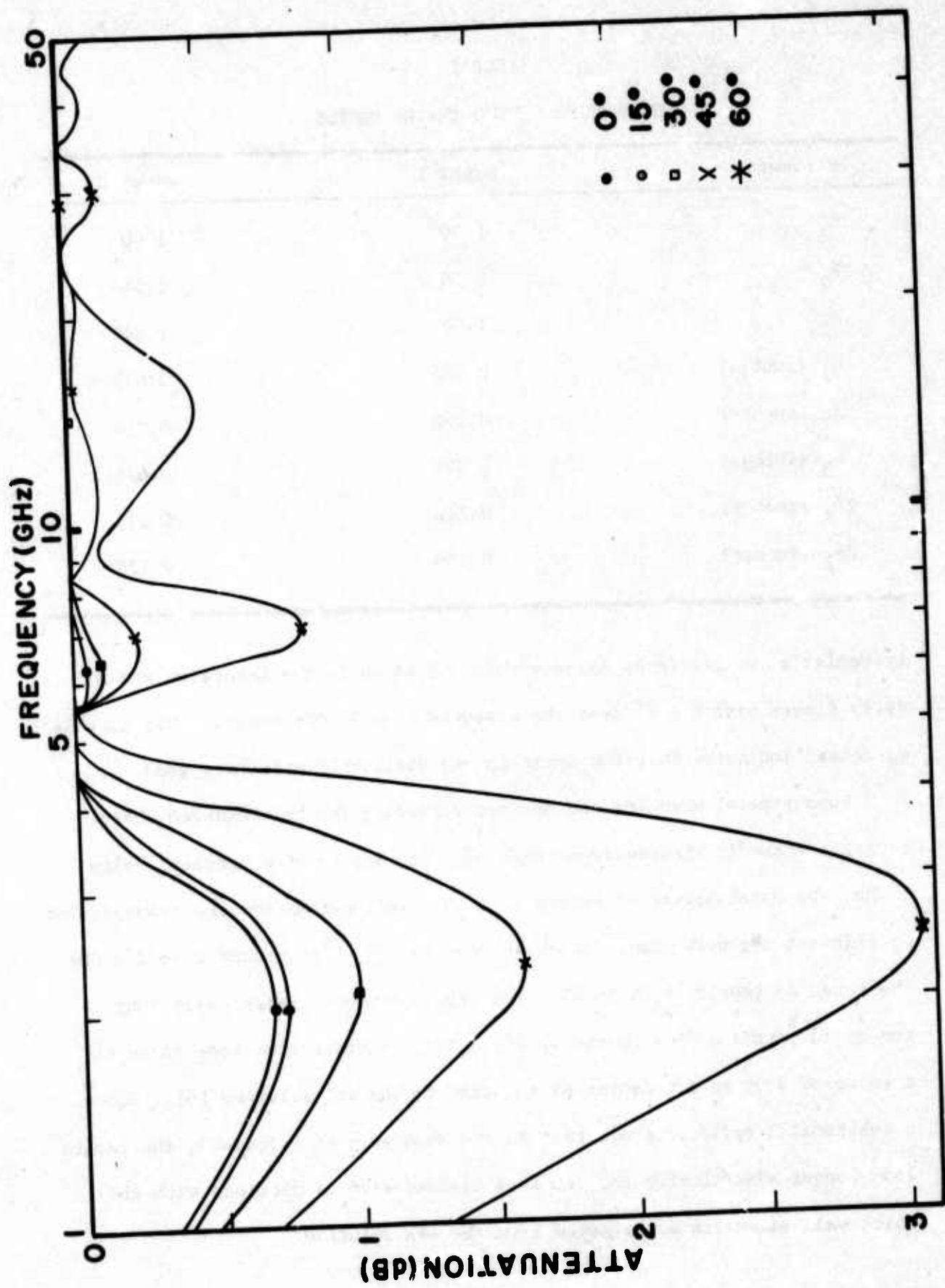


Figure 30. Transmission Loss of Perpendicular Polarized Component for Panel No. 1.

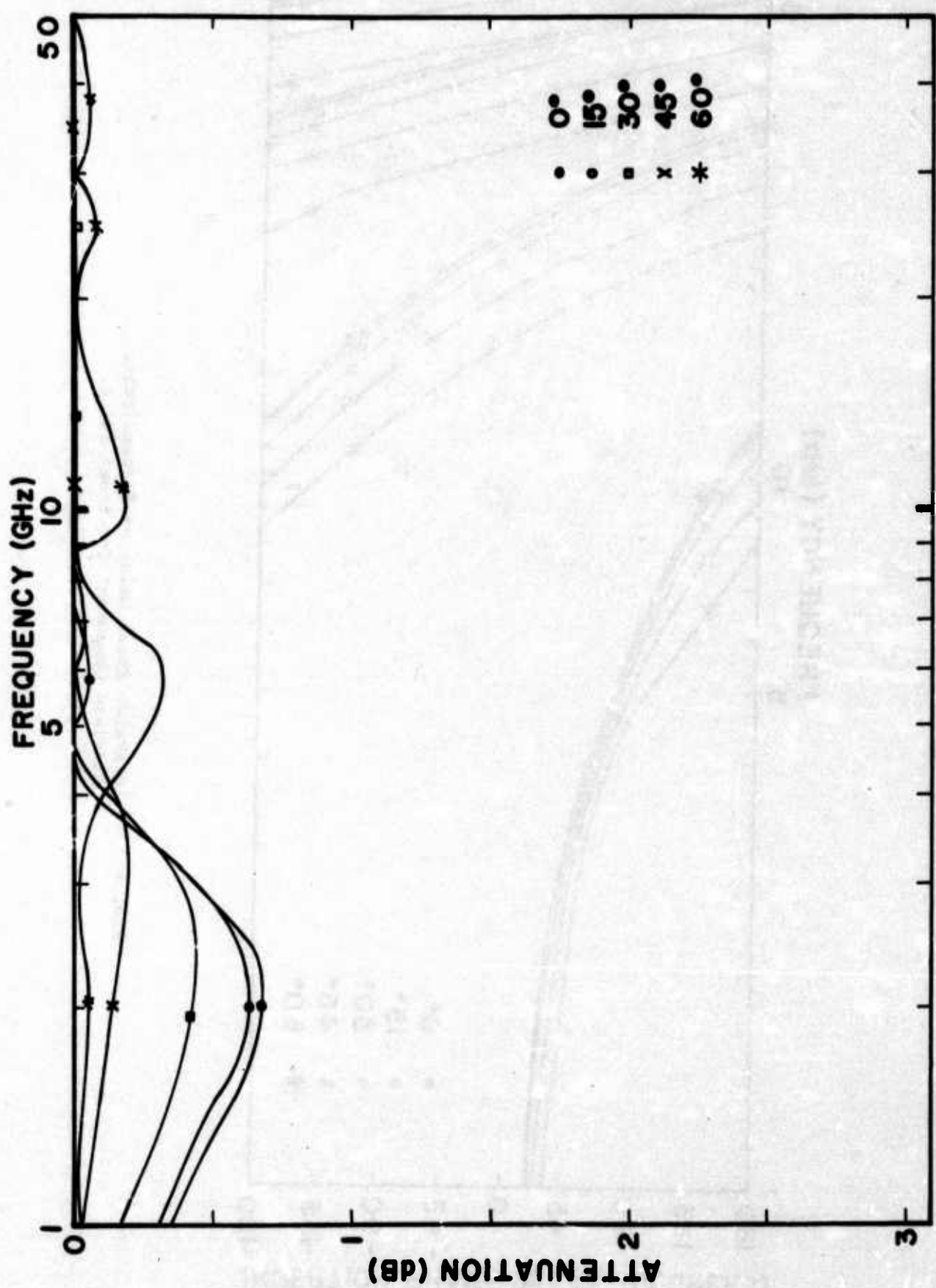


Figure 31. Transmission Loss of Parallel Polarized Component for Panel No. 1.

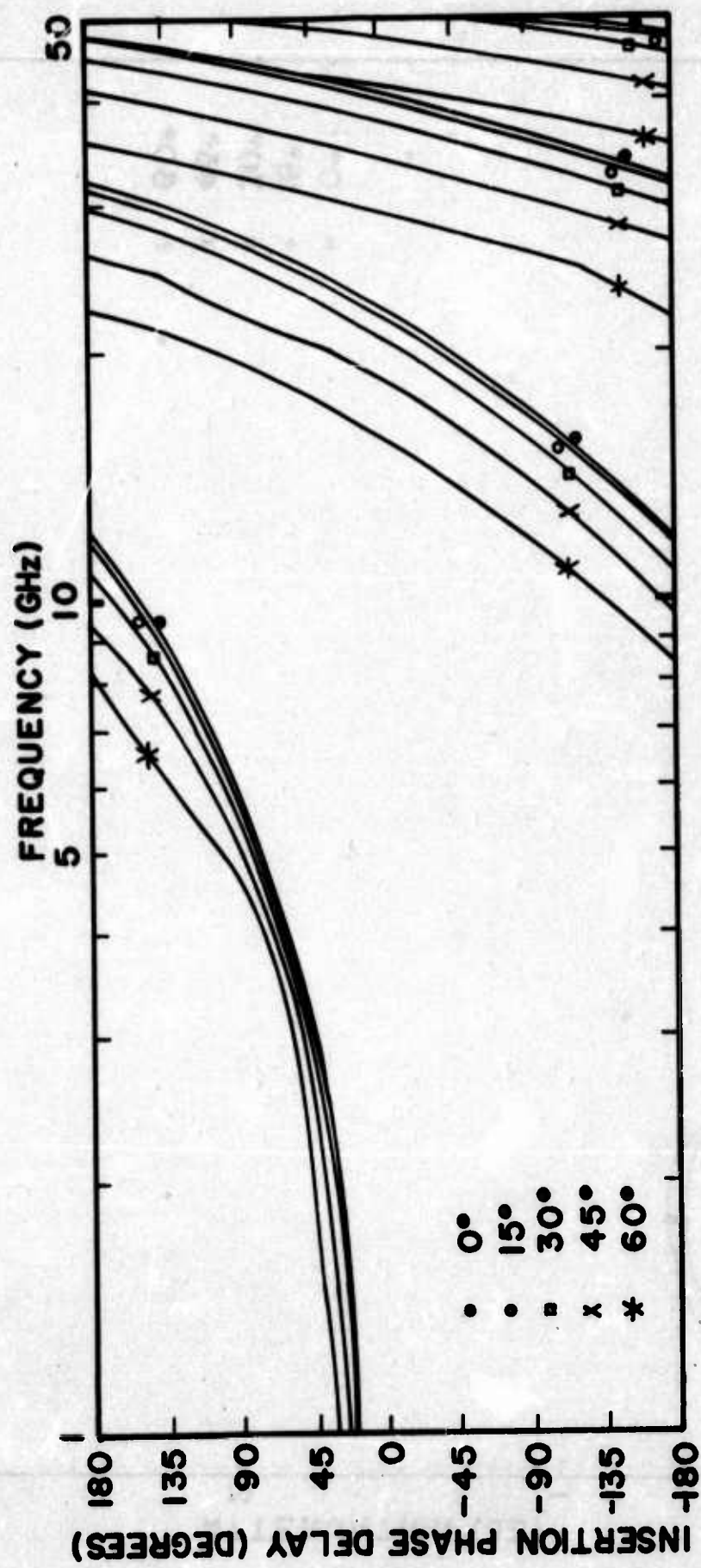


Figure 32. Insertion Phase Delay of Perpendicular Polarized Component for Panel No. 1.

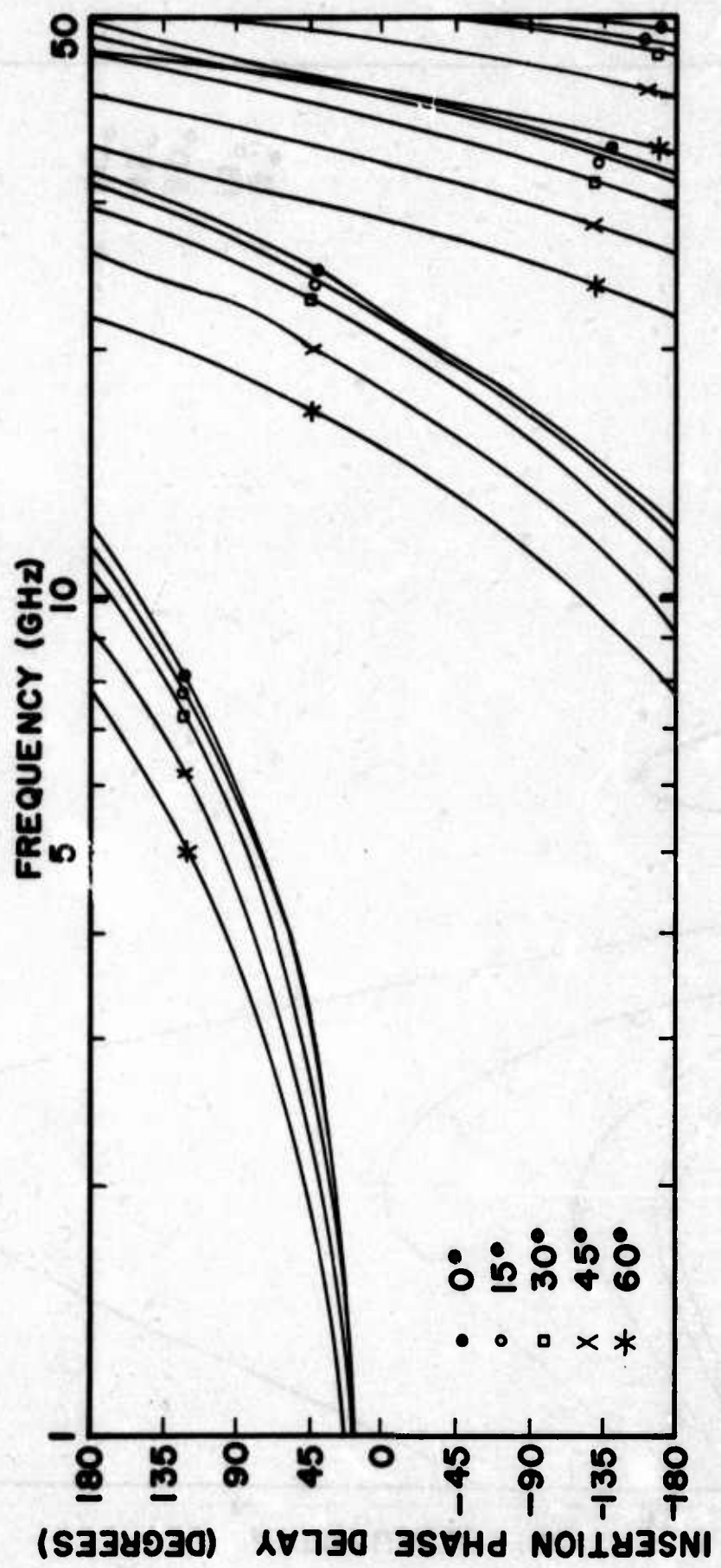


Figure 33. Insertion Phase Delay of Parallel Polarized Component for Panel No. 1.

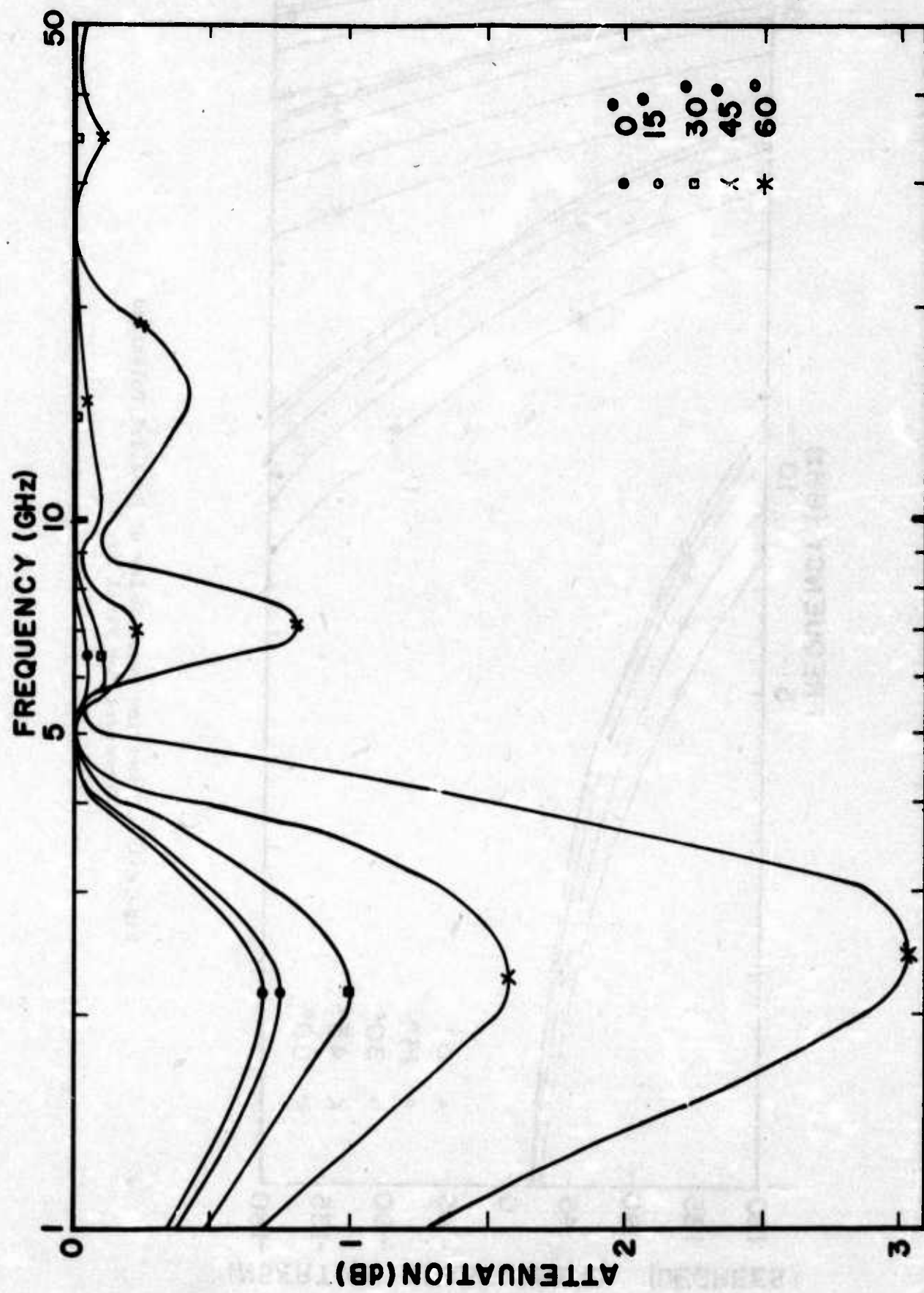


Figure 34. Transmission Loss of Perpendicular Polarized Component for Panel No. 2.

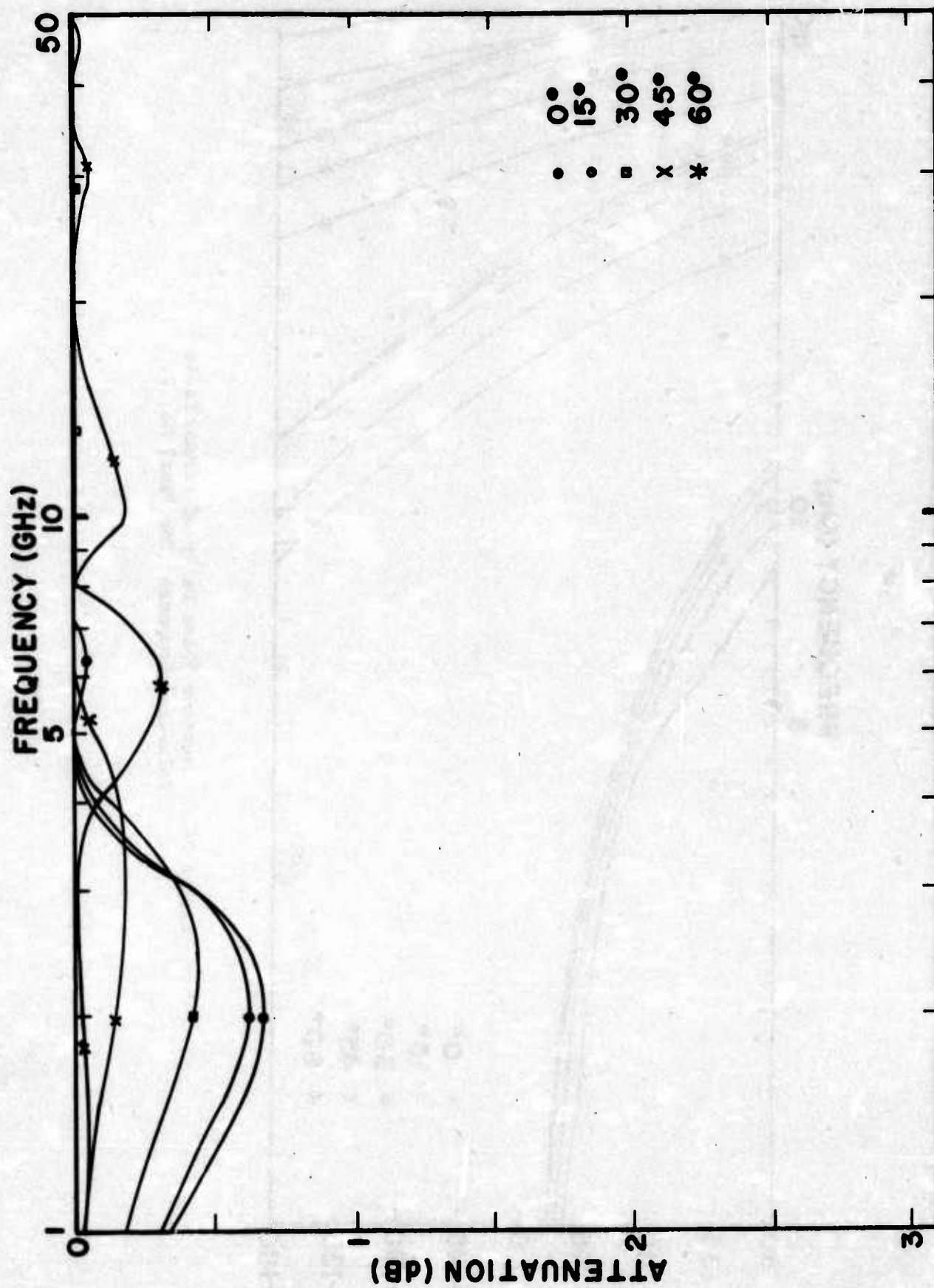


Figure 35. Transmission Loss of Parallel Polarized Component for Panel No. 2.

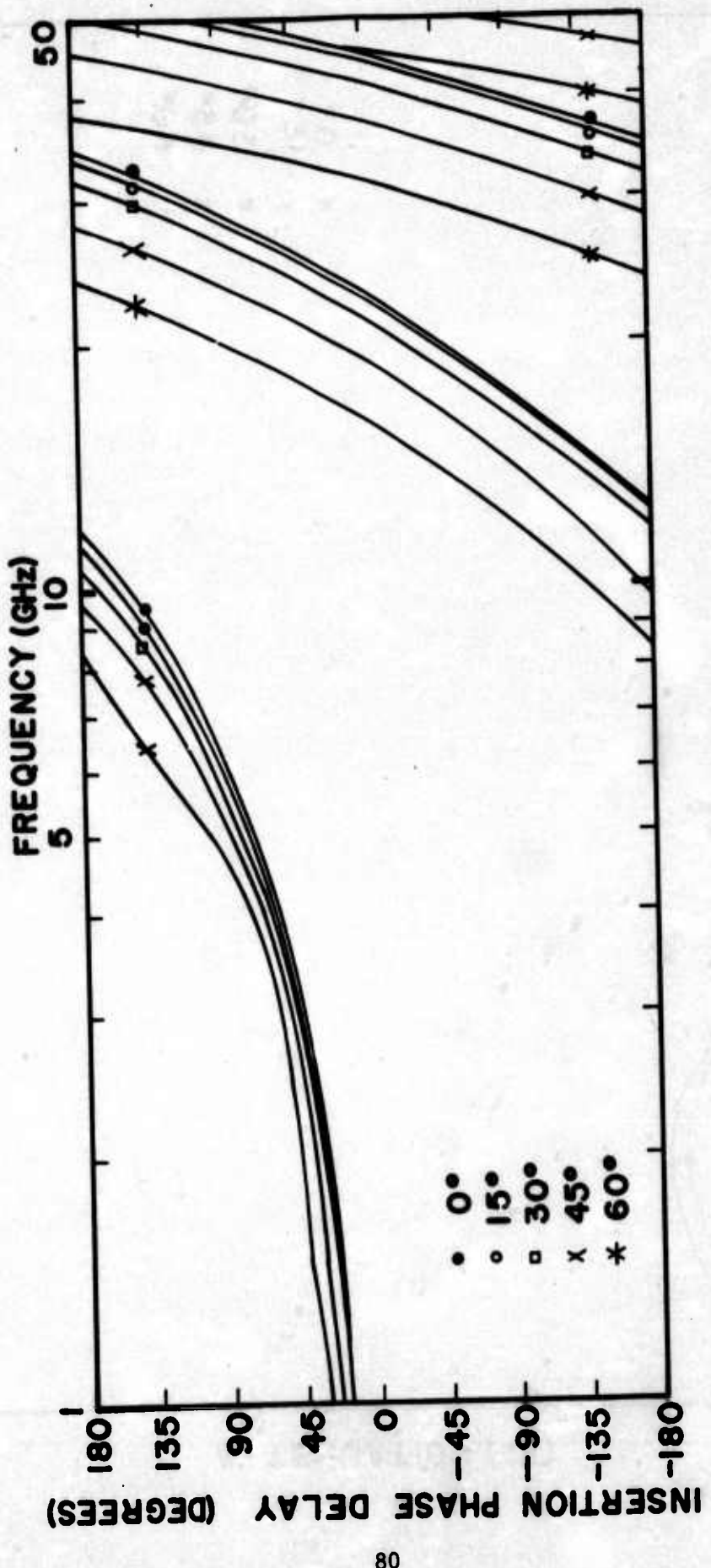


Figure 36. Insertion Phase Delay of Perpendicular Polarized Component for Panel No. 2.

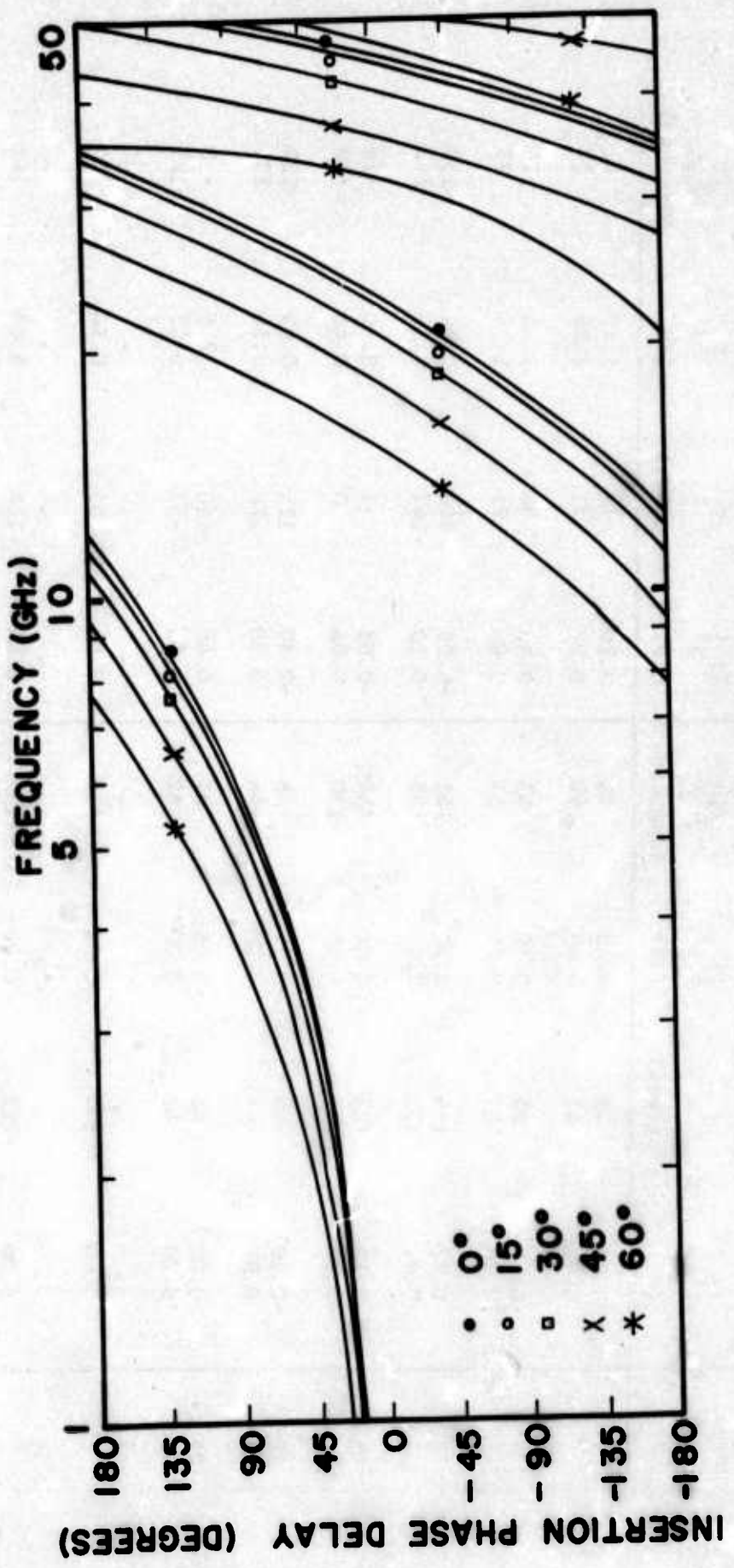


Figure 37. Insertion Phase Delay of Parallel Polarized Component for Panel No. 2.

TABLE II
COMPARISON OF MEASURED AND PREDICTED TRANSMISSION LOSS AND INSERTION
PHASE DELAY FOR PANEL NUMBER 1

Freq. (GHz)	0° Incidence				60° Incidence			
	$ T_{\parallel} $ (dB)	$\angle T_{\parallel}$ (degrees)	$ T_{\perp} $ (dB)	$\angle T_{\perp}$ (degrees)	$ T_{\parallel} $ (dB)	$\angle T_{\parallel}$ (degrees)	$ T_{\perp} $ (dB)	$\angle T_{\perp}$ (degrees)
3	0.50*	41	0.40	44	0.20	70	3.10	62
	0.44	42	0.44	42	0.02	71	2.89	59
4	-0.15	55	0.10	55	-0.40	94	1.60	75
	0.06	57	0.06	57	0.07	95	1.54	75
9	-0.22	135	-0.22	142	-0.25	-145	-0.14	-157
	0.02	135	0.02	135	0.10	-147	0.10	-163
15	-0.15	-128	0.00	-134	-0.03	-7	0.30	-18
	0.00	-130	0.00	-130	0.06	0	0.46	-19
20	-0.10	-45	-0.15	-45	-0.30	125	-0.05	120
	0.00	-46	0.00	-46	0.00	128	0.14	104
25	0.00	46	-0.05	41	0.40	-110	-12.9	-50
	0.00	42	0.00	42	0.09	-97	0.03	-125
30	-	-	-	-	-	-	-	-
	0.00	137	0.00	137	0.04	45	0.14	14
35	-	-	-	-	-	-	-	-
	0.00	-122	0.00	-122	0.04	-164	0.03	161

*Upper figures are measured values, lower figures are predicted values.

TABLE III
COMPARISON OF MEASURED AND PREDICTED TRANSMISSION LOSS AND INSERTION
PHASE DELAY FOR PANEL NUMBER 2

Freq. (GHz)	0° Incidence				60° Incidence			
	$ T_{\parallel} $ (dB)	$\angle T_{\parallel}$ (degrees)	$ T_{\perp} $ (dB)	$\angle T_{\perp}$ (degrees)	$ T_{\parallel} $ (dB)	$\angle T_{\parallel}$ (degrees)	$ T_{\perp} $ (dB)	$\angle T_{\perp}$ (degrees)
3	0.50*	45	0.35	43	0.00	74	2.85	63
	0.44	42	0.44	42	0.02	71	2.89	59
4	-0.20	58	0.08	59	-0.25	102	1.30	79
	0.06	57	0.06	57	0.07	95	1.55	74
9	-0.10	137	-0.20	137	0.10	-136	0.00	-152
	0.01	134	0.01	134	0.09	-148	0.11	-165
15	0.05	-128	0.05	-125	0.05	-11	0.25	-13
	0.00	-134	0.00	-134	0.06	-6	0.43	-25
20	0.05	-48	-0.10	-49	0.20	130	0.00	110
	0.00	-57	0.00	-57	0.01	114	0.16	89
25	0.10	32	0.10	31	0.60	-93	0.60	-125
	0.00	21	0.00	21	0.04	-124	0.01	-153
30	-	-	0.10	116	-	-	0.35	-7
	0.00	101	0.00	101	0.07	0	0.05	-34
35	-	-	0.10	-140	-	-	0.10	171
	0.00	-177	0.00	-177	0.00	127	0.10	88

* Upper figures are measured values, lower figures are predicted values.

SECTION VI

PROBLEM AREAS

The broadband panel is unique in its bandwidth capability, but problems have been encountered in its fabricability, in its low frequency operating characteristics, and in the shape of the external surface. During this program, Rexolite[®] ($\epsilon_r = 2.54$) was used as the base material. All of the panels were machined from Rexolite[®]. This material is not a typical flight material for radomes and antenna windows, although it could be used on a ground-based application. The machining process is laborious and is not cost effective. For applications where a plastic material can be used, the panel could be built-up from small elements that are either glued or pressed together. Each individual panel element would be fabricated by either a casting or molding technique.

Another process for panel fabrication is that of injection molding. This would be especially applicable to a ceramic panel such as slip-cast fused silica. A pattern mold is made by injection molding. This mold in turn would be used to form an additional mold out of a material such as paraffin from which the broadband panel would be formed.

The undesirable feature of this particular broadband panel design is the thickness requirement for operation near 2 GHz. The 1.5-inch thickness panel operates well above 4 GHz and does so only if the base material has a low dielectric constant (less than 4.0). Even with this thickness, the density of the material is approximately 0.63 g/cc (Panel No. 2). The pyramidal plate design has a density of 0.48 g/cc. Since Rexolite[®] has

a density of 1.05 g/cc, the weight of this type panel is reduced by one-half when machined. For operation near 2 GHz, the panel would approach a thickness of 3 inches based on the current design.

The non-smooth exterior surface might present a problem in some flight environments. It is not likely to pose much of a problem for aircraft use since it has been shown in this report that a thin covering can be used without degradation of the panel transmission properties.

SECTION VII

CONCLUSIONS AND RECOMMENDATIONS

General conclusions drawn from the research work performed are:

- (1) Bandwidths of 10:1 are readily attainable on the broadband flat panels, where bandwidth is defined as the frequency range of 90 percent or greater power transmission coefficient.
- (2) The difference in insertion phase delay for perpendicular and parallel polarizations is minimal for angles of incidence up to 60°. This implies that the broadband panel will operate satisfactorily for circularly polarized radiation.
- (3) The broadband panel operates satisfactorily in a curved configuration.
- (4) The panel requires a thickness of approximately 1.5-inches to operate near 4.0 GHz using a material of relative dielectric constant near 2.5.
- (5) For operation below 4.0 GHz, the panel thickness requirement becomes severe for most applications. In addition, a weight penalty would necessarily be imposed.
- (6) Rain erosion coatings can be applied to the structure without serious degradation of performance.
- (7) There are fabrication techniques that are readily adaptable to the broadband panel.
- (8) A computer program has been developed which allows anisotropic panels to be fully analyzed.

Due to the potential use of this type structure, specific recommendations are as follows:

- (1) A radome which operates from 8 GHz to 40 GHz should be fabricated from a typical organic material such as polyimide-quartz or PRD-49 and tested as a broadband structure and as a boresight radome.
- (2) A radome which operates from 8 GHz to 40 GHz should be fabricated from a ceramic material such as slip-cast fused silica. This radome should then be electrically tested.

- (3) Design techniques should be explored that would enhance the lower frequency characteristics of the panel without degrading the overall performance.
- (4) There are current requirements for dual mode radomes (RF/IR) which have a broadband RF requirement. The potential of this type structure for this application should be fully explored.
- (5) Broadband antenna windows should be designed, fabricated, and tested for use on current aircraft development programs.

APPENDIX A

EVALUATION OF PROPAGATION CONSTANTS AND DIRECTIONS OF PROPAGATION

A system of equations will be derived for determining the propagation constants and the directions of propagation in each layer of the anisotropic radome panel discussion in the main portion of the presentation. Each layer is assumed to be linear, homogeneous, lossless, charge free, and possibly dielectrically anisotropic. The evaluation will take place at an arbitrary interface, $z = z_m$ = a constant as shown in Figure 38.

A. Derivation of Basic Equations

The fields in each region will be the sum of a number of plane waves traveling in different directions with different propagation constants. In the m -th region the electric field will have the form

$$\bar{E}_m = \sum_j \bar{E}_{mj} e^{-j\beta_{mj} \bar{n}_{mj} \cdot \bar{r}} \quad (64)$$

where the summation index j includes all ordinary and extraordinary waves no matter what their direction of travel. The vectors \bar{E}_{mj} are complex constant vectors representing the wave amplitudes, β_{mj} is the propagation constant, and \bar{n}_{mj} is a unit vector in the direction of propagation.

At the interface $z = z_m$ the phase variations in both the x and y directions must be the same for each term on both sides of the interface. Thus

$$\beta_{mj} n_{x_{mj}} = \beta_{mk} n_{x_{mk}} \quad (65)$$

$$\beta_{mj} n_{y_{mj}} = \beta_{mk} n_{y_{mk}} \quad (66)$$

$$\beta_{mj} n_{x_{mj}} = \beta_{(m+1)k} n_{x_{(m+1)k}} \quad (67)$$

$$\beta_{mj} n_{y_{mj}} = \beta_{(m+1)k} n_{y_{(m+1)k}} \quad (68)$$

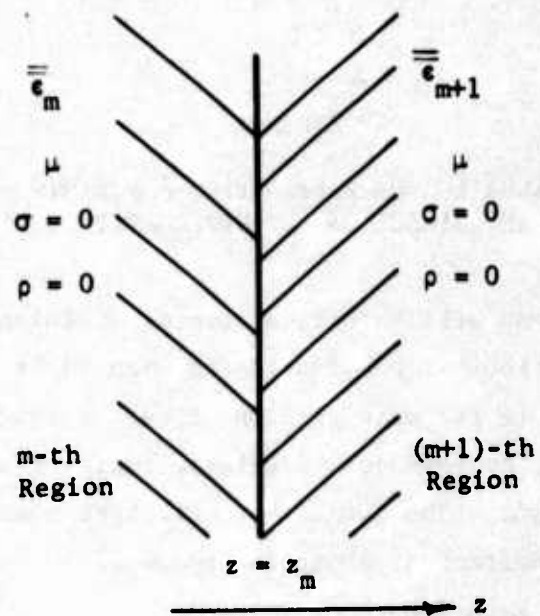


Figure 38. Medium Parameter at the Interface at $z = z_m$.

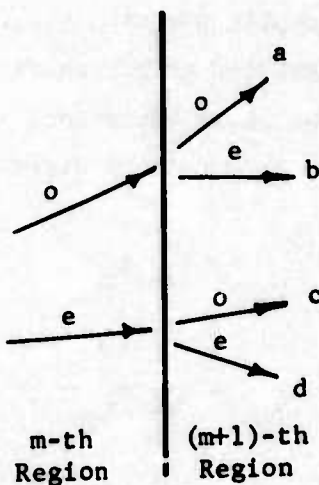


Figure 39. The Splitting of Two Waves Into Four When Passing Into a New Medium.

where j and k represent any pair of waves in the two media and the x, y, z subscripts on n represent the particular rectangular components of that vector \bar{n} . According to Collin [6, p. 98], if the permittivity tensor is diagonal in rectangular coordinates with components in the $(m+1)$ st region of

$$\bar{\epsilon}_{m+1} = \epsilon_0 \begin{bmatrix} \kappa_{x_{m+1}} & 0 & 0 \\ 0 & \kappa_{y_{m+1}} & 0 \\ 0 & 0 & \kappa_{z_{m+1}} \end{bmatrix}$$

then the β 's and n 's in the $(m+1)$ st region satisfy the equation

$$\begin{aligned} & (\beta_{m+1}^2 - \kappa_{y_{m+1}} k_0^2) (\beta_{m+1}^2 - \kappa_{z_{m+1}} k_0^2) n_{x_{m+1}}^2 \kappa_{x_{m+1}} k_0^2 \\ & + (\beta_{m+1}^2 - \kappa_{z_{m+1}} k_0^2) (\beta_{m+1}^2 - \kappa_{x_{m+1}} k_0^2) n_{y_{m+1}}^2 \kappa_{y_{m+1}} k_0^2 \\ & + (\beta_{m+1}^2 - \kappa_{x_{m+1}} k_0^2) (\beta_{m+1}^2 - \kappa_{y_{m+1}} k_0^2) n_{z_{m+1}}^2 \kappa_{z_{m+1}} k_0^2 \\ & = 0 \end{aligned} \quad (69)$$

where the k subscripts denoting a particular component in the $(m+1)$ st region have been dropped for simplicity and k_0 is the free space propagation constant.

Since \bar{n}_{m+1} is a unit vector, it follows that

$$n_{z_{m+1}}^2 = 1 - n_{x_{m+1}}^2 - n_{y_{m+1}}^2 \quad (70)$$

substituting (67), (68) and (70) into (69) and dropping the j subscripts for convenience yields

$$\begin{aligned} & (\beta_{m+1}^2 - \kappa_{y_{m+1}} k_0^2) (\beta_{m+1}^2 - \kappa_{z_{m+1}} k_0^2) n_{x_m}^2 \kappa_{x_{m+1}} \\ & + (\beta_{m+1}^2 - \kappa_{z_{m+1}} k_0^2) (\beta_{m+1}^2 - \kappa_{x_{m+1}} k_0^2) n_{y_m}^2 \kappa_{y_{m+1}} \end{aligned}$$

$$\begin{aligned}
 & + (\beta_{m+1}^2 - \kappa_{x_{m+1}} \kappa_o^2) (\beta_{m+1}^2 - \kappa_{y_{m+1}} \kappa_o^2) \\
 & \cdot \left(\frac{\beta_{m+1}^2}{\beta_m^2} - n_{x_m}^2 - n_{y_m}^2 \right) \kappa_{z_{m+1}} = 0
 \end{aligned} \tag{71}$$

Equation 71 shows that if all of the medium parameters are known and if β and \bar{n} are known for the incident wave in the 1-st medium (which is the usual case) then the β 's and n 's for all regions to the right of the first one can be determined. This last statement is true since all terms in (71) are known in the m -th region. Also, Equations 67, 68 and 70 allow \bar{n}_{m+1} to be determined from \bar{n}_m , β_m , and β_{m+1} (all of which are known) as

$$\begin{aligned}
 n_{x_{m+1}} &= \frac{\beta_m}{\beta_{m+1}} n_{x_m} \\
 n_{y_{m+1}} &= \frac{\beta_m}{\beta_{m+1}} n_{y_m} \\
 n_{z_{m+1}} &= + \sqrt{1 - n_{x_{m+1}}^2 - n_{y_{m+1}}^2}
 \end{aligned} \tag{72}$$

B. Properties of Propagation Constant Equation

Some of the properties of (71) will now be examined. First notice that (71) is a cubic equation in β_{m+1}^2 and that $\beta_{m+1}^2 = 0$ is always a solution. To prove this last statement simply substitute $\beta_{m+1}^2 = 0$ into (71) and obtain

$$\begin{aligned}
 & \kappa_{x_{m+1}} \kappa_{y_{m+1}} \kappa_{z_{m+1}} n_{x_m}^2 + \kappa_{x_{m+1}} \kappa_{y_{m+1}} \kappa_{z_{m+1}} n_{y_m}^2 \\
 & + \kappa_{x_{m+1}} \kappa_{y_{m+1}} \kappa_{z_{m+1}} (-n_{x_m}^2 - n_{y_m}^2) = 0
 \end{aligned}$$

Thus there are only two nontrivial solutions for β_{m+1}^2 in (71). Thus, in general, for each wave incident from medium m onto the interface, two waves are produced in region $m+1$ each having different values of β_{m+1} and \bar{n}_{m+1} .

The second property that will be proved is that if all dielectric constants are positive then

$$\begin{aligned}
 k_o^2 \min(\kappa_{x_{m+1}}, \kappa_{y_{m+1}}, \kappa_{z_{m+1}}) &\leq \beta_{m+1}^2 \\
 \leq k_o^2 \max(\kappa_{x_{m+1}}, \kappa_{y_{m+1}}, \kappa_{z_{m+1}}) & \tag{73}
 \end{aligned}$$

The validity of (73) can be seen from Equation (69). If

$$\beta_{m+1}^2 > k_o^2 \max(\kappa_{x_{m+1}}, \kappa_{y_{m+1}}, \kappa_{z_{m+1}})$$

then the left hand side of (69) is positive and a solution of (69) does not exist. Similarly if

$$\beta_{m+1}^2 < k_o^2 \min(\kappa_{x_{m+1}}, \kappa_{y_{m+1}}, \kappa_{z_{m+1}})$$

then the left hand side of (69) is again positive and no solution exists. Thus, (73) is proven.

Let us next prove that there is only one incident ordinary and one incident extraordinary wave in each region. First assume that there is only one incident ordinary and extraordinary wave in region m ; then, the most general situation in region $(m+1)$ is one in which four waves are present. One ordinary and one extraordinary wave could be produced for each of the two incident waves. These four waves in region $(m+1)$ will be labeled a through d as shown in Figure 39. We must show that a and c are the same and that b and d are the same. From (65) and (67) it follows that

$$n_{x_{m+1}}^{oa} = \frac{\beta_m^o n_x^o}{\beta_{m+1}^{oa}} \tag{74}$$

$$n_{x_{m+1}}^{eb} = \frac{\beta_m^o n_x^o}{\beta_{m+1}^{eb}} \tag{75}$$

$$n_{x_{m+1}}^{oc} = \frac{\beta_m^e n_x^e_m}{\beta_{m+1}^{oc}} \quad (76)$$

$$n_{x_{m+1}}^{ed} = \frac{\beta_m^e n_x^e_m}{\beta_{m+1}^{ed}} \quad (77)$$

$$\beta_m^o n_x^o_m = \beta_m^e n_x^e_m \quad (78)$$

$$\beta_{m+1}^{eb} n_{x_{m+1}}^{eb} = \beta_{m+1}^{ed} n_{x_{m+1}}^{ed} \quad (79)$$

A set of equations similar to the last six can be written for the y components of the direction of propagation vectors.

It is obvious that

$$\beta_{m+1}^{oa} = \beta_{m+1}^{oc} \quad (80)$$

since the ordinary propagation constant of a medium is independent of the direction of the wave [5, p. 680]. Utilizing (78) and (80) it can be seen that the right hand sides of (74) and (76) are identical. Hence,

$$n_{x_{m+1}}^{oa} = n_{x_{m+1}}^{oc} \quad (81)$$

In a similar manner it can be shown that

$$n_{y_{m+1}}^{oa} = n_{y_{m+1}}^{oc} \quad (82)$$

Hence from (72)

$$n_{z_{m+1}}^{oa} = n_{z_{m+1}}^{oc} \quad (83)$$

From (80) through (83) it follows that waves a and c are identical since they travel in the same direction with the same velocity.

Next it must be shown that waves b and d are identical. To do this notice that both of these waves satisfy (71) but with different β_m , n_{x_m} and n_{y_m} values. If (71) is multiplied by β_m^2 and then (78) and a corresponding equation for the n_y components are used, it can be seen that the propagation constants of the b and d waves satisfy the same equation and so are the same. Using (78) and the fact that

$$\beta_{m+1}^{eb} = \beta_{m+1}^{ed}$$

in (75) and (77) reveals that

$$n_{x_{m+1}}^{eb} = n_{x_{m+1}}^{ed}$$

In a similar fashion it can be shown that

$$n_{y_{m+1}}^{eb} = n_{y_{m+1}}^{ed}$$

Hence from (72)

$$n_{z_{m+1}}^{eb} = n_{z_{m+1}}^{ed}$$

Thus, since waves b and d travel in the same direction with the same velocity, they must represent the same wave.

It has thus been proved that two waves incident from region m onto region $(m+1)$ can produce at most two incident waves in region $(m+1)$. Only one wave would be produced if region $(m+1)$ were isotropic. This situation holds true for any region m and hence holds true for the entire panel. It is of course well known that one wave incident from an isotropic region, ie: region 1, onto an anisotropic region, ie: region 2, will produce in general two incident waves in region 2.

The proof that no more than two incident waves exist in each region hinged on the permittivity tensor being diagonal. An example of such a permittivity tensor is one describing a uniaxial medium in which the optic axis lies either along the x or y coordinate axes.

Now consider the case of a panel each layer of which is uniaxial and for which each optic axis lies along either the x or the y axis. In the former case $\kappa_y = \kappa_z$ while in the latter $\kappa_x = \kappa_z$. For either of these two cases it can be seen from (A-8) that

$$\beta_{m+1}^2 = \kappa_{z_{m+1}} \kappa_0^2 \quad (84)$$

is one of the two nontrivial solutions of (71). Since (84) is independent of the direction of propagation it represents the ordinary wave propagation constant [5, p. 680]. The remaining solution of (71) must represent the extraordinary wave. Next notice that (84) is independent of direction or propagation in the other layers. Hence, the ordinary β may be determined from (84) and only the extraordinary β need be found from (71). The nonlinear equation (71) may be solved using Newton-Raphson, Muller or other methods. The region over which to search for the solution can be determined by examining (73) and (84).

APPENDIX B

TYPICAL RADIATION PATTERNS OF CYLINDRICAL PANEL

The six figures included in Appendix B are representative radiation patterns using the cylindrical panel as an antenna window. The figures denote the amplitude/phase characteristics of: (1) the test horn antenna, (2) the test horn antenna placed behind the cylindrical grooved panel, and (3) the test horn behind the fiberglass covered cylindrical grooved panel. Both horizontal and vertical polarization plots are shown and these were measured at a frequency of 11.0 GHz. As noted, the cylindrical panel was positioned horizontally and the angle of incidence was measured from a vertical plane through the center of the panel. Very little difference in amplitude is noted for the patterns.

The radiation patterns of the horn antenna with the cylindrical panel positioned vertically and with the incidence angle again measured from a vertical plane through the center of the panel showed a focusing effect at all frequencies. This was due to the small radius of the panel. These patterns are not included here but the focusing effect occurred at all frequencies.

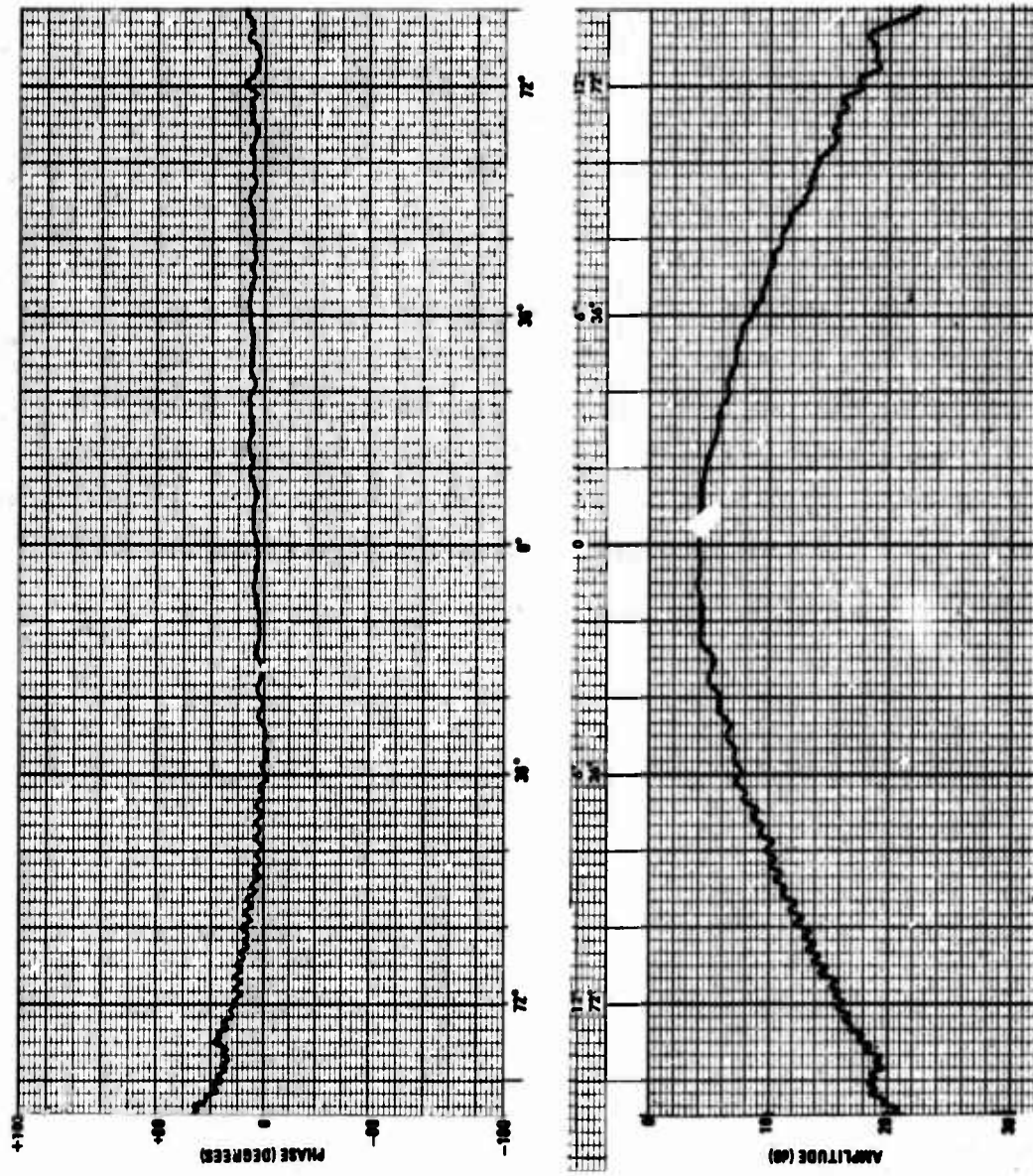


Figure 40. Phase/Amplitude Plots, Horn Antenna. Vertical Polarization, 11 GHz.

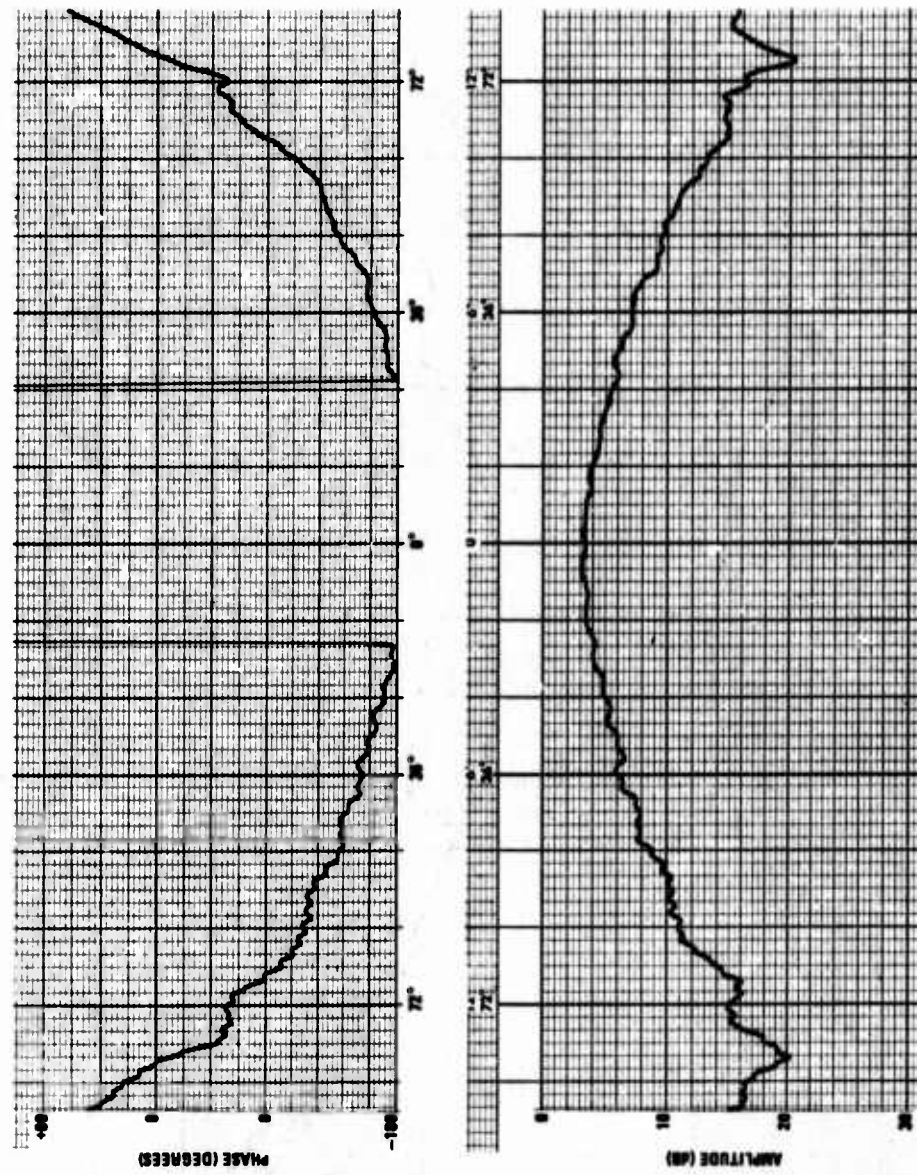


Figure 41. Phase/Ampplitude Plots, Horn Antenna and Cylindrical Panel,
Vertical Polarization, 11 GHz, Panel Horizontal.

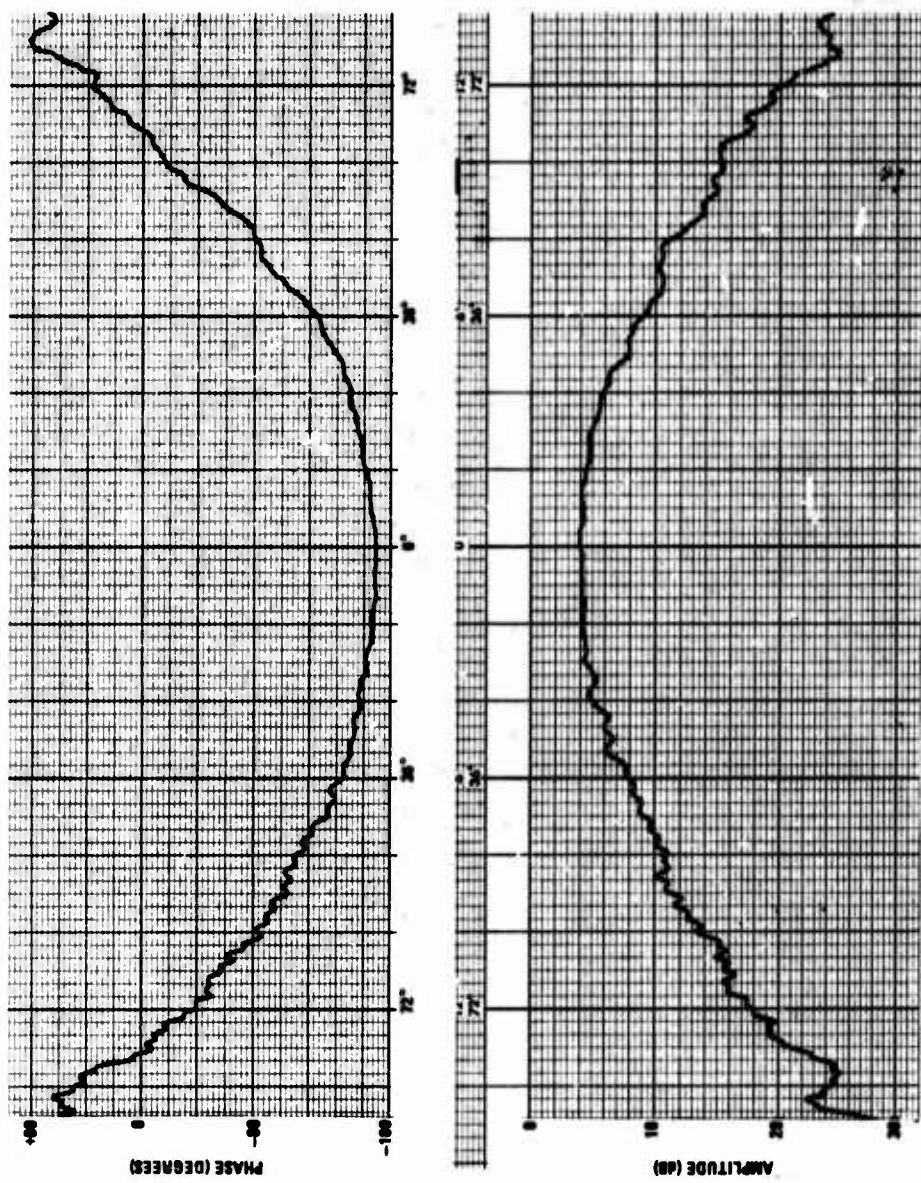


Figure 42. Phase/Amplitude Plots, Horn Antenna and Cylindrical Panel, Vertical Polarization, 11 GHz, Panel Horizontal; Fiberglass Cover.

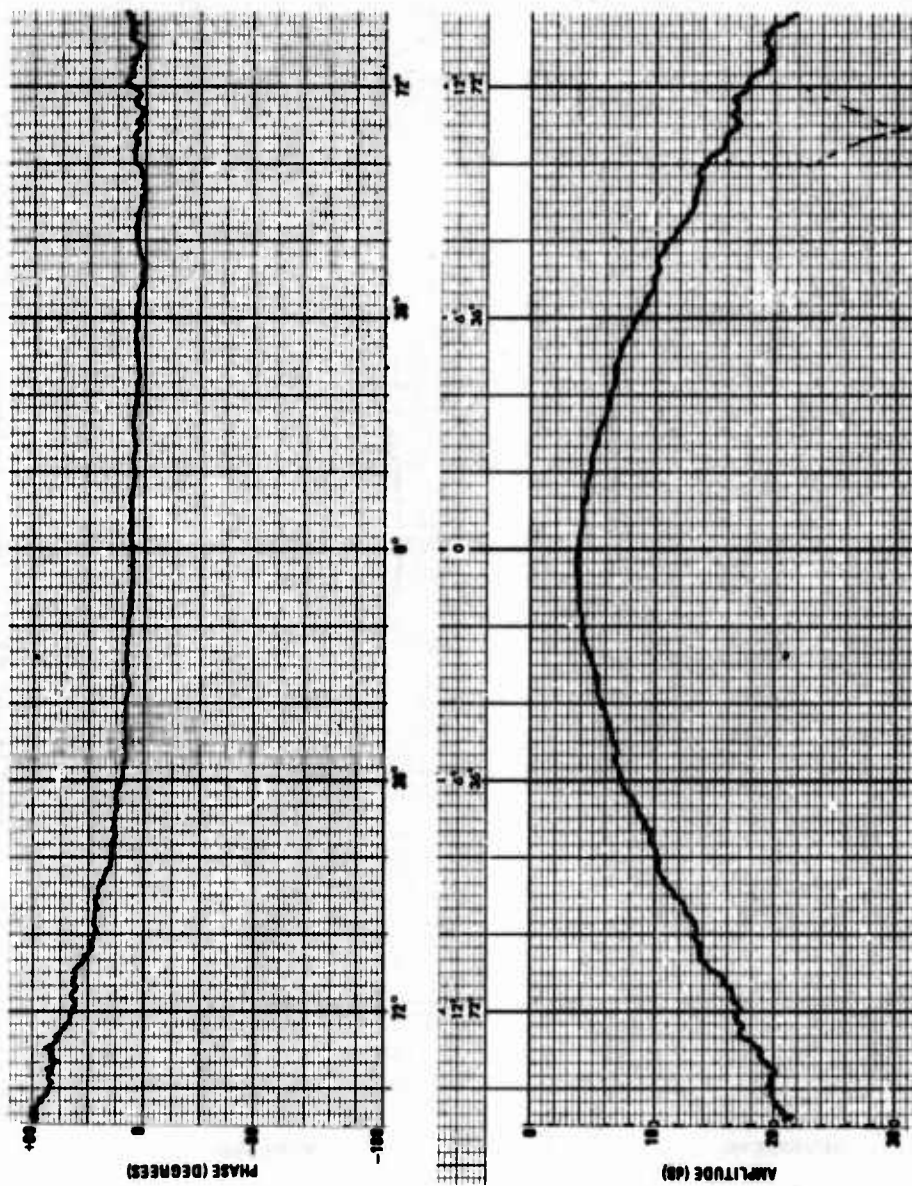


Figure 43. Phase/Amplitude Plots, Horn Antenna, Horizontal Polarization, 11 GHz.

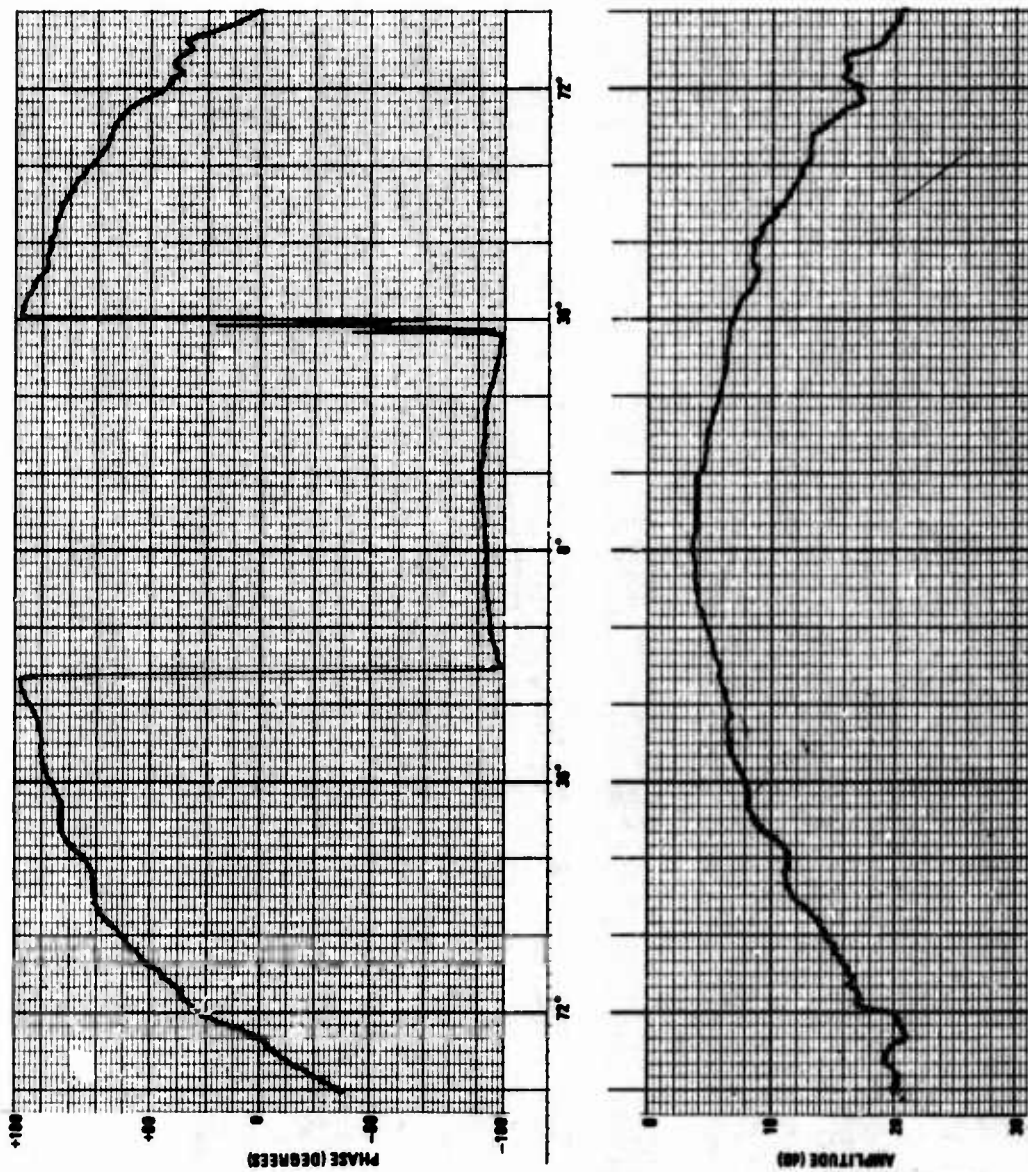


Figure 44. Phase/Ampitude Plots, Horn Antenna and Cylindrical Panel, Horizontal Polarization, 11 GHz; Panel Horizontal.

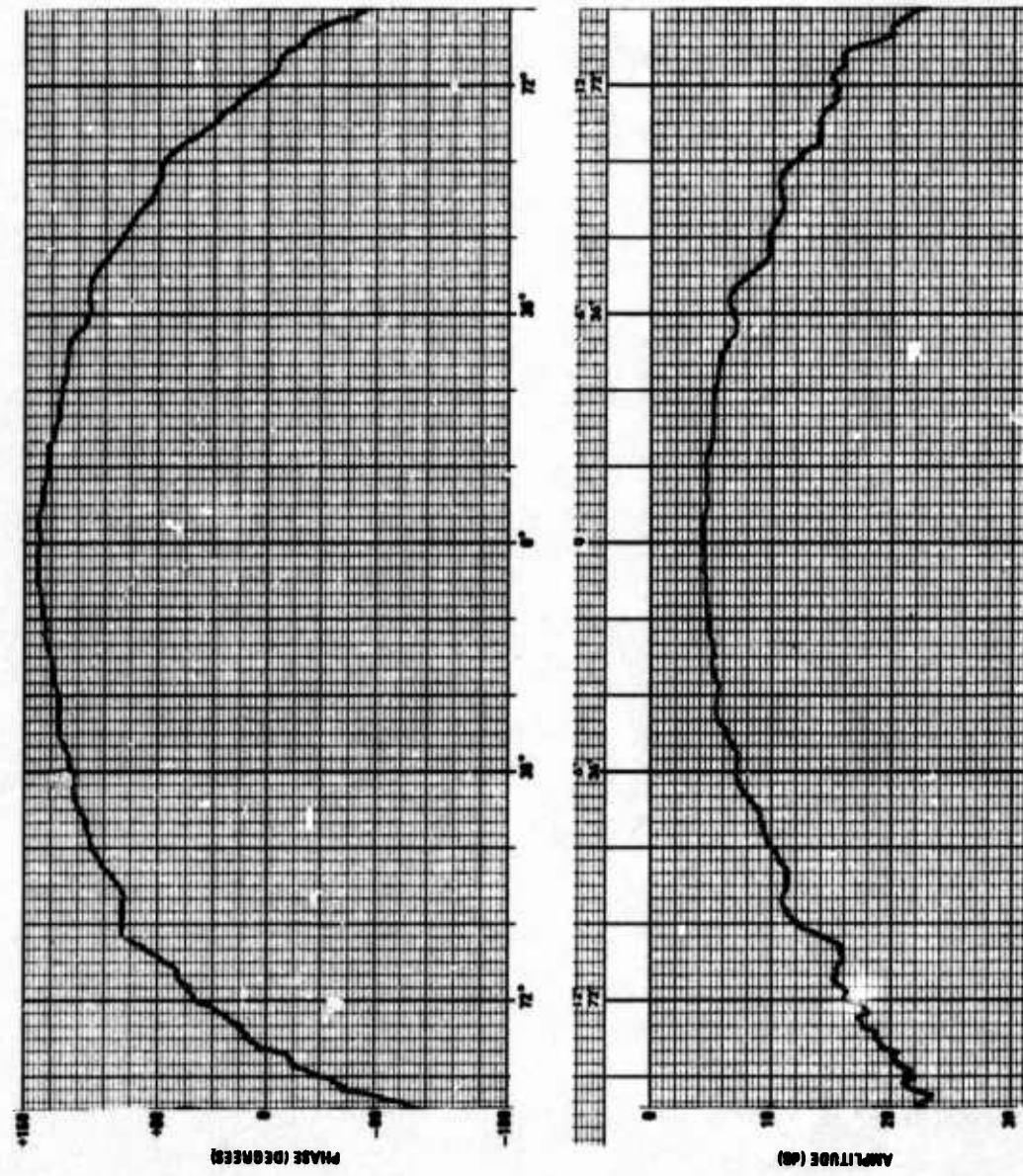


Figure 45. Phase/Amplitude Plots, Horn Antenna and Cylindrical Panel, Horizontal Polarization, 11 GHz; Panel Horizontal; Fiberglass Cover.

REFERENCES

1. H. L. Bassett and G. K. Huddleston, "Broadband Radome Techniques," Interim Report No. 1, Georgia Tech Project A-1333, AF Contract F33615-71-C-1694, February 1973.
2. K. H. Breeden, et al., "Millimeter Radome Design Techniques," Technical Report AFAL-TR-70-163, Georgia Tech Project A-1071, AF Contract F33615-68-C-1193, August 1970.
3. H. L. Bassett, et al., "Inorganic Nose Cone Techniques for Sidelobe Reduction," Technical Report AFAL-TR-71-172, Georgia Tech Project A-1220, AF Contract F33615-70-C-1237, July 1971.
4. J. H. Richmond, "The WKB Solution for Transmission Through Inhomogeneous Plane Layers," IRE Transactions on Antennas and Propagation, Vol. AP-10, pp. 472-473, July 1962.
5. M. Born and E. Wolf, Principles of Optics, New York: Pergamon Press, 1964, pp. 665-681.
6. R. E. Collin, Field Theory of Guided Waves, New York: McGraw-Hill, 1960, pp. 97-102.
7. J. Strong, Concepts of Classical Optics, San Francisco: W. H. Freeman, 1958, pp. 128-133.
8. D. S. Jones, The Theory of Electromagnetism, New York: Pergamon Press, 1964, pp. 329-332.

DISTRIBUTION LIST

1 AFAL/WRP (Mr. W. P. Eviston)
WPAFB OH 45433

1 AFAL/NVS
WPAFB OH 45433

1 AFAL/NVT
Wright-Patterson AFB, OH 45433

1 AFAL/TSR
WPAFB, OH 45433

1 ASD/ENVCD Lester Wagner
WPAFB OH 45433

1 AFML/MANC (Mr. H. S. Schwartz)
WPAFB OH 45433

1 SEG/SEACA (Mr. G. Duree)
WPAFB OH 45433

1 SEG(SEPI)
WPAFB OH 45433

1 2750 AB Wg/SSI
area B Technical Library
WPAFB OH 45433

1 ASD/ASNPD-30
Wright-Patterson AFB OH 45433

1 AFML/LPE (Dr. WGD Frederick)
WPAFB Ohio 45433

1 AFML/LNE (George Schmitt)
WPAFB OH 45433

1 AFAL/TEM-3 P. Springer
WPAFB OH 45433

1 2750 AB Wg/SSL
WPAFB, OH 45433

1 Repro + 10

Government

1

Hq USAF/SAMID
Wash DC

1

AFOSR/SRE
1400 Wilson Blvd
Arlington, VA 22209

1

APGC/PGVEP-3
Eglin AFB F1 32542

1

RADC/EMEA (Mr. Curtis)
Griffiss AFB, NY 13442

1

USAF (AFCSAMI)
Andrews AFB
Wash DC 20331

1

AFCRL(CRD)
ATTN: Mr. Phil Blacksmith
Lawrence G. Hanscom Fld
Bedford, MA 01730

1

AFMDC (Technical Library)
Holloman AFB, NM 88330

1

AFMTC(Technical Library)
Patrick AFB, FL 32925

1

AFWL (WLRJ-Mr. Moulds)
Kirtland AFB, NM 87177

1

Hq USAF (AFXSAI)
Air Battle Analysis Center
Deputy Director of Plans
for War Plans
Wash DC 20332

1

RTD(RTTC)
Bolling AFB DC 20332

1

Air University Library
Maxwell AFB AL 36112

Government

1 Chief, Technical Library
Office of Asst Secretary of Def R&D
Room 3E 1065, The Pentagon
Washington, DC 20330

1 U.S. Army Missile Command
ATTN: Mr. P. A. Ormsby, AMSMI-RSM
Redstone Arsenal, Alabama 35809

1 Commanding General
U. S. Army Missile Command
ATTN: AMCPM-MDEM (Glen B. Micholas)
Redstone Arsenal, Alabama 35809

1 Commander
US Army White Sands
ATTN: SIGWS-FC-02
White Sands, NM 88002

1 Mr. Melvin C. Gilreath
Mail Stop 490
NASA-Langley Research Center
Hampton, VA 23365

1 Director
Ballistics Research Laboratory
ATTN: Ballistics Measurement Lab
Aberdeen Proving Ground MD 21005

1 Army Materials & Mechanics
Research Center (D. R. Messier)
Arsenal Street
Watertown, MA 02172

1 Allen Shipley
Calstec
Picatinny Arsenal
Dover, N. J. 07801

1 Central Intelligence Agency
Code SAN
2430 E NW
Wash DC 20505

1 Scientific & Tech Info Fac
ATTN: NASA Rep (SAK/DL)
P. O. Box 5700
Bethesda, MD 20014

Government

1

Naval Air Systems Command
(AIR-52032-A (Charles F. Bersch))
Wash DC 20360

1

Harry Diamond Labs (Howard Jones)
Dept of the Army
Connecticut Ave & Van Ness St.
Washington, DC 20438

1

U. S. Army Missile Command
AMSMI-RLP (Kenneth N. Letson)
Redstone Arsenal, Alabama 35809

1

Air University Library
Maxwell AFB Ala 36112

2

AFAL/TSR
WPAFB OH

12

DDC
Cameron Station
Alexandria Virginia 22314

Companies

1

Aerospace Corporation
Technical Library
P. O. Box 92957
Los Angeles, CA 90009

1

The Boeing Company
ATTN: T. Larry Norin
P. O. Box 3999
Seattle WA 98148

1

Boeing Aerospace Co.
ATTN: Robert W. Sutton
P. O. Box 3999
Seattle WA 98148

Companies

1 General Dynamics/Electronics
P. O. Box 81127
ATTN: Mr. Gus Tricoles
3302 Pacific Coast Highway
San Diego, CA 92112

1 Texas Instruments, Inc.
ATTN: Don Purington Antenna & Microwave
Division
P. O. Box 6015
Dallas Tx 75222

Companies

1 Brunswick Corp
 ATTN: John B. Styron
 Marion, VA 24354

1 RCA/Government & Commercial Systems
 ATTN: E. Tahan
 Aerospace Systems Division
 P. O. Box 588 Burlington MA 01803

1 The Magnavox Co
 ATTN: E. Swartz
 Government & Industrial Group
 Fort Wayne, Indiana

1 North American Rockwell Corp
 ATTN: R. Craig Sparling
 Los Angeles International Airport
 Los Angeles, CA 90009

1 McDonnell Douglas Corp
 ATTN: George J. Cossell
 Douglas Aircraft Co.
 3855 Lakewood Boulevard
 Long Beach CA 90801

1 Hughes Aircraft Co.
 Aerospace Group (Robert W. Jones)
 Culver City, CA

1 Motorola Inc.
 Government Electronics Division
 ATTN: Donald Lee Loyet
 8201 E McDowell Road
 Scottsdale, Ariz 85252

Universities

1 University of Michigan
 ATTN: Mr. Ralph Hiatt
 201 Catherine Street
 Ann Arbor, MI 48104

4 Georgia Institute of Technology
 Engineering Experiment Station
 Atlanta, GA 30332

1 Ohio State University
 ATTN: Dr. R. C. Rudduck
 1320 Kinnear Road
 Columbus, OH 43212

Unclassified

SECURITY CLASSIFICATION OF THIS PAGE (When Data Entered)

REPORT DOCUMENTATION PAGE		READ INSTRUCTIONS BEFORE COMPLETING FORM
1. REPORT NUMBER AFAL-TR-74-128	2. GOVT ACCESSION NO.	3. RECIPIENT'S CATALOG NUMBER
4. TITLE (and Subtitle) BROADBAND RADOME TECHNIQUES		5. TYPE OF REPORT & PERIOD COVERED Final Technical Report May 1971 - May 1974
		6. PERFORMING ORG. REPORT NUMBER
7. AUTHOR(s) H. L. Bassett, D. G. Bodnar, G. K. Huddleston, and J. M. Newton		8. CONTRACT OR GRANT NUMBER(s) F33615-71-C-1694
9. PERFORMING ORGANIZATION NAME AND ADDRESS AFAL/TEM 3 Wright-Patterson Air Force Base, Ohio 45433		10. PROGRAM ELEMENT, PROJECT, TASK AREA & WORK UNIT NUMBERS 20020408
11. CONTROLLING OFFICE NAME AND ADDRESS		12. REPORT DATE May 1974
		13. NUMBER OF PAGES
14. MONITORING AGENCY NAME & ADDRESS (if different from Controlling Office)		15. SECURITY CLASS. (of this report) Unclassified
		15a. DECLASSIFICATION/DOWNGRADING SCHEDULE
16. DISTRIBUTION STATEMENT (of this Report) Distribution limited to U. S. Government agencies only, test and evaluation results reported. Other requests for this document must be referred to AFAL/TEM, Wright-Patterson Air Force Base, Ohio 45433		
17. DISTRIBUTION STATEMENT (of the abstract entered in Block 20, if different from Report)		
18. SUPPLEMENTARY NOTES		
19. KEY WORDS (Continue on reverse side if necessary and identify by block number) Broadband Radomes Electromagnetic Windows Anisotropic Dielectric Pane		
20. ABSTRACT (Continue on reverse side if necessary and identify by block number) The significance of this research and development to the Air Force is that a new type of electromagnetic window panel was designed and tested that exhibited a bandwidth of 10:1 or greater. Empirical data are included on both flat panels and curved panels. A typical panel that operates from 4 GHz to 40 GHz, having 90 percent or better transmission coefficient from 0° to 60° angle of incidence range, is 1.5-inches in thickness. The inner and outer surfaces of the panel are either grooves or pyramids. This type panel design		

20 has excellent circular polarization characteristics, since the amplitudes of the parallel and perpendicular components are near equal and since the insertion phase delays for the two components are approximately the same. Antenna radiation pattern measurements are included that also verify the broadband characteristics of these panels. Data are also presented on a computer analysis program of transmission through an anisotropic media. The analytical results compare favorably with the measured data.